

ABSTRACT

Title of Dissertation: EXPERIMENTAL AND COMPUTATIONAL
ANALYSIS OF AN ELECTROHYDRODYNAMIC
MESOPUMP FOR SPOT COOLING APPLICATIONS

Amir Shoushtari, Doctor of Philosophy, 2004

Dissertation directed by: Professor Michael Ohadi
Department of Mechanical Engineering

As electronic products become faster, more compact, and incorporate greater functionality, their thermal management becomes increasingly more challenging as well. In fact, shrinking system sizes, along with increasing circuit density, are resulting in rapid growth of volumetric heat generation rate and reduction in surface area for adequate heat dissipation. Moreover, system miniaturization by employing microfabrication technology has had a great influence on thermal and fluid research. Smaller systems have many attractive characteristics and can be more conveniently fabricated using batch production technologies.

One of the fields showing promising potential in microsystems and electronics cooling is the use of the phenomenon of *electrohydrodynamics* or EHD defined as a direct interaction between the electric and hydrodynamic fields where the electric field introduces fluid motion.

The objectives of the present study were to identify the physics of these phenomena as related to the present study, to simulate it numerically, and to verify the

modeling through experiments. More specifically, the goals were to develop a novel numerical methodology to simulate the highly complex interaction between fluid flow and electrical fields. Next, to verify the model a mesoscale ion-injection pump was designed and fabricated, followed by a set of experiments that characterized the pump's performance. The experiments will also demonstrate the application potential of the concept in electronics cooling and particularly for spot cooling applications.

Experimental tests were conducted on an EHD ion-injection mesopump to measure the flow rates and generated pressure heads with HFE -7100 as working liquid. It is shown that the results of two different flow rate measurement techniques that were employed, are in agreement. The experimental results also show that maximum flow rate of about 30 ml/min and pressure head of 270 Pa for the electrode gap of 250 μm and voltage of 1500 V are achievable. A novel numerical modeling method was developed that incorporates both the injection and dissociation of ions. This modeling method is used to simulate the EHD mesopump. The numerical results show a fairly good agreement with experimental data.

EXPERIMENTAL AND COMPUTATIONAL ANALYSIS OF AN
ELECTROHYDRODYNAMIC MESOPUMP FOR SPOT COOLING APPLICATIONS

by

Amir Shoushtari

Dissertation submitted to the Faculty of the Graduate School of the
University of Maryland, College Park in partial fulfillment
of the requirements for the degree of
Doctor of Philosophy
2004

Advisory Committee:

Professor Michael Ohadi, Chair/Advisor
Assistant Professor Elias Balaras
Professor Avram Bar-Cohen
Associate Professor Kenneth Kiger
Professor Gary A. Pertmer

©Copyright by

Amir Shoushtari

2004

Dedication

To my parents for their endless and unconditional love to their children

Acknowledgements

First and foremost I would like to thank my advisor Dr. Michael Ohadi, whom I am indebted to for his encouragement, counsel and support throughout the course of my study and research.

I also extend my appreciation to the other members of my advisory committee who provided constructive advice and guidance, including Dr. Avram Bar-Cohen, Dr. Elias Balaras, Dr. Kenneth Kiger and Dr. Gary A. Pertmer.

During the course of my research, I had the privilege of working with and being advised by several fellow scientists, including Dr. Majid Molki, Dr. Jafar Darabi, Dr. Francis Franca, Dr. John Lawler, Dr. Serguei Dessiatoun and Dr. Jianwei Qi, to whom I wish to express my sincere gratitude.

I would also like to thank Dr. Reza Ghodssi, for his suggestions and interaction, and providing me with the opportunity of productive interaction with his team and access to microfabrication facilities and labs.

I am grateful to my many friends and colleagues at the Smart and Small Thermal Systems Laboratory for providing a stimulating, constructive and fun environment in which to learn and grow. I am especially thankful to Vytenis Benetis, Sourav Chowdhury, Parisa Foroughi, Guohua Kuang, Saeed Moghaddam, Arman Molki, Mihai Catalin Rada, Valentin Tudor and Jianlin Wu.

I would also like to thank my friends in MEMS Sensors and Actuators Lab who helped me in some aspects of microfabrication.

Finally, I wish to thank the AHX/EHD Consortium and ATEC Inc. for their invaluable financial support of this project.

Table of Contents

List of Tables.....	xi
List of Figures.....	xii
Nomenclature.....	xviii
CHAPTER 1: INTRODUCTION.....	1
1.1 Overview.....	1
1.2 Research Objectives.....	4
1.3 Research Approach.....	5
1.4 Scope.....	7
CHAPTER 2: ELECTROHYDODYNAMICS THEORETICAL BACKGROUND.....	9
2.1 Introduction.....	9
2.2 Basic Electrohydrodynamics Definitions.....	9
2.3 Governing Equations.....	10
2.3.1 Electrical Equations.....	10
2.3.1.1 Electrical Conduction and Dissociation.....	12
2.3.1.2 Unipolar Charge Migration.....	14
2.3.2 Fluid Flow Equations.....	15
2.3.3 Joule Heating and EHD Body Forces in Fluids.....	16

2.4	Nondimensional Form of the Governing Equations	19
2.5	Electrohydrodynamic Efficiency.....	21
2.6	Definitions and Physical Concepts.....	23
2.6.1	Polar and Non-polar Liquids	23
2.6.2	Ion Mobility	24
2.6.3	Charged Carrier Generation in Gases.....	25
2.6.3.1	Various processes of Charged Carrier Generation.....	25
2.6.3.2	Corona Discharge and Non-uniform Field Gas Breakdown	28
2.6.4	Charged Carrier Generation in Liquids	32
2.6.5	Current Density-Electric Field Characteristic	34
2.6.6	Charge Decay	36
2.6.6.1	Ohmic Regime.....	36
2.6.6.2	Unipolar Charge Injection Regime	37
2.7	Summary	39
CHAPTER 3: LITERATURE REVIEW		40
3.1	Introduction	40
3.2	A Review of Various EHD Pumping Mechanisms	40
3.2.1	Ion-Injection Pumping Mechanism	41
3.2.2	Traveling Wave-Induced Pumping Mechanism	54
3.2.3	Electro-osmotic Pumping Mechanism	56
3.2.4	Conduction Pumping Mechanism.....	57
3.3	A Review of a Selected Non-EHD Micro Pumping Mechanisms	61

3.4 Numerical Modeling of the Electrohydrodynamics Phenomenon.....	66
3.5 Summary	70
CHAPTER 4: NUMERICAL MODELING	71
4.1 Introduction	71
4.2 Numerical Modeling for Two Classes of Problems	72
4.2.1 Unipolar Charge Injection with Ohmic Conduction.....	72
4.2.1.1 Governing Equations.....	73
4.2.1.2 Boundary Conditions	75
4.2.1.3 Discretisation.....	77
4.2.1.4 Implementation of the Solution Technique to the Fluent Solver	79
4.2.1.5 Numerical Solution Algorithm.....	81
4.2.1.6 Verification of Numerical Modeling Technique.....	82
4.2.2 Dissociation-Injection Process.....	95
4.2.2.1 Governing Equations.....	97
4.2.2.2 Boundary Conditions	99
4.2.2.3 Discretisation, Numerical Solution Algorithm, and Implementation of the Solution Technique with the Fluent Solver.....	100
4.2.2.4 Verification of Numerical Modeling Technique.....	100
4.3 Summary	103
CHAPTER 5: EHD MESOPUMP DESIGN AND FABRICATION	105
5.1 Introduction	105
5.2 Requirements and the Preliminary Design	105

5.3	A Preliminary Ion-Injection Pump Design	108
5.4	Why the Microfabrication Technique for Electrodes?	112
5.5	Mesopump Design	114
5.6	Microfabrication and Packaging Processes	118
5.6.1	Step-by-Step Microfabrication Procedure.....	122
5.6.1.1	Silicon Wafers	122
5.6.1.2	Chromium and Gold Film Deposition.....	124
5.6.1.3	Photolithography to Generate the Pattern of Perforations.....	125
5.6.1.4	Etching the Gold and Chromium Films.....	128
5.6.1.5	Etching the Nitride Layer Using RIE.....	128
5.6.1.6	Photolithography and Wet Etching to Pattern the Bond Pads.....	129
5.6.1.7	Photolithography to Pattern the Wafer Backside Cavity.....	131
5.6.1.8	Etching the Nitride Layer on the Backside of the Wafer Using RIE	132
5.6.1.9	Etching the Oxide Layer on Both Sides of the Wafer	133
5.6.1.10	Etching of Silicon from Both Sides of Wafer	133
5.6.2	Mesopump Packaging Procedure.....	135
5.7	Summary	137

CHAPTER 6: EXPERIMENTAL APPARATUS AND TEST

PROCEDURES	138	
6.1	Introduction	138
6.2	Flow Loop Testing Setup.....	138
6.3	EHD Mesopump Working Fluid	144

6.4 Instruments and Measurement Devices	146
6.5 Experimental Procedure.....	149
6.6 Summary	150
CHAPTER 7: EXPERIMENTAL AND NUMERICAL RESULTS	151
7.1 Introduction	151
7.2 Calibration and Experimental Results.....	151
7.2.1 Flow Loop and Instrument Calibration	151
7.2.1.1 Calibration of Thermocouples.....	151
7.2.1.2 Calibration of Pressure Transducer.....	152
7.2.1.3 Calibration of High-Voltage Power Supply.....	153
7.2.1.4 Calibration of the Flow Loop.....	155
7.2.2 EHD Pumping Experimental Results	163
7.3 Numerical Results.....	167
7.3.1 Modeling of the Ion-Injection Mesopump	168
7.3.2 Design of Multi-stage Mesopump Using the Numerical Modeling	177
7.4 Summary	184
CHAPTER 8: CONCLUSIONS AND RECOMMENDATIONS FOR	
FUTURE WORK	185
8.1 Introduction	185
8.2 Overview and Conclusions	185

8.3 Recommendations	188
8.3.1 Recommendations for Numerical Modeling.....	188
8.3.2 Recommendations for Fabrication of EHD Mesopump.....	192
8.3.3 Recommendations for EHD Mesopump Experimental Test Conditions	194
8.4 Summary.....	197
References	198

List of Tables

Table 2-1 Primary dimensionless parameters based on conservation equations	19
Table 2-2 Additional useful dimensionless parameters	20
Table 3-1 Summary of reported experimental works on the ion-injection pumps	52
Table 5-1 Properties of Silicon Nitride.....	122
Table 5-2 Properties of Thermal SiO ₂	123
Table 5-3 KOH solution recipe	134
Table 6-1 Physical properties of HFE-7100 in comparison with a number of other liquids	145
Table 6-2 Pressure transducer specifications	146
Table 6-3 Data acquisition unit specifications	147
Table 6-4 DC high-voltage power supply	147
Table 6-5 DC power supply specifications.....	148
Table 6-6 Digital multimeter specifications	148
Table 7-1 Value of input parameters.....	172
Table 7-2 Modeling input parameters.....	181
Table 8-1 A comparison of choices of substrate materials	193

List of Figures

Figure 2-1 The main processes responsible for the production of the charged particles in a gas discharge (Malik, Al-Arainy et al. 1998).....	26
Figure 2-2 Negative corona avalanche	30
Figure 2-3 Positive corona avalanche.....	31
Figure 2-4 J-E- characteristic of gases or nonpolar liquids	34
Figure 4-1 Computational grid	78
Figure 4-2. Schematic of one-dimensional unipolar ion-injection pumping.....	83
Figure 4-3 A comparison between numerical and analytical solutions of dimensionless charge density versus dimensionless axial length for one-dimensional unipolar ion-injection process.....	85
Figure 4-4 A comparison between numerical and analytical solutions of dimensionless potential field versus dimensionless axial length for one-dimensional unipolar ion-injection process.....	85
Figure 4-5 A comparison between numerical and analytical solutions of dimensionless pressure head versus dimensionless velocity for one-dimensional unipolar ion-injection process.....	86
Figure 4-6 Wire-plate test-section (Saidi, Moghaddam et al. 2002).....	87
Figure 4-7 Unstructured computational mesh; The computational domain consisted of 38000 cells.....	88
Figure 4-8 Pressure distribution in vicinity of wire and plate electrodes	92
Figure 4-9 Velocity magnitude in vicinity of wire and plate electrodes	92

Figure 4-10 Numerical and experimental velocity profiles on a horizontal axis 8 mm below the wire-T: turbulent model, L: laminar model, FOU: first order upwind scheme, SOU: second order upwind scheme.....	93
Figure 4-11 Numerical and experimental velocity profiles on a horizontal axis 2 mm above the wire-T: turbulent model, L: laminar model, FOU: first order upwind scheme, SOU: second order upwind scheme.....	93
Figure 4-12 Numerical and experimental normal velocity component on the vertical axis of symmetry passing through the wire-T: turbulent model, L: laminar model, FOU: first order upwind scheme, SOU: second order upwind scheme.....	94
Figure 4-13 Numerical velocity profiles using the coarse grid with 38000 cells and fine grid with 57000 cells	94
Figure 4-14 A comparison between result of current model and Pontiga et al. numerical result for total current density (solid line) and dissociation current density (dashed line) as a function of C_0^{-1} for $C_0 \bar{b}^2 = 10^{-2}$ and $A = 1$	103
Figure 5-1 Increasing the number of sharp points on the emitter electrode enhances ion-injection process.....	106
Figure 5-2 The electric intensity at the sharp points depends on their distances from the collector electrode. The electric field intensifies as the emitter sharp points get closer to the collector electrode.	107
Figure 5-3 If the ion-injection points are positioned far away from each other, the electric force will not be uniform. This may result in a recirculation motion of the liquid.	108
Figure 5-4 A preliminary EHD ion-injection pump, (a) dimensional drawing, (b) 3D model	110

Figure 5-5 Fabricated components of an ion-injection EHD pump (preliminary design)	110
Figure 5-6 Static pressure test on the preliminary EHD pump design; the column height of HFE 7100 liquid represents the static pressure generated.	112
Figure 5-7 Direction of ion-injection process around a wire electrode	113
Figure 5-8 Schematic diagram of electrodes of mesopump	115
Figure 5-9 Various layers deposited on the silicon wafer (not to scale)	116
Figure 5-10 Schematic sketch of Pyrex spacer	117
Figure 5-11 Schematic diagram of Mesopump components	118
Figure 5-12 Cross-section of a blank wafer	123
Figure 5-13 Schematic sketch of the wafer cross-section after chromium-gold deposition	125
Figure 5-14 Two CAD drawings of the photomasks used to pattern checkerboard shape windows	127
Figure 5-15 Photoresist is patterned on the wafer front side	127
Figure 5-16 Gold and chromium films are etched	128
Figure 5-17 Nitride layer is etched using RIE technique	129
Figure 5-18 CAD drawing of the photomask used to pattern bond pads	130
Figure 5-19 Chromium and gold layers are etched to form bond pads	131
Figure 5-20 CAD drawing of the photomask used to pattern backside windows and dicing lines	132
Figure 5-21 Photoresist is patterned on the wafer backside and spun on the entire wafer front side	132

Figure 5-22 Silicon nitride film is etched on the backside of wafer	132
Figure 5-23 Wafer cross-section after etching silicon dioxide layers.....	133
Figure 5-24 A schematic sketch of wafer cross-section after silicon wet etching process	135
Figure 5-25 Schematic sketches of electrodes (top), and microfabricated electrodes after dicing (bottom).....	136
Figure 5-26 Mesopump housing and Pyrex spacer.....	136
Figure 5-27 Assembled mesopump.....	137
Figure 6-1 Schematic sketch of closed flow loop.....	140
Figure 6-2 Flow measurement closed loop.....	142
Figure 6-3 Heating element (a) before insulating (b) after insulating	143
Figure 7-1: Thermocouple calibration curve	152
Figure 7-2 Pressure transducer calibration curve	153
Figure 7-3 Voltage calibration curve for high-voltage power supply.....	154
Figure 7-4 Current calibration curve for high-voltage power supply	155
Figure 7-5 A gear pump was used to calibrate the flow measurement technique.....	156
Figure 7-6 The variation of heat loss versus volumetric flow rate	157
Figure 7-7 The calibration curve for the thermal based volumetric flow rate measurement technique.....	158
Figure 7-8 The calibration curve for the thermal based volumetric flow rate measurement technique in terms of dimensionless numbers	158
Figure 7-9 The flow loop pressure drop versus the volumetric flow rate	159
Figure 7-10 The flow loop dimensionless pressure drop versus the Reynolds number ..	159

Figure 7-11 A thermal resistance network for analytical modeling.....	161
Figure 7-12 A comparison between analytical modeling and experimental results for flow measurement.....	163
Figure 7-13 A comparison between analytical and experimental results for flow measurement calibration curve	163
Figure 7-14 EHD pump-generated pressure versus applied voltage.....	164
Figure 7-15 EHD mesopump electrical current versus applied voltage	165
Figure 7-16 EHD mesopump volumetric flow rate versus applied voltage	166
Figure 7-17 EHD mesopump efficiency versus applied voltage.....	167
Figure 7-18 Computational domain of solution: (a) side view (b) top view	169
Figure 7-19 Surface boundaries surrounding the computational domain.....	171
Figure 7-20 Numerical modeling and experimental results for the static pressure versus voltage	173
Figure 7-21 Numerical modeling and experimental results for the electrical current versus voltage	174
Figure 7-22 Distribution of the dimensionless electrical potential.....	176
Figure 7-23 Distribution of dimensionless positive charge density.....	176
Figure 7-24 Distribution of dimensionless negative charge density.....	177
Figure 7-25 Schematic of a three-stage ion-injection pump; Electrodes 1, 3 and 5 are emitters and electrodes 2, 4 and 6 are collectors.	178
Figure 7-26 Numerical model consisting of two emitter electrodes (E_1 , E_2) and one collector electrode (C_1).....	180

Figure 7-27 Numerical modeling results of the dimensionless pressure head per total length (left) and pressure head ratio (right) versus $x=S/L$	182
Figure 7-28 Numerical modeling results of the dimensionless pressure head per total length (left) and pressure head ratio (right) versus $x=S/L$ for two different voltages $\phi_0=1000$ ($C_0 = 0.3607$) and $\phi_0=1500$ ($C_0 = 0.2404$)	183

Nomenclature

a	size of ion (m)	\mathbf{J}'	Electric current density due to movement of charge carriers (A/m^2)
b	Dimensionless parameter defined by Eq. (2 17)	\mathbf{J}^+	Electric current density of positive species (A/m^2)
B	A constant factor in Eq. (2 40), $0.441 [\text{K}(\text{m}/\text{V})^{1/2}]$	\mathbf{J}^-	Electric current density of negative species (A/m^2)
\mathbf{B}	Magnetic induction [$(\text{N}\cdot\text{s})/(\text{C}\cdot\text{m})$]	k	Boltzmann constant, $1.38 \times 10^{-23} (\text{J}/\text{K})$
c	Density of ionic pairs (C/m^3) ²	k_d	Dissociation constant [$\text{m}^3/(\text{C}\cdot\text{s})$]
c_p	Specific heat [$\text{J}/(\text{kg}\cdot\text{K})$]	k_d^0	Dissociation constant without electric field [$\text{m}^3/(\text{C}\cdot\text{s})$]
D_e	Diffusion coefficient (m^2/s)	k_r	Recombination constant [$\text{m}^3/(\text{C}\cdot\text{s})$]
D_i	Molecular diffusion of charge specie i	K	Empirical constant in Eq. (2 42)
\mathbf{D}	Electric displacement (C/m^3)	l_B	Bjerrum distance (m)
e_0	Absolute value of electric charge, $1.6 \times 10^{-19} (\text{C})$	L	Length scale (m)
E_0	Empirical constant in Eq. (2 42) (kV/cm)	\mathbf{n}	Unit normal surface vector
E_C	Corona electrical field intensity onset (kV/cm)	p	Pressure (Pa)
\mathbf{E}	Electric field intensity (V/m)	P	EHD input power (W)
\mathbf{F}_e	Electric body force (N/m^3)	\mathbf{P}	Polarization vector (C/m^3)
g, \mathbf{g}	Gravitational acceleration (m/s^2)	S_j	Joule heating source term (W/m^3)
G_e	Thermophoresis coefficient	t	Time (s)
\mathbf{H}	Magnetic field intensity (A/m)	T	Temperature (K)
I	Electrical current (A)	\mathbf{u}	Velocity of fluid or medium (m/s)
\mathbf{J}	Electric current density (A/m^2)	W	height of the potential barrier above the Femi level of the metal (eV)

Greek Letters

α	Thermal diffusivity of fluid (m^2/s)	$\rho_{e,inj}^0$	Injected charge density in absent of the electric field (C/m^3)
β	Thermal expansion coefficient (K^{-1})	ρ_e^+	Electric volume charge density of positive charge (C/m^3)
d	Relative air density factor	ρ_e^-	Electric volume charge density of negative charge (C/m^3)
ε	Electric permittivity (F/m)	\mathbf{s}_e	Electric conductivity (S/m)
ε_0	Permittivity of free space, $8.86 \times 10^{-12} (\text{F}/\text{m})$	ϕ	Electric potential (V)
\mathbf{e}_r	Dielectric constant (F/m)	Φ	Viscous dissipation ($1/\text{s}^2$)
\mathbf{e}_s	Specific dielectric constant $= \varepsilon / \varepsilon_0$		
h	Efficiency		
l_D	Debye length $= (\mathbf{e}_0 kT / e_0 \mathbf{r}_e)^{1/2} (\text{m})$		
l_H	Heterocharge layer thickness (m)		
μ	Dynamic viscosity of fluid ($\text{Pa}\cdot\text{s}$)		
μ_m	Magnetic permeability $[(\text{N}\cdot\text{S}^2)/\text{C}^2]$		
$\mu_{e,i}$	Mobility of charge specie i ($\text{m}^2/\text{V}\cdot\text{s}$)		
μ_e^+	Mobility of positive charge specie ($\text{m}^2/\text{V}\cdot\text{s}$)		
μ_e^-	Mobility of negative charge specie ($\text{m}^2/\text{V}\cdot\text{s}$)		
n	Kinematic viscosity of fluid (m^2/s)		
ρ	Fluid density (kg/m^3)		
ρ_e	Electric volume charge density (C/m^3)		
ρ_e^0	Charge density of ions at the thermodynamic equilibrium (C/m^3)		
$\rho_{e,i}$	Electric volume charge density of specie i (C/m^3)		
$\mathbf{r}_{e,inj}$	Injected charge density (C/m^3)		

CHAPTER 1: INTRODUCTION

1.1 Overview

Extensive research has been carried out for years on the development of novel and efficient techniques for the enhancement of heat transfer and mass transport of fluids. Indeed heat, momentum, or mass transport enhancement is a diverse and complex area where many methods have been developed, and while some of them have been commercialized, many techniques are still in the laboratory stages, where commercialization is their major challenge.

During the past decade two emerging topics have had a great impact on the research in this area. The first topic is thermal issues in electronics. As electronic products become faster, more compact, and incorporate greater functionality, their thermal management becomes increasingly challenging. In fact, shrinking system sizes, along with increasing circuit density, are resulting in rapid growth of volumetric heat generation rates and reduction of heat dissipative surfaces. Moreover, the reliable range of operation in terms of temperature for most of these electronic devices has remained in the range of 70°C to 150 C for most applications. Additional thermal management challenges arise if the electronics products operate in harsh environments. In addition, the prospect of using conventional cooling techniques for future products is not very promising. The size of heat sinks cannot increase much beyond their current size because of the desire to shrink chassis size. The cooling airflow rate that may be supplied is limited by the space that is available for fans or blowers and by strict acoustic emission

standards. These factors, plus the need for a severe product cost reduction, have resulted in a strong demand for effective compact heat removal techniques. This demand arises not only in the context of high-speed computers but also, for example, in next-generation portable electronics, biomedical devices, and automotive applications. Although there is debate on the change in the rate of heat generation of future electronics, there is no disagreement that thermal management in future systems will be a more challenging issue. A major result of these challenges in the field of heat transfer has been to define new boundaries for the commercialization possibilities of various heat removal techniques. Many techniques which in the past were not considered commercially viable by industries such as refrigeration, process, and automation sectors are now finding innovative applications in the related electronic packaging areas. This has also boosted new research activities in heat transfer and fluid flow fields.

The second trend that has had a great influence on thermal and fluid research is the tendency toward system miniaturization including use of microfabrication technologies. Smaller systems have many attractive characteristics. They generally have a faster response than their macro-size counterparts. They are typically lighter, less expensive, and more sensible to an external incitation. They can be more conveniently fabricated using batch production technologies. Furthermore, in special cases, using miniaturized systems is unavoidable due to the existence of space or weight constraints. As a result, miniaturized mechanical devices are becoming more prevalent both in commercial applications and in scientific inquiry. The process of miniaturization is not simply the shrinking down of existing systems, but a complete restructuring of the microsystem. Microsystems tend to behave differently from the objects we are used to

handling in our daily life (Karniadakis and Beskok 2002). Great interest in miniaturization has led to the definition and development of a new research area known as *microelectromechanical systems* (MEMS) which involves coupled field behavior combining two or more energy domains such as mechanical, electrical, optical, or thermal (DeVoe 2002). These devices are miniature embedded systems involving one or many micromachined components or structures.

System miniaturization has drastically revolutionized fundamental, experimental, and technological research. In fundamental study, phenomena of negligible importance in the macrosystems might need to be taken into consideration for microdevices or vice versa. For example, for microsystems the inertial forces tend to be quite small, while surface effects tend to dominate the behavior of these systems. Friction, electrostatic forces, and viscous effects due to the surrounding air or liquid become increasingly important as the devices become smaller. In general, quantities that are a function of the area decrease more gradually than properties that depend on the volume (Karniadakis and Beskok 2002). Because of the extensive challenges existing in experimental analysis of microsystems, miniaturization provides an extensive research opportunity for analytical and numerical modeling as well. In fact, modeling plays a great role in design of microdevices.

Experimental research on microsystems has also been carried out in recent years to characterize their behavior and response. However, it has turned out that instrumentation is one of the main challenges in this area. In fact, microsystems are very vulnerable to environmental disturbances. It is difficult to design and utilize measurement

techniques and instruments that are non-intrusive, have a limited range of stochastic errors, and are adequately sensitive.

Technology development in microdevice production has been dependent on microfabrication techniques. Microfabrication is the set of design and fabrication tools for the machining of microstructures and very small mechanical features well below the limits of human perception (Maluf 2000). While many fundamental processes of microfabrication technology were originally introduced by the integrated circuit industry, the MEMS community has tremendously improved microfabrication techniques in recent years.

To summarize, electronics thermal management and miniaturization have greatly motivated recent research in heat and fluid flow field, while microfabrication has provided a superb practical technique to realize design miniaturization. This introduction was given to establish the motivations for the objectives and scopes sought in the current study which will be addressed next.

1.2 Research Objectives

As indicated, in many MEMS devices and miniaturized systems several different energy fields simultaneously play a role. For example, in a microsensor, micromechanical and electrical components might function side by side. In fact, a major advantage of miniaturized systems is their integration of various energy fields (e.g. mechanical, electrical, optical, etc.) on the same platform.

One of the fields showing promising potential in microsystems is *electrohydrodynamics*, or the EHD technique for fluid pumping and transport phenomenon applications. Electrohydrodynamics can be defined as a direct interaction

between the electric and hydrodynamic fields where the electric field introduces fluid motion. This physical phenomenon, which will be defined precisely in following chapters, is a complex field. The major objectives of the present study can be listed as follows:

1. Study the concept of the electrohydrodynamics for microfluidics applications, identify key factors, and classify governing equations
2. Develop a novel numerical methodology to simulate the corresponding electrohydrodynamics phenomenon (i.e. the interaction between fluid flow and electrical fields)
3. Design and fabricate an electrohydrodynamic pump with two sub-goals:
 - a. Verify the developed numerical methodology in practice
 - b. Demonstrate the application potential of the electrohydrodynamics phenomenon in electronic cooling using microfabrication techniques

1.3 Research Approach

In this section it is intended to present an overview of the research track that was chronologically followed to meet the project goals.

The current study was started with a conceptual study of the EHD phenomenon involved in the current application. In this stage the physics of EHD were broadly studied to understand the process, how the fluid and electric fields interact, and which media properties play important roles. Then, the governing equations and mathematical formulation of the fields and the boundary conditions were classified, leading to an understanding of how the EHD equations are coupled and how they interact.

The next stage was to develop a numerical strategy to solve the governing equations simultaneously and simulate the EHD process. The initial modeling methodology was specially adopted to simulate the EHD heat transfer enhancement in gases. This task was carried out by discretizing the governing equations and writing a 2-D numerical program to solve these equations numerically. After concluding that the modeling strategy was successful, the same technique was adopted for *Fluent*, a commercial 3-D CFD code. *Fluent* offers great flexibility in modeling of practical problems where the geometries are fairly complex. Moreover, *Fluent* provides a convenient feature known as *User-Defined Functions* (UDF). A UDF is a routine programmed by a user that can be dynamically loaded with the *Fluent* original solver to enhance the standard feature of the code. Even though *Fluent* presents great advantages in handling of fluid mechanics problems, it does not have any built-in function to solve electrostatic equations. Nevertheless, the *Fluent* UDF feature allowed us to extend the capability of the code to handle the electrostatic equations as well. This was not an effortless task since it was necessary to translate these equations and their boundary conditions to the general form of transport equations and boundary conditions that could be solved by the code. Besides, an advanced knowledge of the *Fluent* user-defined macros was needed.

In the next stage the numerical simulation methodology was verified. To do this, a basic macroscale test section was designed to demonstrate single phase fluid pumping application using air as the working fluid, with applications in air-side heat transfer enhancement. After a number of experiments were conducted, the results were compared with the numerical results and agreement of the results was found promising. However,

realizing the practical application of the EHD for air-side heat transfer enhancement at the macroscale is limited, predominantly due to relatively high Joule heating and the associated power consumption, it was decided to next examine the applicability for fluid pumping applications, including its use in micro pumping and spot cooling of high flux electronics. Therefore, at the next stage a meso-scale, ion-drag, EHD pump was designed and manufactured. In order to build the meso-pump, a microfabrication technique was utilized, with nearly all its steps being carried out in the University of Maryland research labs. Although some basic hydrostatic tests were conducted that showed the applicability of the EHD pumping concept, it was decided to design a complete closed-loop test section and to run a number of tests in this test section to evaluate the performance of the EHD meso-pump with microfabricated electrodes. Then, using the developed simulation methodology, a numerical model of the meso-pump was generated and a comparison between the numerical and experimental results was carried out.

1.4 Scope

In Chapter 2 the electrohydrodynamics concepts and governing equations will be presented and the terminology, as well as definitions of some basic terms and physical concepts, will be reviewed. Chapter 3 provides a comprehensive literature review on some of the earlier works on micropumps as well as basic research on the EHD phenomena and its applications as related to the present work. The methodology of numerical modeling for electrohydrodynamic processes will be presented in Chapter 4. For the numerical modeling, two classes of EHD problems will be simulated. In both classes, the source of motion is the Coulombic force acting on the fluid. However, the difference is in the type of charged carriers participating in the EHD process. The design

of EHD mesopump and its fabrication methodology will be reviewed in Chapter 5. In this chapter an appropriate scheme for mesopump microfabrication and its process flow will be studied. In Chapter 6 the experimental setup and test facilities used in current study will be introduced. The experimental and numerical results of current research will be presented in Chapter 7. Finally, an overview of the results and recommendations for future work will be given in Chapter 8.

CHAPTER 2: ELECTROHYDODYNAMICS THEORETICAL

BACKGROUND

2.1 Introduction

In this chapter the relevant electrohydrodynamics concepts will first be briefly defined and be followed with the governing equations in their general form. These equations will be simplified to obtain a useful and practical set of equations, and then will be nondimensionalized. Afterward, terminology, as well as definitions of some basic terms and physical concepts, will be reviewed. This chapter will facilitate coverage of corresponding equations for numerical modeling which will be more specifically discussed in Chapter 4.

2.2 Basic Electrohydrodynamics Definitions

Electrohydrodynamics (EHD) is a field of science that studies the fluid flow behavior under the influence of electric fields. In other words, EHD deals with the interaction between the electric field and fluid flow. This interaction can result in different phenomena such as mixing, pumping, secondary motion, agitation, and heat transfer enhancement. The generated fluid motion is due to an electrical body force exerted on the fluid under certain conditions that will be discussed in next sections.

2.3 Governing Equations

2.3.1 Electrical Equations

The EHD governing equations are deduced from two basic sets of equations, Maxwell's equations and fluid flow conservative equations. Maxwell's equations are the general electromagnetism equations (Castellanos 1998). Under special circumstances, these equations can be simplified to form the electrical governing equations in electrohydrodynamics.

Gauss's law states that

$$\nabla \cdot \mathbf{D} = \mathbf{r}_e \quad (2-1)$$

where \mathbf{D} is the displacement vector and defined as $\mathbf{D} = \epsilon_0 \mathbf{E} + \mathbf{P}$.

The nonexistence of magnetic charges implies that

$$\nabla \cdot \mathbf{B} = 0 \quad (2-2)$$

If the magnetic field is time dependent, Faraday's law states that

$$\nabla \times \mathbf{E} = -\frac{\partial \mathbf{B}}{\partial t} \quad (2-3)$$

The fourth law tells us

$$\nabla \times \mathbf{H} = \mathbf{J} + \frac{\partial \mathbf{D}}{\partial t} \quad (2-4)$$

where \mathbf{J} is the current density due only to the free charge carriers that are convected through the fluid under the action of the electric field. As constitutive relations, it can be assumed that $\mathbf{D} = \epsilon \mathbf{E}$, $\mathbf{B} = \mu_m \mathbf{H}$.

In the case that electric energy is greater than the magnetic energy (electroquasistatics), the above equations can be simplified to (see (Melcher 1981))

$$\nabla \cdot \mathbf{D} = \rho_e, \quad \nabla \times \mathbf{E} = 0 \quad (2-5)$$

$$\nabla \cdot \mathbf{B} = 0, \quad \nabla \times \mathbf{H} = \mathbf{J} + \frac{\partial \mathbf{D}}{\partial t} \quad (2-6)$$

From the irrotational nature of electric field it is concluded that

$$\mathbf{E} = -\nabla\phi \quad (2-7)$$

where ϕ is the electric potential.

The charge conservation law implies that

$$\frac{\partial \rho_e}{\partial t} + \nabla \cdot \mathbf{J} = 0 \quad (2-8)$$

where the electric current density, \mathbf{J} , is defined as

$$\mathbf{J} = \mathbf{J}' + \rho_e \mathbf{u} \quad (2-9)$$

The first term represents the summation of all current densities measured by an observer moving with a volume element inside the medium, while the second term stands for the current density due to the bulk movement of charge carriers with the medium. It can be shown that (Castellanos 1998)

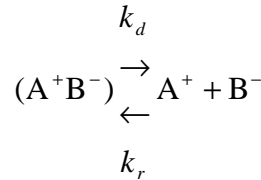
$$\mathbf{J}' = \sum_i (\mu_{e,i} \rho_{e,i} \mathbf{E} + D_i \nabla \rho_{e,i}) \quad (2-10)$$

where $\mu_{e,i}$, D_i , and $\rho_{e,i}$ are mobility, molecular diffusion coefficient, and charge density of charge specie i , respectively (see section 2.6.2 for a definition of the ion mobility). It can be proved that the effect of diffusion may be safely neglected unless the electric field

is as low as 0.025 V/m (see (Castellanos 1998)) . In next two sections, two special cases will be reviewed, and the law of charge conservation for these two cases will be presented.

2.3.1.1 Electrical Conduction and Dissociation

One important phenomenon observed in liquids is electrical conduction, which is due to the dissociation of either neutral, impure molecules inside the liquid or the liquid molecules themselves into ions. If we only consider the liquid molecules' dissociation, using a simple model, we have:



(2-11)

where (A^+B^-) stands for the neutral ionic pairs, while A^+ and B^- represent the positive and negative ions, respectively (Pontiga and Castellanos 1996). This equation shows that the free ions are continuously generated from the dissociation of ionic pairs, and conversely, the ionic pairs are formed by a recombination of the positive and negative ions. k_d and k_r are the dissociation and recombination coefficient, respectively.

Now the charge conservation equation for each charge polarity is

$$\frac{\partial \mathbf{r}_e^+}{\partial t} + \nabla \cdot \mathbf{J}^+ = k_d c - k_r \mathbf{r}_e^+ \mathbf{r}_e^-$$

(2-12)

$$\frac{\partial \mathbf{r}_e^-}{\partial t} + \nabla \cdot \mathbf{J}^- = k_d c - k_r \mathbf{r}_e^+ \mathbf{r}_e^-$$

(2-13)

where c is the concentration of ionic pairs, and r_e^+ and r_e^- are the concentration of cations (positive ions) and anions (negative ions) (Pontiga and Castellanos 1996). The current flux density is given by

$$\mathbf{J}^\pm = \pm m_e^\pm r_e^\pm \mathbf{E} + r_e^\pm \mathbf{u} \quad (2-14)$$

Notice that Eqs. (2-5) to (2-10) are all still valid considering that $r_e = r_e^+ - r_e^-$ and $\mathbf{J} = \mathbf{J}^+ - \mathbf{J}^-$. In nonpolar liquids (see section 2.6.1 for the definition) the concentration of free ions to ionic pairs is extremely low.

The recombination coefficient, k_r , can be obtained by

$$k_r = \frac{(m_e^+ + m_e^-)}{e} \quad (2-15)$$

with m_e^+ and m_e^- representing the mobility of cations and anions, and e the liquid permittivity (Castellanos 1998). Unlike the recombination coefficient for the nonpolar liquids, the dissociation coefficient is a function of the electric field intensity. In fact, the rate of dissociation of ionic pairs can be substantially increased by the application of an electric field. This coefficient is given as

$$k_d = k_d^0 \frac{I_1(4b)}{2b} \quad (2-16)$$

where k_d^0 is the rate of dissociation of ionic pairs when no electric field is present, and I_1 is the modified Bessel function of first kind and order one. b is defined as

$$b = \frac{L_B}{L_E} = \frac{e_0^2 / 8\pi\epsilon kT}{\sqrt{e_0 / 4\pi\epsilon |\mathbf{E}|}} \quad (2-17)$$

In the limit, the dissociation coefficient tends to the constant value k_d^0 , since

$\lim_{b \rightarrow 0} I_1(4b)/2b = 1$. Notice that b is a function of electric field.

At the thermodynamic equilibrium and in the absence of an external electric field, the rate of positive and negative ion generation is zero, and the densities of positive and negative ions are identical. Therefore, from Eqs. (2-12) and (2-13) it can be concluded that

$$\frac{k_r}{k_D^0} = \frac{c}{(\rho_e^0)^2} \quad (2-18)$$

where $\rho_e^0 = \frac{\sigma_e}{(\mu_e^+ + \mu_e^-)}$ and σ_e the ohmic electrical conductivity. This relation enables us

to find the density of ionic pairs, c , in terms of other given parameters.

2.3.1.2 Unipolar Charge Migration

As suggested by Melcher (Melcher 1981), if only unipolar charge migration and ohmic conduction are present, and the variation of ohmic conduction with electric field is negligible, the total current density can be found as

$$\mathbf{J} = \mathbf{m}_e \mathbf{r}_e \mathbf{E} + \mathbf{s}_e \mathbf{E} + \mathbf{r}_e \mathbf{u} \quad (2-19)$$

where the terms on the right-hand side represent the unipolar charge migration and conduction and convection components, respectively. The unipolar charge migration current density component is due to the flow of free ions (positive or negative) injected into the field through the electrodes. The term $\mathbf{m}_e \mathbf{E}$ shows the velocity of these charge carriers, while \mathbf{r}_e represents their volume density. The conduction term is due to the

current flow of charged carriers that are produced not by injection process, but by the dissociation of molecules within the field. This process always creates an equal number of positive and negative charges. However, redistribution of the positive and negative charges can occur, creating locally charged regions, even if the entire fluid domain as a whole in the electric field is neutral (Seyed-Yagoobi and Bryan 1999). The convection current density component is a result of the free charge carrier translation with the medium (e.g. fluid) moving with a velocity of \mathbf{u} .

2.3.2 Fluid Flow Equations

The basic equations for an incompressible, Newtonian fluid under the influence of an electric field are as follows (Davidson, Kulacki et al. 1987):

Conservation of mass:

$$\nabla \cdot \mathbf{u} = 0 \quad (2-20)$$

Navier-Stokes equations with an electric body force term \mathbf{F}_e :

$$\rho \left[\frac{\partial \mathbf{u}}{\partial t} + (\mathbf{u} \cdot \nabla) \mathbf{u} \right] = -\nabla p - \nabla \cdot \mathbf{t} + \rho \mathbf{g} + \mathbf{F}_e \quad (2-21)$$

where for an incompressible Newtonian fluid

$$-\nabla \cdot \mathbf{t} = \mu \nabla^2 \mathbf{u} \quad (2-22)$$

and an energy equation for an incompressible fluid subject to Joule heating source term,

S_J :

$$\frac{\partial T}{\partial t} + \mathbf{u} \cdot \nabla T = \nabla \cdot (\alpha \nabla T) + \frac{\nu}{c_p} \phi + \frac{S_J}{\rho c_p} \quad (2-23)$$

The interaction between the electric and fluid fields is through the body force term \mathbf{F}_e and the Joule heating source term S_J , which will be defined in the next section.

2.3.3 Joule Heating and EHD Body Forces in Fluids

As explained, when an electrostatic force is applied to a fluid, it can result in an EHD body force as well as the Joule heating phenomenon. The calculation of the electric body force is a complicated problem, since any attempt to deduce this force from a microscopic model and subsequent averaging has been unsuccessful. The technique, which is mainly used to drive this body force, is based on an energy principle. Using this method, it can be shown that the electric body force acting on the fluid is

$$\mathbf{F}_e = \mathbf{r}_e \mathbf{E} - \frac{1}{2} E^2 \nabla \mathbf{e} + \frac{1}{2} \nabla \left[E^2 \mathbf{r} \left(\frac{\partial \mathbf{e}}{\partial \mathbf{r}} \right)_T \right]$$

(2-24)

(Stratton 1941; Castellanos 1998).

The three terms in Eq. (2-24) represent different types of forces acting on the fluid. The first term, called the *electrophoretic* force, corresponds to the Coulomb force acting on the *free* charges in presence of an electric field. This term does not include the force acting on the dipole molecules, which are not free charges. The charge density in this term, \mathbf{r}_e , is considered as the ensemble average of all free charge carriers, including both positive and negative ions. The direction of this component of the electric force for the cations is co-directional with the electric field (i.e. from the positive electrode toward the negative electrode), while for the inions it is in an opposite direction. Therefore, a DC electric field will generate unidirectional Coulombic motion of the charge carrier, while an AC field may generate oscillatory motion of charges. The second and third terms are

known as the *dielectrophoretic* and *electrostrictive* forces, respectively. If the electric field is uniform, the forces on the two separated charges, which form a dipole molecule, cancel out. In a nonuniform field, the force on one of the dipole charges located at a more intense electric field exceeds the force on the other charge, and as a result, the dipole is drawn toward the direction of increasing electric field strength. This effect is governed by the second and third terms in Eq. (2-24).

These two force components are generally more important in a two-phase flow; in a single-phase flow their effect can typically be ignored. Nevertheless, there are two ways in which a single-phase fluid can support a concentration of polarization: when the permittivity (or dielectric constant) of fluid is a function of position, and when the fluid permittivity varies with density.

In fact, if a dielectric liquid is elastically deformed under the force exerted by an electric field, or an interface exists (e.g. two-phase fluids), the dielectrophoretic and electrostrictive forces must be taken into consideration. Notice that in the last term of Eq. (2-24) the electrostrictive force is a gradient term. Therefore, in most cases for a single phase flow, this component of body force does not influence the flow fluid, but, only changes the pressure field. In order to clarify the direction of dielectrophoretic force, let's consider three different examples. For the first example we consider a single-phase flow for which permittivity increases with electric field. According to Eq. (2-24), the direction of the dielectrophoretic force is from the high strength electric field region to the low strength field region. For the second example consider an interface between a liquid and vapor in a nonuniform electric field. In this condition an attraction force is created that draws the fluid of higher permittivity (liquid) toward the region of higher electric field

strength. As the final example, consider the case where a particle is moving under a nonuniform electric field influence in a fluid. If the permittivity of the particle is larger than the surrounding fluid (e.g., a glass particle surrounded by air), as a result of the dielectrophoretic force, the particle moves toward the higher electric field region. However, if the permittivity of the particle is smaller than the surrounding fluid (e.g. a vapor bubble surrounded by a liquid), the dielectrophoretic force drives the particle toward the lower electric field region.

In order to avoid the singularity of the electrical permittivity in Eq.(2-24) at the interface of two-phase media, the Maxwell stress tensor associated with the EHD body force can be used:

$$\mathbf{t}_{ij} = \epsilon E_i E_j - \frac{\epsilon}{2} \mathbf{d}_{ij} E_k E_k \left[1 - \frac{\mathbf{r}}{\epsilon} \left(\frac{\partial \epsilon}{\partial \mathbf{r}} \right)_r \right] \quad (2-25)$$

(Seyed-Yagoobi and Bryan 1999). Notice that the EHD body force given in Eq.(2-24) can be obtained from the transformation of surface force densities given by Eq.(2-25) to volume force densities by applying Gauss's theorem.

The effect of EHD on conservation of energy is fairly complex. However, if the secondary effects, such as thermoelectric phenomena, variation of fluid property with electric field, and dependency of permittivity on temperature, are ignored, then the simplified energy conservation equation as given by Eq. (2-23) is applicable and the Joule heating source term is defined as

$$S_j = \mathbf{E} \cdot \mathbf{J}' \quad (2-26)$$

where \mathbf{J}' is defined by Eq. (2-10), and for a fluid with the unipolar charge migration and ohmic conduction we have

$$S_J = \mathbf{m}_e \mathbf{r}_e E^2 + \mathbf{s}_e E^2 \quad (2-27)$$

2.4 Nondimensional Form of the Governing Equations

Nondimensionalization of the EHD governing equations results in the standard group of dimensionless parameters, including the Reynolds, Prandtl, Eckert, and Nusselt numbers. In addition to these well-known parameters, the electric field effect introduces a new set of dimensionless parameters. A review of the open literature shows that in the past there were discrepancies among researchers on the definition of the EHD dimensionless parameters and the terminologies used. Therefore, the Institute of Electrical and Electronics Engineers- Dielectrics and Electrical Insulation Society- Electrohydrodynamics (IEEE-DEIS-EHD) Technical Committee has recommended using a set of standard dimensionless parameters based on the fundamental governing conservation equations (IEEE-DEIS-EHD Technical Committee 2003). These parameters are summarized in Table 2-1.

Table 2-1 Primary dimensionless parameters based on conservation equations

Symbol	Expression	Name
Re	LU_0/\mathbf{n}	Reynolds Number
E_{hd}	$\mathbf{r}_{e,0} E_0 L^3 / \mathbf{r} \mathbf{n}^2$	EHD Number (Conductive Electric Rayleigh Number)
Md	$\mathbf{e}_0 E_0^2 L^2 / \mathbf{r} \mathbf{n}^2$	Masuda Number (Dielectric Electric Rayleigh Number)
$E_{i\epsilon T}$	$\epsilon_0 E_0^2 L^2 (\partial \epsilon_s / \partial \rho)_T / \nu^2$	Thermo-Dielectric Rayleigh Number
Sc_i	\mathbf{n} / D	Ion Schmidt Number
Fe	$\mathbf{m}_e E_0 L / D$	Ion Drift Number
σ_T	$G_e T_0 / D$	Thermophoresis Number
Ra	$\mathbf{b} g \Delta T_0 L^3 / \mathbf{n}^2$	Rayleigh Number

Pr	n/a	Prandtl Number
Ec	$U_0^2 / C_p T_0$	Eckert Number
Db	$(L/l_D)^2$	Debye Number

(From (IEEE-DEIS-EHD Technical Committee 2003))

There are several other dimensionless parameters that can be expressed by a combination of nondimensional parameters given in Table 2-1. A few of these parameters and their relationship with the standard dimensionless parameters are given in Table 2-2.

Table 2-2 Additional useful dimensionless parameters

Symbol	Expression	Name	Relationship with Standard Dimensionless Parameters
τ	$U_0 t / L$	Mechanical Convection	t
Re_e	$e U_0 / s_e L$	Electric Reynolds	$\epsilon_s Re Sc_i / Db$
τ_r	$t s_e / e$	Charge Relaxation Time	$\tau Db / \epsilon_s Re Sc_i$
τ_E	$t r_e m_e / e$	Space Charge Decay	$\tau Db / \epsilon_s Re Sc_i$

Now using these dimensionless parameters, the nondimensional form of the governing equations can be derived. The dimensionless Gauss equation (i.e. Eq. (2-1)) is

$$\nabla^* \cdot (\mathbf{e}_s \mathbf{E}^*) = \frac{E_{hd}}{Md} \mathbf{r}_e^* \quad (2-28)$$

For the charge conservation equation, given in Eq. (2-8), we have

$$\frac{\partial \mathbf{r}_e^*}{\partial t^*} + \frac{F_E}{E_{hd} \cdot Re \cdot Sc_i} \nabla^* \cdot \mathbf{J}^* = 0 \quad (2-29)$$

The dimensionless current density is defined as

$$\begin{aligned} \mathbf{J}^* &= \frac{L^3}{rn^2 m_e} \mathbf{J} \\ &= \mathbf{J}'^* + \frac{Re Sc_i E_{hd}}{F_E} \mathbf{r}_e^* \mathbf{u}^* \end{aligned}$$

(2-30)

where for the unipolar charge migration along with ohmic conduction we have

$$\begin{aligned}\mathbf{J}'^* &= \frac{L^3}{rn^2 m_e} \mathbf{J}' \\ &= E_{\text{hd}} \mathbf{r}_e^* \mathbf{E}^* + \frac{\text{ReSc}_i \text{Md}}{\text{Re}_e F_E} \mathbf{E}^*\end{aligned}$$

(2-31)

Notice that Re_e is not a primary dimensionless parameter. However, using Table 2-2 it

can be converted to a combination of primary dimensionless parameters.

Nondimensionalization of the momentum equation, Eq.(2-21), yields

$$\left[\frac{\partial \mathbf{u}^*}{\partial t^*} + (\mathbf{u}^* \cdot \nabla^*) \mathbf{u}^* \right] = -\nabla^* p^* + \frac{1}{\text{Re}} \nabla^{*2} \cdot \mathbf{u}^* + \mathbf{g}^* + \mathbf{F}_e^*$$

(2-32)

where the dimensionless EHD body force is

$$\begin{aligned}\mathbf{F}_e^* &= \frac{L \mathbf{F}_e}{\rho U_0^2} \\ &= \frac{E_{\text{hd}}}{\text{Re}^2} \rho_e^* \mathbf{E}^* - \frac{\text{Md}}{\text{Re}^2} \frac{1}{2} E^{*2} \nabla^* \epsilon_s + \frac{E_{\text{leT}}}{\text{Re}^2} \frac{1}{2} \nabla^* \left[E^{*2} \rho^* \left(\frac{\partial \epsilon}{\partial \rho} \right)_T \right]\end{aligned}$$

(2-33)

Likewise, for the energy equation given by Eq. (2-23), we have

$$\frac{\partial \theta^*}{\partial t^*} + \mathbf{u}^* \cdot \nabla^* \theta^* = \frac{1}{\text{Pr Re}} \nabla^{*2} \theta^* + \frac{\text{Ec}}{\text{Re}} \phi^* + \frac{\text{Ec} F_E}{\text{Re}^3 \text{Sc}_i} \mathbf{E}^* \cdot \mathbf{J}'^*$$

(2-34)

2.5 Electrohydrodynamic Efficiency

An important factor in EHD study is the efficiency of the process. The power applied to an EHD-driven system, does not convert entirely into useful work. If the electrohydrodynamic process is employed to generate fluid motion, then the useful portion of input power is the one which is converted to kinetic energy. The rest of the

energy will be dissipated in the form of heat. To find the kinetic energy conservation equation, we can multiply the Navier-Stokes equation (Eq. (2-22)) by \mathbf{u} to obtain

$$\rho \frac{D}{Dt} \left(\frac{1}{2} u^2 \right) = -\mathbf{u} \cdot \nabla p - \mathbf{u} \cdot \nabla \cdot \mathbf{t} + \rho \mathbf{u} \cdot \mathbf{g} + \mathbf{u} \cdot \mathbf{F}_e \quad (2-35)$$

The contribution of viscous work can be divided into two terms, and the kinetic energy equation can be rewritten as

$$\rho \frac{D}{Dt} \left(\frac{1}{2} u^2 \right) = -\nabla \cdot p \mathbf{u} - (\nabla \cdot [\mathbf{t} \cdot \mathbf{u}]) - \mu \phi + \rho \mathbf{u} \cdot \mathbf{g} + \mathbf{u} \cdot \mathbf{F}_e \quad (2-36)$$

The right hand side of the kinetic energy equation consists of five terms. The first term is the rate of work done by pressure of surrounding. The second term represents the rate of work done by viscous forces. Notice that using the divergence theorem, the contribution of these two terms for any control volume can be converted to a surface integral evaluated on the boundaries. The third term is viscous dissipation and represents the rate of irreversible conversion of kinetic energy to internal energy. This term always acts as a sink. The fourth term shows the rate of work done by gravity force. The last term represents the contribution of EHD work on the kinetic energy. This term can be interpreted as the useful part of EHD work on the fluid resulting in fluid movement.

Therefore, if the total EHD input power to a control volume is $P = I \cdot \mathbf{f}$, the efficiency of EHD can be defined as

$$\mathbf{h} = \frac{\int_{V_c} \mathbf{u} \cdot \mathbf{F}_e}{P} \quad (2-37)$$

2.6 Definitions and Physical Concepts

In the previous section the electrohydrodynamics phenomenon from a mathematical perspective was studied, and the governing equations were introduced. The following section will describe some of the key physical concepts and definitions that play important roles in the phenomenology of the electrohydrodynamics process.

2.6.1 Polar and Non-polar Liquids

A number of length scales appear in the microscopic study of ions inside the liquids, among which are the size of ions, a , and *Bjerrum distance*, l_B , defined as the distance at which the Coulombian interaction of electrostatic energy between two ions of opposite polarity equals their thermal energies. This length scale is given as

$$l_B = \frac{e^2}{4\pi\epsilon K_B T} \quad (2-38)$$

Now, if for a liquid $l_b \gg a$ the majority of ions are associated in ionic pairs, the liquid is called a *non-polar liquid*, while if $l_b \ll a$ ions stand free, the liquid is called a *polar liquid* (Castellanos 1998).

Polar liquids have permanent dipoles. In such dielectrics, the asymmetry in their molecular structure leads to a permanent displacement of positive and negative charge centers even in the absence of an external field. Polar liquids are presented as aromatic hydrocarbons (nitrobenzene, chlorobenzene, etc.), spirits, acetone, liquid crystals, water, and ethanol. Polar liquids dissolve and dissociate impurities so efficiently that it is extremely difficult to purify them to a state where they exhibit high level of electrical

resistivity (i.e. $> 10^{12}$ ohm-m). Highly-pure polar liquids are very attractive as dielectric media by virtue of their intrinsically large permittivities. ($\epsilon_r > 30$) (Gallagher 1975). For a review of purification techniques see Schmidt (Schmidt 1997).

Non-polar liquids do not form dipoles appreciably in the absence of an external electric field. The dipoles formed in such dielectrics, on the application of electric field, are not permanent, and their atoms return back to their original state once the electric field is removed. Most of the insulating liquids used in power system applications are non-polar.

2.6.2 Ion Mobility

Charge carriers are typically electrons and ions. In most situations the electrons are quickly trapped by electronegative impurities or molecules of the fluid. For these situations the positive and negative ions are the only charge carriers present in the fluid. The mobility of the charge carrier, μ_e , is defined as its velocity per unit of electric field stress.

Various techniques for measuring the charge carrier mobility have been developed. Many methods employ pulsed sources of charge carriers, such as radioactive isotopes, lasers, or accelerators. In other methods, a continuous charge carrier injection is modulated by an electric field. Sometimes electric field impulses are applied. The most important method for measuring electron or ion mobilities is the time-of-flight method, which consists of the measurement of the time it takes a group of charge carriers to traverse a certain distance in an electric field.

For the theoretical description of ion mobility in fluids a continuum model has been developed known as Walden's rule. In this model, the ionic motion is considered as

that of a charged sphere of radius R carrying an elementary charge through a viscous medium of viscosity μ . If it is assumed that the driving electric force applied to the charge carrier is equal to the viscous Stokes force exerted on a spherical ion of radius R , then we conclude

$$\mu_e = \frac{e_0}{6\pi R\mu} \quad (2-39)$$

where μ_e is the ionic mobility. Notice that for negative ions, μ_e is negative. Taking $R \approx 10^{-9}$ m, then $\mu_e \mu \approx 10^{-11}$ C/m, which implies that the product of mobility and viscosity is a constant.

A large discrepancy in ion mobility measurements has been reported by many researchers, and some of the results do not support Walden's rule (Eq.(2-39)). It has been shown that impurities play a significant role in the inconsistency of experimental results. Nevertheless, it is believed that Walden's rule is correct in its order of magnitude.

2.6.3 Charged Carrier Generation in Gases

2.6.3.1 Various processes of Charged Carrier Generation

There are several processes by which a charge carrier (i.e. an electron, a positive ion, or a negative ion) can be produced in a fluid. Malik et al. (Malik, Al-Arainy et al. 1998) have summarized the main ones in a gas discharge, which are shown in Figure 2-1.

Among these processes, the cathode processes are of the most interest. At their normal state, the electrons are bound to the solid electrode by electrostatic forces between electrons and ions in the lattice. For the electron to leave the cathode, a minimum specified energy, known as work function, is required where its value depends on the

material. Each of the cathode processes provides a different source of the required energy. Let's briefly review some of these processes.

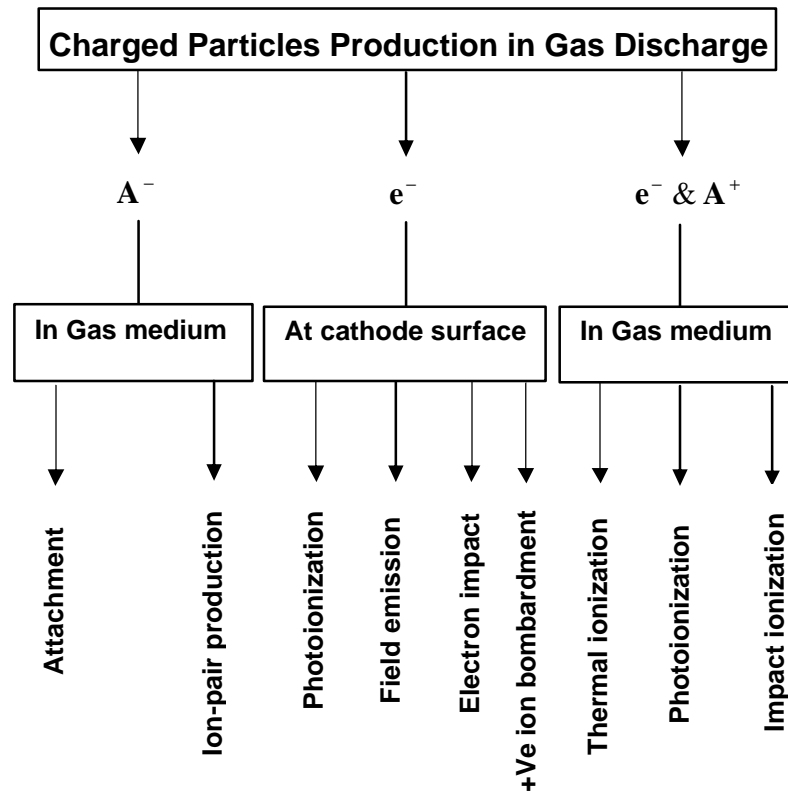


Figure 2-1 The main processes responsible for the production of the charged particles in a gas discharge (Malik, Al-Arainy et al. 1998)

Positive Ion and Excited Atom Bombardment

When a positive ion has an impact on the cathode, an electron is released, provided the impact energy is equal to or more than twice the cathode work function. At least two electrons will be released: one will neutralize the positive ion and the other will be ejected to the gas medium. An electron might also be emitted as a result of the bombardment of the cathode by neutral excited atoms or molecules.

Photoemission

If the energy of a photon striking the cathode surface is higher than the cathode work function, an electron may be ejected from the cathode.

Thermionic Emission

Raising the cathode temperature to a very high value (around 2000 K) will lead to some electrons leaving their surfaces, since the violent thermal lattice vibrations will provide the electrons with the required energy. When a positive ion has an impact on the cathode, an electron is released. This process is also called Schottky emission. In the vacuum, the emitted current density is given as

$$J = J_0 \exp\left(\frac{B\sqrt{E}}{T}\right) \quad (2-40)$$

where J_0 is the current density as the electric field approaches zero and the constant B takes the value $0.441 \text{ K(m/V)}^{1/2}$ (Castellanos 1998).

Field Emission

A high electrostatic field may overcome the binding force between electrons and protons and lead to the liberation of one or more electrons from the cathode. This takes place when the electric field value is of the order 10^4 - 10^5 kV/cm. Although this is a relatively high electric field intensity, conditions for field emission can exist at electrode protrusions and microdefects. The emitted current density is given by

$$J = \frac{1.54 \times 10^{-6}}{W} E^2 \exp\left(-\frac{6.83W^{\frac{3}{2}}}{E}\right) \quad (2-41)$$

where W is a parameter defined as the height of the potential barrier above the Fermi level of the metal, measured in electron-volts (Castellanos 1998). Usually, if $\log(I/f^2)$ is

plotted as a function of $1/f$, it yields a straight line, indicating that W is slowly varying with E .

Of these mechanisms, thermionic emission occurs at very high temperatures and is important in vacuum conditions. Field emission occurs at very high values of surface electric field and is important mainly in vacuum breakdown phenomena. Therefore, both these mechanisms generally do not play any important role in gas discharges and charge creation at normal atmospheric temperature and pressure. However, positive ion and excited atom bombardment as well as photoemission can be the major processes of the charge creation inside gases.

2.6.3.2 Corona Discharge and Non-uniform Field Gas Breakdown

Any gas can withstand a certain amount of electrical stress, but when the electric field intensity exceeds this value, a discharge is inevitable. In the case of a uniform electric field inside a gap, the discharge usually takes place in the form of a complete breakdown. However, in a non-uniform field gap, the discharge will occur only in areas where the electric field intensity is higher than the dielectric strength of the gas. This process is known as partial discharge, and when it takes place in gases it is called *corona discharge*.

Corona discharge is in conjunction with the charge carrier generation that leads to an electrical current flow. The required non-uniform electric field can be established if one of the electrodes has a much smaller radius of curvature than the other. In this case the sharper and flatter electrodes are called *emitters* and *collectors*, respectively. Depending on the polarity of the applied voltage to the emitter electrode, two modes of

the corona discharge can be identified, which are negative and positive coronas (Malik, Al-Arainy et al. 1998; Maruvada 2000)

Negative Corona

For this mode, the cathode is the emitter electrode. As the voltage is raised to the critical field intensity, electron avalanches are formed and propagate towards the anode, leaving behind positive ions. When the electrons enter the low field region, they slow down and form negative ions. Thus, a space charge field is formed as shown in Figure 2-2. Here E_s is the applied electric field, and E_0 is the electric field due to the generated space charge acting in reverse direction. The discharge and ion generation stops when the effective electric field intensity ($E_s - E_0$) in the vicinity of the emitter electrode drops below a critical field value. The space charge electric field vanishes when the charge carriers clear the gap, and as a result, the electric field in the neighborhood of the emitter recovers. Thus, once again corona discharge is repeated. This leads to the formation of corona current pulses. Upon increasing the voltage further, at a certain voltage the space charge field becomes incapable of reducing the effective electric field at the emitter electrode neighborhood below its critical value. Therefore, the discharge process becomes continuous, causing a pulseless current. This mode is known as glow corona. Upon increasing the voltage even further, the discharge occupies a major portion of the inter-electrode spacing, and incomplete streamers are formed. This mode is known as pre-breakdown streamer corona. Further increase of voltage leads to a complete breakdown.

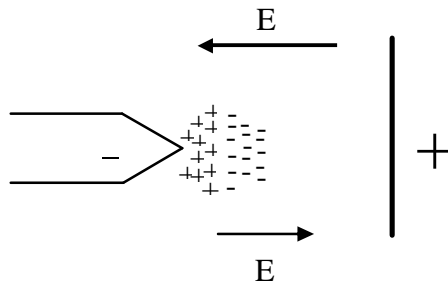


Figure 2-2 Negative corona avalanche

Positive Corona

In this case the anode is the emitter electrode. As the voltage is increased until the critical field is established at the anode, electrons are accelerated from the low field region towards the anode and cause ionization in the high field region (Figure 2-3). At the anode, the electrons will be absorbed quickly while the positive ions accumulate around the anode. As a result, the highest ionization activity occurs at the anode. Due to the lower mobility of the ions, a positive ion space charge is left behind along the path of the development of the avalanche of ions. As a result of the high electric field intensity near the anode, electron attachment in positive corona is less effective than in negative corona, and the majority of the free electrons created are absorbed in the anode. The discharge stops when the effective field near the anode drops below the critical electric field. However, the discharge restarts when the positive ions are cleared away from the anode towards the cathode, and the field in the vicinity of anode recovers to a higher value. As the voltage is increased further, the field at the anode will be high enough to cause discharge even when there is a positive space charge near the anode. In this case a continuous current will flow from glow corona. Upon raising the voltage further,

incomplete streamers are formed, resulting in a pre-breakdown-streamer mode of corona. As the voltage is further increased, complete breakdown occurs in the gap.

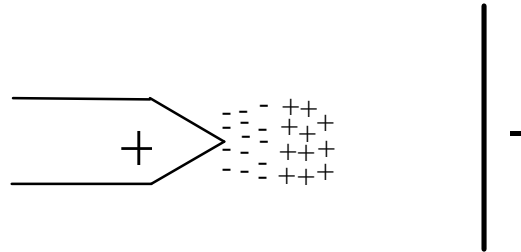


Figure 2-3 Positive corona avalanche

Corona Onset Gradient and Kaptsov Theory

Corona onset field is the critical electric field intensity value needed at the emitter electrode to initiate a self-sustaining discharge. The corona onset field is a function of the radius of curvature of the emitter conductor and its surface condition as well as of the gas temperature and pressure. The corona onset electric field intensity of cylindrical conductors inside the air has been studied experimentally, and empirical formulas have been developed for AC and DC voltages. In general, the corona onset gradient E_c of a cylindrical conductor is given as

$$E_c = mE_0\delta \left(1 + \frac{K}{\sqrt{\delta r_c}} \right) \quad (2-42)$$

where E_0 and K are empirical constants depending on the nature of the applied voltage (Maruvada 2000). These values for AC voltages, according to Peek, are $E_0=29.8$ kV/cm (or 21.1 kVrms/cm) and $K=0.301$ for the case of two parallel conductors above ground and $E_0=31.0$ kV/cm (or 21.9 kVrms/cm) and $K=0.308$ for the concentric cylindrical

geometry (Peek 1929). The corresponding values for DC voltages, according to Whitehead, are $E_0 = 33.7$ kV/cm and $K = 0.24$ for positive polarity and $E_0 = 31.0$ kV/cm and $K = 0.308$ for negative polarity (Whitehead 1929). The fact that the constants in Whitehead's formula for negative polarity DC are the same as those for Peek's for AC suggests that AC corona onset occurred during the negative half-cycle of AC. δ is the relative air density factor, and is given as

$$\delta = \frac{273 + t_0}{273 + t} \cdot \frac{p}{p_0} \quad (2-43)$$

where t is the temperature and p the pressure of ambient air and t_0 and p_0 are reference values. Usually, $t_0 = 25$ °C and $p_0 = 760$ torr. r_c is the conductor radius in cm and m is the conductor surface irregularity factor. Conductor surface irregularity factor m is equal to 1 for smooth and clean conductors. Experimental results have shown that the value of m may vary between 0.75 and 0.85 for stranded conductors, depending on the ratio of the strand-to-conductor diameter.

For the unipolar corona discharge process, according to Kaptsov's theorem, the electric field intensity of the corona discharge at the vicinity of the emitter electrode remains at its onset value despite the variation in the applied voltage. If the emitter electrode is a thin conductor, the onset electric field intensity at the emitter surface is reasonably described by Peek's formula (i.e. Eq. (2-42)).

2.6.4 Charged Carrier Generation in Liquids

Many of the processes that can lead to charged carrier generation in gases can cause charge generation inside liquids as well. Moreover, in liquids another charge generation process known as field ionization might generate ions.

Field Ionization

When the emitter electrode (i.e., an electrode with a small radius of curvature) is of the positive polarity, molecules adjacent to the electrode become ionized due to electrons tunneling into the metal. While field emission is governed mainly by the work function, field ionization is controlled by the difference between the energy of the forbidden zone (also known as ionization energy) and the work function (Schmidt 1997).

Ion Injection in Nonpolar Liquids

In liquids the field emission occurs at intense values of the electric field. At such high values the electrical double layer is destroyed, and tunneling of electrons from the metal to the molecule (field emission) or from the molecule to the metal (field ionization) takes place. However, in most situations of practical interest in EHD, the electric fields are not intense enough, and the electrical double layer mediates the electronic transfer at the interface. In nonpolar liquids ion injection may be described by a two-step process: first the ions are created at the electrode, and then they escape out of the image force region. It can be shown that in this situation the injected charge density in the liquid at the electrode is

$$\mathbf{r}_{e,inj} = \frac{\mathbf{r}_{e,inj}^0}{b K_1(b)} \quad (2-44)$$

where $\mathbf{r}_{e,inj}^0$ is a constant that depends on the liquid and electrolyte nature (Castellanos 1998). b is a dimensionless parameter defined in Eq. (2-17) and K_1 is the modified Bessel function of the second kind and first order. This expression has been successfully verified in a large variety of organic solvents and salts up to 2×10^2 kV/cm. Finally, it is to be

noticed that for values of $1 \leq E \leq 40$ kV/cm we may safely assume that the charge density is constant. This is called an *autonomous* injection.

2.6.5 Current Density-Electric Field Characteristic

Generally, gases and most nonpolar liquids exhibit a dependence of the current density, j , on the electric field strength, E , as shown in Figure 2-4, where four distinct regions are observed (Schmidt 1997).

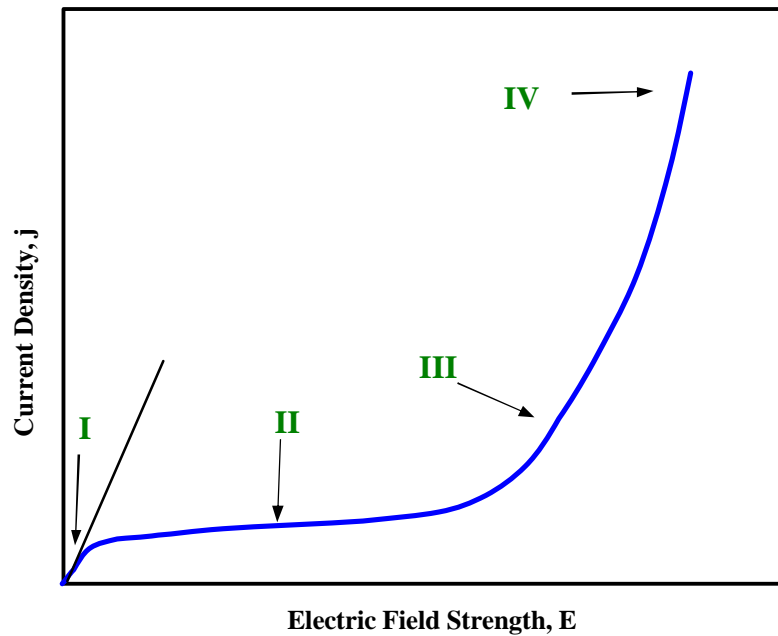


Figure 2-4 J-E- characteristic of gases or nonpolar liquids

At low values of electric field intensity (i.e. $E < 1$ kV/cm), Ohm's law,

$$j = \mathbf{s}_e E$$

(2-45)

is fulfilled (Region I). This region is followed by a plateau (Region II) where the current tends towards saturation. All charge carriers generated per second are extracted from the volume. At higher electric field intensities (i.e. 10 kV/cm $< E$), a steep increase of j with E

is observed (Region III), which eventually at high electric field (i.e. $E \sim 40\text{-}100\text{ kV/cm}$) leads to breakdown (Region IV).

In liquids, unlike in gases where natural radiation plays important role, the major role is played by the dissociation of ionic impurities and solid impurity particles, which are dominant factors in Regions I and II. The host liquid may dissociate the impurities into ion pairs. These positive and negative ions, which escape recombination, drift to the electrodes and thus give rise to a flow of current in the ohmic region. At the intermediate field, the charge carriers are produced entirely by an electro-chemical process at the interface between the liquids and metal, and a so-called double layer is formed at the electrode. Its significance is that the positive and negative ions are created at this junction. At certain field strength the ions will move to the electrodes at a rate faster than the generation rate in the bulk of the liquid, which causes growth of a space charge at the electrodes, causing the current to tend toward saturation (Region II). If the field applied to the liquids is sufficiently high, the current tends to increase sharply for comparatively small increments of field. A number of factors might play a role in this process.

When the concentration of undissociated impurity molecules is sufficiently high, the increase in electric field will lead to an enhancement of the dissociation process. As a result, more, free ion pairs are produced and conductivity increases.

Reduction or oxidation of impure molecules at the liquid/metal interface may yield excess negative or positive ions. Such electrochemical reactions are controlled by the double layer potential, which in turn is determined by the density and the nature of absorbed ions.

Solid impure particles are also considered to contribute extensively to high field conduction. Since these particles may also be of a semiconducting or insulating nature, prolonged action of electric stress at the electrodes will either lead to their removal from the interelectrode gap or to their neutralization at the electrodes, thus reducing the conduction current.

A high field can lead to the emission of electrons at the cathode, whereas at the anode, field ionization can be initiated. As pointed out in previous sections, the field strength required for these processes to begin is of the order of 10^4 kV/cm.

Under high fields, conduction currents are usually accompanied by randomly occurring pulses or bursts of currents. It has been demonstrated that these pulses are associated with bubble generation (Qureshi and Chadband 1988) and the development and propagation of discharge called tress (Lesaint and Tobazeon 1988).

2.6.6 Charge Decay

Consider a charged specie (e.g., a positive or negative ion) moving inside a medium. It can be shown that the charge of the specie is not preserved permanently, and charge decay will be observed. The rate of the charge decay is an important factor in analysis of EHD phenomena. For example, the Coulomb force in liquids is directly proportional to the charge of ionic species. If the charge of these species decays quickly, the Coulomb force also decreases rapidly. To study the rate of charge decay, two cases will be considered (Castellanos 1998).

2.6.6.1 Ohmic Regime

For ohmic regime the current density is given as

$$\mathbf{J} = \mathbf{s}_e \mathbf{E} + \mathbf{r}_e \mathbf{u}$$

(2-46)

Using Eqs. (2-28)-(2-31), it can be shown that if the electrical conductivity σ_e remains constant, the charge conservation equation becomes

$$\left(\frac{\partial \mathbf{r}_e^*}{\partial t^*} + \mathbf{u}^* \cdot \nabla \mathbf{r}_e^* \right) + \frac{1}{\mathbf{e}_s \text{Re}_e} \mathbf{r}_e^* = 0$$

(2-47)

or

$$\frac{D^* \mathbf{r}_e^*}{D^* t^*} + \frac{1}{\mathbf{e}_s \text{Re}_e} \mathbf{r}_e^* = 0$$

(2-48)

Therefore, for each charge carrier moving with the fluid, the transient charge variation can be found by solving Eq.(2-48) as follows:

$$\mathbf{r}_e^* = \mathbf{r}_e^*(0) e^{\frac{-t^*}{\mathbf{e}_s \text{Re}_e}}$$

(2-49)

The electrical Reynolds number is correlated to the charge relaxation time by

$$\mathbf{e}_s \text{Re}_e = \frac{t}{t_r}$$

(2-50)

where the definitions of the dimensionless parameters are given in Table 2-2. Therefore, it can be concluded that the charge decay depends on the electrical Reynolds number of the process. In other words, if the charge carriers move inside a fluid with high electrical conductivity and low electrical permittivity, the charge decay process will be faster.

2.6.6.2 Unipolar Charge Injection Regime

In the absence of the charge diffusion and for a perfect insulation fluid (i.e. $\sigma_e = 0$), the total current density is given as

$$\mathbf{J} = \mathbf{r}_e m_e \mathbf{E} + \mathbf{r}_e \mathbf{u}$$

(2-51)

In this case, the charge conservation law can be written as

$$\left(\frac{\partial \mathbf{r}_e^*}{\partial t^*} + \mathbf{u}^* \cdot \nabla^* \mathbf{r}_e^* \right) + \frac{F_e}{\text{ReSc}_i} \mathbf{E}^* \nabla^* \mathbf{r}_e^* + \frac{F_e E_{\text{hd}}}{e_s \text{ReSc}_i \text{Md}} \mathbf{r}_e^{*2} = 0$$

(2-52)

or in terms of dimensionless characteristics time:

$$\left(\frac{\partial \mathbf{r}_e^*}{\partial t^*} + \mathbf{u}^* \cdot \nabla^* \mathbf{r}_e^* \right) + \frac{\mathbf{t}'_T}{\mathbf{t}} \mathbf{E}^* \nabla^* \mathbf{r}_e^* + \frac{\mathbf{t}_E}{\mathbf{t}} \mathbf{r}_e^{*2} = 0$$

(2-53)

The dimensionless charge conservation equation's exact solution is as follows:

$$\mathbf{r}_e^* = \frac{\mathbf{r}_e^*(0)}{\left(1 + \frac{\mathbf{t}_E}{\mathbf{t}} t^*\right)}$$

(2-54)

This solution is valid on the characteristic lines $d\mathbf{r}_e^*/dt^* = F_e/(\text{ReSc}_i) \mathbf{E}^* + \mathbf{u}^*$, so that unless a given element of liquid can be traced via a particle line to a source of charge, it will support no bulk charge density. The algebraic charge relaxation time τ_E depends on the initial level of charge and after several decay times; the dimensionless charge density reaches a limiting value $\mathbf{r}_e^*(0) \frac{\mathbf{t}}{\mathbf{t}_E t^*}$; and the dimensional charge density approaches a limiting value $\mathbf{e}/m_e t$, which is independent of the initial condition. The ratio between the space charge decay time and the ionic transient time is given by the nondimensional number $C = \mathbf{t}_E/\mathbf{t}'_T = \mathbf{r}_{e,0} L/\mathbf{e}E$. Small values of C indicate that the electric field is determined by the external power supply connected to the electrodes in the fluid. In contrast, for high values of C the electric field is strongly dependent on the charges that are either inside or on the surface of the fluid.

2.7 Summary

In this chapter the fundamentals of the EHD concepts and the governing equations were reviewed and using a set of nondimensional parameters, the governing equations were converted to dimensionless form. Terminology, as well as definitions of some basic terms and physical concepts, was also introduced and studied. In the next chapter the relevant research works reported in literature will be reviewed.

CHAPTER 3: LITERATURE REVIEW

3.1 Introduction

For many years electrohydrodynamics have been the subject of numerous investigations. In recent years, research interest has been particularly boosted with the emergence of miniature systems. Moreover, the study of EHD is interdisciplinary, making attractive for various scientific communities. Although applicability of EHD has been successfully demonstrated for many years, the understanding of its processes, its characterization, and its applications in system miniaturization have not been fully addressed and are still the subjects of ongoing research.

The objective of this chapter is to review some of the earlier works on micropumps as well as related basic research on the EHD phenomena and its applications as related to the present work. These studies are divided into EHD pumping mechanisms, non-EHD meso and micro pumping mechanisms, and numerical modeling of the EHD phenomenon.

3.2 A Review of Various EHD Pumping Mechanisms

EHD pumping is nonmechanical; it has neither moving mechanical parts nor the need for an external pressure gradient for operation. This is why EHD pumping continues to be attractive for many engineering applications with substantial commercialization potential in a number of industrial sectors..

Since the current research deals with the EHD pumping process, a review of the studies in this field will be helpful. EHD pumping mechanisms can be divided into several categories. This is because the EHD force consists of different terms that each can result in a driving force and pumping action (see section 2.3.3 and Eq. (2 24)). Furthermore, there are various physical processes that are due to a specific EHD body force term. For example, an electrophoretic (Coulombian) force can be the driving source for different pumping techniques such as ion-injection or electrokinetic. A review of various techniques is presented in the following sections.

3.2.1 Ion-Injection Pumping Mechanism

Since the current research involves the design and testing of a meso-scale ion-injection pump, a review of earlier investigations on this subject was necessary. As with some other types of EHD pumps, the ion-injection pumps driving action relies on the Coulomb force applied on the free charges. However, in this particular mechanism, the source of these free charges is the direct injection of ions from the electrode(s) by applying a high intensity electric field. Once a strong electric field is established between two electrodes inside an electrically insulating fluid, ions are injected through one or both electrodes (unipolar or bipolar charge injection). The ion-injecting electrode is called the emitter, while the other electrode is called the collector. Notice that in some cases, one electrode can simultaneously act as both the emitter for a certain ion polarity and the collector for another ion polarity. The free charges injected into the fluid move along the electric field lines, dragging adjacent fluid molecules and starting them in a bulk motion. This type of pump is sometimes called an ion-drag pump due to the dragging action of

the ions. However, this might be a misleading term since the dragging action of the ions might be found in other types of pumps as well.

The fact that liquid dielectrics can be pumped by injection of charges has been known for almost a century (Chattock, Walker et al. 1901). However, a feasibility study of ion-injection pumping was not realized until 40 years ago.

Stuetzer (1959) studied ion-injection pressure generation experimentally and theoretically. He presented an approximate theory that was applicable for unipolar conduction both in gases and in insulating liquids. The experimental result was in agreement with theory but was limited to the static case (i.e., nonmoving fluid). Later, Stuetzer (1960) extended his investigation and presented a theoretical model with supporting measurements that described the dynamic behavior of an ion-injection pump assuming unipolar ion conduction. Pickard (Pickard 1963 (A) ; Pickard 1963 (B)) reexamined the ion-injection pump theoretically and experimentally. He obtained new theoretical results for both static and dynamic cases.

Melcher (1981) considered a one-dimensional DC pump consisting of a pair of electrically conducting grids through which the fluid passes and which meanwhile acts as an emitter and collector of the charged carriers. He derived an expression for pressure rise as a function of a dimensionless parameter called electric Reynolds number and the dimensionless current. He also found the efficiency of the electrical-to-mechanical energy conversion as function of these two variables. Based on his model, at low electric Reynolds numbers, the efficiency increases rapidly, but at high electric Reynolds numbers the rate of increase decelerates. Most of the assumptions made by Stuetzer and

Pickard were included in Melcher's analysis. However, Melcher's analyses were more general, since his results were presented in dimensionless form.

Crowley *et al.* proposed a simplified model of EHD pumping to account for the material properties of the working fluid (Crowley, Wright et al. 1990). They examined the effect of the working fluid on the flow rate and the efficiency of the pumping. Their analysis was not limited to ion-injection pumping. However, in their model the complicated effects of the channel geometry, electrode structure, charge injection and flow stability were neglected, and instead an order magnitude analysis was employed. In their theoretical analysis, they considered the contribution of all three components (conduction, convection, and mobility) to the current density. Based on their fundamental model, they concluded that a high dielectric constant and low viscosity produce high-flow velocities, while low conductivity and mobility promote high efficiency. If we use the same model for HFE-7100[®], the working liquid in the current research, a relatively high velocity is expected, since this dielectric liquid has a high dielectric constant ($\epsilon_s \approx 7$) and low viscosity. However, since the ion mobility and electrical conductivity of this liquid is relatively high, a moderate efficiency should be expected. Notice that according to Eq. (2 39), the ion mobility and viscosity are inversely proportional.

Bryan and Seyed-Yagoobi (1992) conducted an experimental investigation on an ion-injection pump. They constructed two pumping sections with 1 and 10 electrode pairs. In their design the distance between the emitter and collector electrodes was 0.5 cm, while the spacing between each electrode was 1.0 cm. The total length of the pumping section for one electrode pair and 10 electrode pairs was 2.4 cm and 33.0 cm, respectively. Pumping flow rate as high as 1.1 kg/s and total pressure of 111.9 Pa at 25

kV for a transformer oil working fluid was achieved. The maximum current at 25 kV for a pair of electrodes was as high as 14 μA and for 10 electrode pairs as high as 140 μA . The maximum efficiency reported was 6%. They also investigated the effect of doping the transformer oil on the mass flow rate. Over the entire voltage range (15 kV-25 kV) the velocity of the undoped transformer oil was greater by a factor of three over transformer oil doped at 100 ppm. No significant difference in the bulk velocity was observed between the doping level of 100 and 250 ppm.

Bryan and Seyed-Yagoobi (1994) also presented a model to analyze the one-dimensional flow field generated by a single electrode pair ion-drag pump. Their model was an extension to Melcher's model since the effect of the electrical conductivity was also taken into account. Their results were presented in terms of three dimensionless parameters, $\text{Re} = \epsilon U_0 / \sigma_e L$, $\text{Esl} = \mu_e \phi_0 / U_0 L$, and $\text{Es} = \mathbf{r}_{e,0} L^2 / \epsilon \mathbf{f}_0$. The results showed that the nonuniformity of charge density distribution between electrodes depends on the Esl number. Lower values of Esl resulted in a more uniform distribution and a higher value of charge density. Therefore, the charge density distribution is more likely to be uniform in a more viscous fluid, since the mobility is inversely proportional to the fluid viscosity. Furthermore, a higher Re number resulted in a more uniform charge density distribution. One way of achieving a high value of Re is to have a longer charge relaxation time, ϵ / σ_e , to allow the majority of the charges to reach the collector electrode. Bryan and Seyed-Yagoobi's results on the pump efficiency were also in agreement with Crowley *et al.*'s conclusion that low conductivity and mobility promote the efficiency (Crowley, Wright et al. 1990).

Barbini and Colleti (1995) conducted an experimental study on the influence of the interelectrode gap on the static pressure head. Their ion-injection pump consisted of two plane and parallel electrodes placed inside a cylindrical PMMA housing (inner diameter 30 mm). Two different electrode geometries, used as the collector electrodes, were a circular stainless steel grid made of 170 μm wire and a drilled (holes diameter 2 mm) brass disk 3 mm thick. The emitter electrode geometry was a circular drilled disk 3 mm thick. Both potential polarities were applied to the emitter electrode. The inter-electrode distance, d , could be varied within a 1 to 5 mm range. Three different oils were used in the tests: castor oil ($\epsilon_s = 4.2$, $\rho = 0.956 \text{ gr/cm}^3$, $\nu = 1.041 \text{ Pa.s}$), silicon oil ($\epsilon_s = 2.25$, $\rho = 0.962 \text{ gr/cm}^3$, $\nu = 0.048 \text{ Pa.s}$), and dodecylbenzene ($\epsilon_s = 2.21$, $\rho = 0.855 \text{ gr/cm}^3$, $\nu = 0.006 \text{ Pa.s}$). Based on their experimental results, they noticed that a long exposure of the liquids to the ambient atmosphere before testing often caused a significant reduction (up to %80) in the obtainable pressure and in the breakdown voltage, probably due to the increase in impurity or humidity content. Moreover, they observed that the static pressure curves varied almost linearly with $(1/d)^2$ for a negative polarity of applied potential, while such a relationship did not hold for the results obtained with positive polarity potential. They also investigated the relationship between the pressure head and ϕ^2 or $(\phi - \phi_0)^2$ where ϕ and ϕ_0 are the applied potential between electrodes and the threshold potential, respectively. They found that, while for silicon oil the pressure head varied linearly with $(\phi - \phi_0)^2$ (in agreement with Stuetzer's model), the pressure head for castor oil showed an approximately linear relationship with ϕ^2 (in agreement with Pickard's model). However, for dodecylbenzene no explicit correlation between the pressure head and ϕ^2 or $(\phi - \phi_0)^2$ was found. The highest pressure head

recorded during this investigation was 765 Pa for silicon oil just prior to breakdown using an inter-electrode gap of 3.5 mm at an applied voltage of 37 kV, although the relative permittivity of silicon oil was lower than castor oil. For silicon oil at low positive polarity voltages, a reverse pumping phenomenon was also observed.

Wong *et al.* developed an EHD injection pump (Wong, Adkins et al. 1996). Fabrication of the pump was accomplished using laser micromachining technology. Two designs were taken into consideration. In the first design, two silicon substrates were stacked vertically on top of each other. Gold was deposited on one side of each substrate serving as the electrode for the EHD pump. A laser was used to drill an array of circular holes in the deep region of both silicon substrates, leaving an open pathway for fluid movement. In the second design, the silicon substrates formed in the grid structure oriented “back-to-back” and bonded together. The back-to-back design had a shorter grid distance between the anode and cathode electrodes, and thus a smaller voltage was required for pumping. Their results showed that this EHD micropump design can achieve a pressure head of 287 Pa with applied voltage 120 V for propanol as the working fluid. No direct measurement of the flow rate was reported, but based on analytical calculation, a volumetric flow rate of about 2.5 ml/min across a square microchannel of 1 cm long with a $100\ \mu\text{m} \times 100\ \mu\text{m}$ cross-sectional area was estimated. However, the applied power to the pump was as high as 5 W, which is surprisingly high. This may have been due to a high electrical conductivity of propanol ($\sigma_e \cong 1 \times 10^{-6}\ \text{1}/\Omega\text{m}$), despite its high dielectric constant ($\epsilon_s = 22.2$).

Ahn and Kim (1997) designed, built, and tested a micro ion-injection pump with planar electrodes fabricated on a glass substrate. The pump consisted of an array of 30

planar electrode pairs driven by a DC voltage. The spacing between each electrode pair was 100 μm , while the distance between two successive stages was 200 μm . Ethyl alcohol was pumped in both directions, and the flow rate and the static pressure were measured in channels of depth 100 μm or 200 μm and width fixed at 3 mm. The maximum static pressure head at 110 V for 100 μm and 200 μm channel heights were about 220 Pa and 100 Pa, respectively. In order to measure the flow rate, a CCD camera and microscope were used, and the maximum measured flow rates for 100 μm and 200 μm channel heights were about 15 $\mu\text{l}/\text{min}$ and 50 $\mu\text{l}/\text{min}$, respectively, which were relatively low. The measured current was in the order of 1 mA. Therefore, the input power of the pump should have been about 0.1 W, which is considerable. This might have been due to a high electrical conductivity of the working fluid, ethyl alcohol. They also reported some shorted circuit cases over 100 V DC due to an electrochemical reaction under high DC voltage.

Asano and Yatsuzuka (1999) conducted an experimental parametric study on an ion-injection pump with needle-cylinder electrodes. The emitter of the pump consisted of a number of needles, while a meshed electrode or perforated cylinder was used as the collector. In order to increase the pressure head, the number of the needles of the emitter was changed from one to fourteen. The perforated cylindrical shape collector was designed in such a way that the center of a hole was aligned with a needle electrode and the length of the collector was fixed at 40 mm. The emitter and collector electrodes were placed inside a horizontal tube with an inner diameter of 26 mm, and silicone oil was used as the working fluid. When the gap distance between the tip of needles and the collector was varied, the gap of 5 mm showed better results. Therefore, many

experiments were performed with this gap space. The results indicated that the 9-needle design showed the best results in terms of the generated pressure head compared to other designs for the same applied voltage. However, the breakdown voltage for this design was lower than the 7- or 14-needle designs. The maximum pressure head obtained was about 80 mm (about 770 Pa) at a voltage of 40 kV DC. They also investigated the effect of the diameter of the collector holes. The results showed that in terms of pressure head, the 6mm-hole electrode was better than the 3 mm-hole or mesh electrodes. Furthermore, their investigation on the needle radius of 35 μm and 10 μm revealed that the variation of pressure with the voltage fairly remained similar for both cases; however, the breakdown voltage seemed to be affected. The smaller the radius, the better performance obtained. No result about the electrical current was reported in this work.

Bologa *et al.* performed experimental tests to investigate the performance of a multistage ion-injection pump with latticed electrodes (Bologa, Kozhevnikov *et al.* 2000). A latticed electrode was formed from parallel wires imbedded with the defined step in a metal ring. Transformer oil ($\sigma_e \cong 1 \times 10^{-11} \text{ 1}/\Omega\text{m}$) was pumped in a Plexiglas closed loop. The pump pressure head was registered by a differential manometer, and the flow rate was measured with the help of air bubbles that were introduced into the loop. Two electrode arrangements were considered. In the first design, 27 pairs of electrodes with an inter-electrode gap of 3 mm were tested, while in the second design 30 pairs with an inter-electrode gap of 4 mm were built. The experimental results showed that the maximum static pressure head for the first and second designs at 20 kV was about 10 kPa and 7 kPa, respectively. Besides, at inter-electrode gaps of 3 mm and 4 mm, the breakdown field intensity was about 70 and 67.5 kV/cm. Some increase of the EHD

pumping pressure after breakdown was also observed, which could be due to the presence of breakdown products. Moreover, the formation of a thin coating on the electrodes was found, even though the electrical field intensity did not exceed the breakdown value. The maximum volumetric flow rate and pressure head for a dynamic test for the first and the second electrode designs (i.e. 3 mm gap \times 27 and 4 mm gap \times 30) were 160 ml/min, 7.5 kPa, 660 ml/min, and 7.5 kPa, respectively. The pump efficiency result showed an increasing trend with the voltage rise. The maximum efficiency for the first electrode design was about 6% for a voltage of 18 kV, while for the second electrode design it was about 1% for a voltage of 26 kV. Bologna *et al.* also reported a linear pressure-flow rate characteristic trend for the EHD pump at a constant voltage of 20 kV.

Yanada *et al.* investigated experimentally the effect of the number of needles on the emitter, the configuration of the collector, and the type of the working fluid on the performance of an ion-injection pump with a needle-mesh electrode configuration (Yanada, Hakama et al. 2002). The liquids used consisted of silicon oil and five other types of mineral oil. The emitter electrode was produced by soldering steel needles onto a copper mesh. The collectors were produced in a similar manner, and the number and the length of the needles on the mesh were varied to examine their effects. A series of experiments was conducted to measure different parameters. It was shown for the static condition with no pumping flow that the number of needles on the emitter can affect the pump performance when the electrode spacing is small, that the configuration of the collector does not significantly affect the magnitude of the pressure generated, and that the effect of the type of oil tested is not so significant. The very opposite results to the static condition were obtained for the flow characteristic. It was shown that attaching

needles to the collector mesh in a similar manner to the emitter considerably increases the flow rate, that the configuration of the collector has a significant influence on the flow characteristic, and that the type of oil affects the magnitude of the flow rate and pressure-flow rate characteristic to a great degree. The presented results in this investigation showed that the configuration of the collector electrode is very important in enhancing the performance of the ion-injection pump. The maximum static pressure head that was measured in this series of experiment was about 900 Pa for a voltage of 30 kV.

Darabi *et al.* fabricated and tested an EHD ion-injection micropump (Darabi, Rada et al. 2002). In their design, the overall dimensions of the micropump were 19 mm×32mm × 1.05 mm. The micropump was made of three parts consisting of a ceramic substrate, on which an array of EHD electrodes was deposited and patterned, an epoxy gasket as the side wall, and a top cover with inlet and outlet ports. Four different electrode patterns were fabricated. The first electrode layout consisted of 95 stages of planar emitters and collectors. The electrode gap was 50 μm and the distance between stages was 100 μm. The second design was composed of 80 stages and had an electrode gap of 50 μm with a 100-μm distance between stages. In this design, the emitter and collector had saw-tooth and planar geometries, respectively. The electrode pattern for the third design was similar to the second design but with a larger electrode gap of 100 μm and a 200 μm distance between stages. The number of stages in this design was 50. The fourth design had the same geometry of the third design with the inclusion of 3D bump structures along the emitter electrode. Static pressure tests were performed with a 3M thermal fluid (HFE-7100) as the working fluid. A pumping head of up to 700 Pa at an applied voltage of 300 V was obtained. Their results indicated that among the various

designs that were tested, the saw-tooth geometry with 3-D bump structures performed the best. No flow rate measurement was reported in this work.

Benetis *et al.* conducted a series of experiments on a micropump (Benetis, Shooshtari et al. 2003). The emitter and collector patterns were saw-tooth and planar, respectively, similar to Darabi and co-workers' design. However, the gap spacing and the distance between the stages were different. In their designs, the electrode gap was fixed at 20 μm and 50 μm , while the distance between electrode stages was 80 μm , 100 μm and 200 μm . Moreover, a different type of top cover was used, and the effect of micropump channel height variation was investigated. The channel heights were 100 μm , 220 μm , 350 μm and 450 μm , and the working liquid was HFE-7100. The result showed that with an increase in channel height the static pressure will decrease. Furthermore, a flow rate up to 7.92 mL/min was achieved at voltage of 500 V.

Table 3-1 Summary of reported experimental works on the ion-injection pumps

Investigator(s)	Pump Size	Electrode Geometry	Gap Size	Number of Stages	Distance between Stages
Stuetzer	Dia: 0.3 to 5 mm	Needle-Ring	0.6-10 mm	Not reported	N/A
Pickard	Dia: 12.5 mm	Parallel rod electrodes	Not reported	1	N/A
Bryan and Seyed-Yagoobi	L: 33.0 cm for 10 electrode pairs	E: Ring with needles C: Rings with and without wire mesh	5 mm	1 and 10	10mm
Barbini and Colleti	Dia: 30 mm	E: Circular drilled disk C: Circular mesh and circular drilled disk	Variable: 1 to 5 mm	1	N/A
Wong <i>et al.</i>	~ 8.64mm × 8.64mm	E: Microfabricated grid C: Microfabricated grid	~ 330 μm, 178μm, and 127μm	1	N/A
Ahn and Kim	Channel height: 100μm & 200μm Channel width: 3mm	Microfabricated planar strips	100 μm	30	200 μm
Asano and Yatsuzuka	Dia: 26 mm	Needles-Cylinder	5 mm	1	N/A
Bloga <i>et al.</i>	—————	Lattices from parallel wires	3 mm & 4 mm	27 & 30	—————
Yanada <i>et al.</i>	Dia: 20 mm	Needle-mesh	2,4, 6 mm	1	—————
Darabi <i>et al.</i>	19 mm × 32 mm × 1.05 mm	Planar, saw-tooth, and saw-tooth with bumps	50 μm, 100μm	95, 80, 50	100μm & 200 μm
Benetis <i>et al.</i>	~ 40mm × 20 mm × 1.0 mm	Planar & saw-tooth	20 μm, 50μm	94, 73, 54	80μm , 100μm, 200μm

Continuation of Table 3-1

Investigator(s)	Working Liquid	Typical Applied Voltage (kV)	Typical Current (mA)	Max Pressure Head (Pa)	Volume Flow Rate (mL/min)
Stuetzer	Kerosene	5-30	0.01-4	~ 7100	—————
Pickard	Acetone	10	20	~1200	6
Bryan and Seyed-Yagoobi	Transformer oil	25	14 & 140	~112	77,000
Barbini and Colleti	Castor oil, Silicon oil, and dodecylbenzene	~37	—————	765	—————
Wong <i>et al.</i>	Propanol	0.120	~17,000	287	2.5 (calculated)
Ahn and Kim	Ethyl alcohol	0.110	1000	220 & 100	15×10^{-3} & 50×10^{-3}
Asano and Yatsuzuka	Silicon oil	+40	—————	80 mm (~770 Pa)	—————
Bloga <i>et al.</i>	Transformer oil	20	—————	10,000 & 7,000	160 & 660
Yanada <i>et al.</i>	Silicon oil & 5 other types of mineral oils	30	1~ 20	900	Variable, ~ 60
Darabi <i>et al.</i>	HFE 7100	~0.700	—————	~700	—————
Benetis <i>et al.</i>	HFE 7100	~0.500	~ 50	~ 700	8

3.2.2 Traveling Wave-Induced Pumping Mechanism

Another kind of EHD driving technique is based on the induction traveling wave. Like the ion-injection mechanism, this technique also relies on the electrophoretic (Coulombic) force on charge carriers.

Fuhr *et al.* studied the traveling wave principles (Fuhr, Schnelle *et al.* 1994). According to them, traveling wave pumping requires a gradient in electrical conductivity and/or permittivity of the fluids. Usually fluids do not exhibit such inhomogeneities. But by stratifying non-mixing liquids, inserting microparticles or imposing a temperature gradient, anisotropies of the passive electrical properties of the fluid can be created and stabilized. Melcher (1981) has demonstrated that waves of electric fields traveling perpendicularly to the liquid interface or a conductivity/permittivity gradient induce charges at the interfaces or in the liquid bulk. At certain propagation velocities of the electric field, these charges are slightly displaced and interact with the traveling field due to charge relaxation processes. As a result, forces acting on the fluid interfaces, on the foreign particle surface or on the volume element, drive the fluid forward or backward.

At high frequency voltages the space charge disappears in the liquid bulk and the behavior of the liquid dielectric in AC electric field is equivalent to the situation where an ideal liquid dielectric is subjected to a stationary electric field. Space charge in the liquid volume can be induced by imposing a temperature gradient or charge injection from electrodes. Both these techniques have been used to pump dielectric liquids using a voltage traveling wave.

The basic features of pumping by a voltage traveling wave are as follows: (i) If the polarity of the charge induced near the exciting electrode is the same (opposite) as

that on the exciting electrode, it results in a repulsive force causing backward (forward) pumping. (ii) If the frequency is too high then a very small charge near the exciting electrode is induced, while if the frequency is too low, a phase lag between the induced charge and traveling electric field does not result in Coulomb pumping force. Thus at very low and very high frequencies, the pumping by a voltage traveling wave is not effective (Castellanos 1998).

Oda *et al.* conducted an experimental study on the induction pumping phenomenon (Oda, Aoyama *et al.* 1996). The electrodes in their setup consisted of three spiral winding wires covered with dielectric insulation. A three-phase, alternating, high voltage with low frequency was directly applied to the three wires. An acrylic U-tube formed the pump enclosure which the electrode wires were twisted around. With the three-phase voltage, an electric field of the traveling wave built up inside the tube in which the working liquid, kerosene, was placed. The experimental results indicated that the pressure head strongly depended on the peak exciting voltage and frequency. The static pressure head increased with the peak voltage increment. However, the optimum frequency value was observed where an increase or decrease of the voltage frequency led to a pressure reduction. For a voltage of 8.75 kV, the optimum exciting frequency was about 25 Hz, which resulted in a 47-mm, static pressure head (equivalent to 335 Pa). Oda *et al.* also developed a simple analytical model that justified their experimental results.

Several other investigations on induction pumping have also been reported. (For example, see Kashani, Kang *et al.* 2000 and Brand and Seyed-Yagoobi 2002).

3.2.3 Electro-osmotic Pumping Mechanism

The electro-osmotic flow (EOF) pump is another type of EHD pump. This technique, some time called the *electrokinetic* mechanism, operates on the electrophoretic (Coulombic) force on the ions. However, the ion generation mechanism is different from other EHD-base techniques such as ion-injection and traveling wave.

Most surfaces establish an electric double layer (EDL) when brought into contact with either a weak or strong electrolyte solution. Due to the electrochemical reactions at the liquid/solid interface, a charged layer is generated. In the case of the solution/glass surface interface a negative surface charge is created. The inside wall of a fused silica tube is covered with acidic silanol groups (Si-OH). Silanol groups carry a negative charge (Si-O⁻) at PH>2. Counter ions from the bulk liquid are attracted to and shield these negative wall charges. Dissolved co-ions are likewise repelled from the wall. The region with the high concentration of ions next to the liquid/solid interface is called the EDL. The EDL consists of two sub-layers. The layer of counter ions formed by immobile ions adjacent to the wall is called the Stern layer. The outer layer and diffuse part of the EDL is formed by mobile ions of the opposite sign to counter balance the charge of the Stern layer. This layer is called the Gouy-Chapman layer and forms a net positive region of ions that span a distance on the order of the Debye length of the solution. The Debye length, λ_D , is about 10nm from the wall for symmetric univalent electrolytes at 1mm concentration. Applying an external electric field parallel to the wall will cause the ions to move and drag the neutral molecules with them, resulting in a net bulk liquid motion along the wall (Zeng, Chen et al. 2001).

Two types of electro-osmotic pumps have been described in the literature, one in a porous media and the other a planar one, which are both currently under development. It has been shown that there is a linear relationship between pressure and flow rate that the electro-osmotic pump can generate.

Zeng *et al.* developed and characterized electro-osmotic micropumps (Zeng, Chen *et al.* 2001). The micropumps were fabricated by packing 500-700 3.5- μm diameter, fused-silica capillaries with 3.5- μm diameter non-porous silica particles. They achieved pressures in excess of 20 atm and a maximum flow rate of 3.6 $\mu\text{l}/\text{min}$ with a maximum thermodynamic efficiency of 1.3% for water as the working fluid. Although this pump generated a very high pressure head, its rate of flow was quite low compared to the ones provided by other EHD pumps.

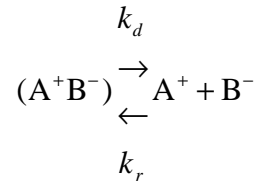
Yao *et al.* recently developed electro-osmotic micropumps that provide maximum flow rates and pressure of 33 ml/min and 1.3 atm, respectively, at applied potential 100 V (Yao, Hertzog *et al.* 2003). However, since in this type of micropump an electrolyte solution must be used, controlling electrolyzed reaction and the generated electrolytic gas streams is challenging. To work around with this issue, Yao *et al.* have proposed a catalytic recombination system.

For more information about electro-osmotic flow see Karniadakis and Beskok 2002 and Madou 2002).

3.2.4 Conduction Pumping Mechanism

The conduction pump operation mechanism relies on the conductivity of the working fluid. Like the ion-injection pump, the conduction pump driving force is the Coulomb force acting on the ions inside the fluid. However, the source of these ions is

the dissociation of neutral species. The simplest model conduction model is a reversible process of dissociation-recombination of a neutral species (denoted A^+B^-) into univalent positive A^+ and negative B^- ions as presented by Eq. (2-11).



(2-11)

where k_d and k_r are the dissociation and recombination coefficient rates, respectively. Since the number of positive and negative generated charges is identical in this process, the Coulomb force vanishes in the bulk of liquid. However, in the vicinity of the electrodes, the positive and negative charge densities are not equal, and a heterocharge layer is formed. Heterocharge means that the charge has the opposite polarity from that of the adjacent electrode. For example, in the neighborhood of a positive electrode the concentration of negative ions exceeds that of positive ions. The heterocharge layer is a characteristic of dielectric liquids of low electrical conductivity ($\sigma_e < 10^{-7}$ S/m), while in conductive and electrolyte liquids the electric double layer (EDL) is identified by the Debye length λ_D . For high values of the electrical conductivity, the electric field in a heterocharge layer is much greater than the field existing in the liquid bulk. The typical thickness of the heterocharge layer, λ_H , is expected to be the length traveled by the ions during the relaxation time $\lambda_H \sim \mu_e E(\epsilon/\sigma_e)$.

Now consider two-plane parallel electrodes placed inside a liquid. If a potential difference is applied to the electrodes, the heterocharge layers will be formed in the neighborhood of them in which the electric field intensifies. Due to the symmetry, the

thicknesses of the heterocharge layers at the positive and the negative electrodes are identical. On the other hand, using Eq. (2 25), it can be shown that the pressure difference between any two points in a one-dimensional problem and in the absence of the fluid motion is given by:

$$p_2 - p_1 = \frac{\epsilon}{2}(E_2^2 - E_1^2) \quad (3-1)$$

Now, let's use this equation for two points. The first point is chosen inside the heterocharge layer of the positive electrode, and the second point is placed in the middle of the two electrodes. Since the electric field intensity in the heterocharge layer is higher than its outer region, $E_1 > E_2$ and consequently, a pressure gradient from point 2 towards point 1 is created. The same pressure head will be created if the first point is located inside the heterocharge layer of negative (or ground) electrode. Therefore, two-plane parallel electrode geometries do not result in a net pressure head since the positive and the negative heterocharge layers counterbalance the effects of each other.

With the change of electrode configuration it is possible to establish a net pressure head between the electrodes. One such electrode geometry was presented by Jeong *et al.* (Jeong, Seyed-Yagoobi et al. 2003). In this configuration, the strong electric fields build up the heterocharge layers around the electrodes. However, the net pressure generation around the ring ground electrode is almost canceled because of the geometrical symmetry. The pressure generation around the high-voltage electrode mainly contributes to the net axial flow. Since the electric field is higher around high-voltage electrode, the heterocharge layer will be thicker, and the pressure across it will be higher as well. Therefore, the flow direction will be from the ground electrode to the high voltage electrode. Notice that since the direction of conduction pumping is opposite that of the

ion-injection pumping, the design of electrodes must be such that no sharp points are formed.

Atten *et al.* studied the concept of conduction pumping (Atten and Seyed-Yagoobi 2003). According to their investigation, the electric conductivity of the working fluid does not play a role in pressure head generation when the EHD effect is achieved solely through conduction. They also designed and fabricated a static pump to experimentally investigate the pressure head generated through pure conduction. Two working fluids (Refrigerant R-123 and n-hexane) and two different electrode designs are considered in their study. A maximum pressure head of 500 Pa and an electrical current of 70 μ A for R-123 liquid at 20 kV were obtained using a single-ring electrode design. The corresponding input power was about 1.4 W. For the needle-electrode geometry and for the same working fluid, the maximum pressure head and current head were about 100 Pa and 35 μ A at voltage about 15 kV. Beyond this electrical voltage, the pressure head suddenly dropped and the ion-injection process was observed. Similar experiments were carried out with n-hexane as working liquid. The pressure heads generated with n-hexane were lower than those achieved with R-123 under identical applied voltage. Atten *et al.* also suggested that application of the conduction pump could be extended to AC fields provided that the corresponding AC time period is much longer than the liquid relaxation time (ϵ/σ) so that the system will be in a quasi-steady state.

The major advantage of the conduction pumping is generally believed to be a reduced possibility of harmful electrochemical reactions inside the working liquid due to the high voltage application. However, the major drawback of this pumping mechanism

might be its strong sensitivity to impurities in the fluid. This can result in reliability issues and non-repetitive performance.

3.3 A Review of a Selected Non-EHD Micro Pumping Mechanisms

In the previous section a review of the EHD pumping mechanisms was presented. However, in past two decades, a large group of pumping mechanisms has also been developed for which the actuation mechanisms do not rely on the EHD force. A number of these pumping mechanisms are, including but not limited to, shape memory alloy, piezoelectric, pneumatic, magnetohydrodynamic (MHD), electrostatic, bimetallic, and thermopneumatic actuations. In contrast to EHD pumps, most of these pumps are mechanical pumps in which a moving part (e.g., a diaphragm) exists. In this section some of these pumping mechanisms are briefly reviewed.

One of the pumping mechanisms is based on piezoelectric actuation. Typically, a piezoelectric micropump is comprised of a pump body, a membrane driven by piezoelectric actuator, and usually microvalves. Most of the piezoelectric micropumps that have been developed are of the reciprocating type where an excited oscillating membrane induces periodic volume and pressure change in a pump chamber. This alternating flux is transformed by passive valves, at the inlet and outlet of the pump chamber, into a directed net volume flow along a positive pressure gradient. Some micropump designs have also been proposed in which nozzle/diffuser elements instead of check valves are used. One of the disadvantages of a micropump using passive check valves is the restriction of the driving frequency.

Gerlach *et al.* developed and fabricated a micropump based on silicon technologies (Gerlach, Schuenemann et al. 1995; Gerlach and Wurmus 1995). The

actuator was a piezoelectric transducer (PZT) disk 200 μm thick glued on top the membrane, forming a bimorph actuator. The micropump typically delivered the maximum static pressure head and volumetric flow rates of 3.5 kPa and 400 $\mu\text{l}/\text{min}$, respectively, at 3 kHz frequency for water as working fluid.

More information about piezoelectric micropumps can be found in works of Shoji *et al.* (Shoji, Nakagawa *et al.* 1990), Stehr *et al.* (Stehr, Messner *et al.* 1996), and Koch *et al.* (Koch, Evans *et al.* 1998).

The various piezoelectric micropumps can typically generate pressure heads around 10 kPa and volumetric flow rate in the range of few hundreds micro liter per minute. The main advantage of this type of actuation is that a variety of fluids can be pumped. However, it has also some drawbacks. Since silicon does not exhibit any piezoelectric effects, it is difficult to convert the electrical signal to mechanical deflection in silicon-base devices. Moreover, the piezoelectric actuation generally suffers from wear, fatigue, temperature sensitivity, hysteresis, and limited lifetime.

The thermopneumatic actuation is another pumping mechanism. A thermopneumatic actuator has a sealed pressure chamber and movable membrane. The thermopneumatic micropump typically consists of a sealed chamber, a heating element that controls the chamber inner gas temperature, a membrane, check valves, and micropump body. As a result of the temperature increase, the gas inside the sealed chamber expands, causing the membrane deflection. This in turn drives the fluid inside the pump body outward. The rising time of the actuator depends on the heat capacitance and available power of the heater, while the relaxation time is determined by the heat transfer of the external environment.

Jeong and Yang (2000) presented a microfabricated thermopneumatic micropump. The micropump consisted of a P⁺ corrugated silicon diaphragm, a micro heater and a pair of nozzle/diffusers. The diaphragm was driven by the air sealed cavity pressure variation caused by the ohmic heating and the natural cooling. As the diaphragm of the micropump vibrated, the fluid flowed in one direction through the nozzle/diffuser. The maximum flow rate of the micropump was about 14 $\mu\text{l}/\text{min}$ at 4 Hz for the input voltage of 8 V.

Bustgens *et al.* also manufactured a thermopneumatic micropump using combined thermoplastic molding and membrane techniques (Bustgens, Bacher *et al.* 1994). The lateral dimensions of the complete pump were 7 mm \times 10mm. The depth and the diameter of the pump chamber were 100 μm and 4 mm, respectively. The membrane was driven by an integrated thermopneumatic actuator. The air enclosed in the actuator chamber located on top of the membrane was heated by an electric current in a titanium wire. A micromembrane pump made of PSU was driven by short pulses (58 ms) of 15 V at a frequency of 5 Hz. The pump membrane was deflected 100 μm towards the bottom of the pump chamber. A flow rate of 44 $\mu\text{l}/\text{min}$ and a differential pressure of 3.8 kPa were achieved. The average power consumption of the micropump was 0.45 W.

The basic advantage of the thermopneumatic micropump is a relatively large pressure head generation. The disadvantages of this pumping technique are the dependency of the response time on environment conditions and typically low generated flow rates (in the order of a hundred micro liters per minute). Besides, this pumping mechanism needs microvalves to operate.

Magnetohydrodynamic (MHD) pumping is a non-mechanical pumping concept (similar to EHD pumps). Magnetohydrodynamics refers to the coupling of an electromagnetic field and a velocity field in an electrically conducting fluid. In magnetohydrodynamic theory, if charged particles move through a region where both an electric field and a magnetic field are present, a magnetic force acts on the moving charged particles (some times called the Lorentz force). The direction of this force is perpendicular to the plane containing the magnetic flux density and current density vectors. For the constant magnitude of current and magnetic flux vectors, this force reaches its maximum when these two vectors are perpendicular. The major characteristic of the MHD concept is its applicability in electrical conductive liquids, distinguishing it from the EHD phenomenon, where dielectric liquid has to be utilized.

A number of studies on MHD micropumps have been reported so far. Huang *et al.* reported their effort to design, microfabricate and test a DC-type MHD micropump using a LIGA microfabrication technique (Huang, Wang *et al.* 2000). In their design the external magnetic field was supplied using permanent magnets. The micropump channel had a $500 \mu\text{m} \times 800 \mu\text{m}$ cross-sectional area and 20 mm length. Experiments were run for four different fluids: 2% sodium hydroxide (NaOH) in water, 1% ammonium chloride (NH_4Cl) in water, ethyl alcohol, and tap water. Although the static pressure heads were not reported, the average flow rates were measured for a range of applied potential. A flow rate up to $1200 \mu\text{l}/\text{min}$ for 2% solution of NaOH at 14V was achieved, though the flow rates were generally unstable and finally decreased to zero for all solutions when run for long durations (several hundred of seconds). It was reported that this was due to bubble generation resulting from the electrolysis of the pumping fluids.

Jang *et al.* reported another design for an MHD micropump (Jang and Lee 2000). In this design the micropump consisted of anisotropic, bulk-etched microchannel, upper and lower aluminium (AL) electrodes, and two permanent magnets. The microchannel was 1 mm wide, 0.4 mm high and 40 mm long. Seawater was used as the pumping liquid ($\sigma_e = 4 \text{ S/m}$). The performance levels of the micropump were obtained by measuring the pressure head difference and flow rate as the applied voltage changed from 10 to 60 V_{DC} at 0.19 and 0.44 Tesla. The pressure head difference was 180 Pa at 38 mA and 60 V, and the flow rate was 63 $\mu\text{l}/\text{min}$ at 1.8 mA when the inside diameter of the inlet/outlet tube was 2 mm and the magnetic flux density was 0.44 T. In a static pressure test a saturation of pressure head over 45 V was observed. In addition, the generation of bubbles due to the electrolysis of the seawater was reported.

Zhong *et al.* reported the use of magneto hydrodynamic pump to circulate fluids in conduits fabricated with low temperature, co-fired ceramic tapes (Zhong, Yi et al. 2002). Conduits were fabricated in toroidal and rectangular shaped loops. Electrodes printed on the ceramic substrate along the conduits' walls facilitated transmission of electric currents through the test fluids. The pumping liquid consisted of mercury slugs ($\sigma_e \approx 10^6 \text{ S/m}$), saline solution ($\sigma_e = 2.2 \times 10^{-3} \text{ S/m}$), and deionized water ($\sigma_e = 2.2 \times 10^{-4} \text{ S/m}$). The toroidal conduit that was used in the experiments with mercury was 22 mm in inner diameter, 2.2 mm wide, and 700 μm deep. The toroidal conduit that was used in the water experiment was 1.4 mm wide and 700 μm deep. The inner part of the rectangular loop was 13.5 mm long and 6.7 mm high, and the conduit's width and height were, respectively, 1.2 mm and 700 μm . For the mercury, the maximum slug's velocity reached 20 cm/s, corresponding to a flow rate of about 18.5 $\mu\text{l}/\text{min}$ at 0.9 V in a capped toroidal

conduit. For the saline solution, the maximum velocity was about 12 mm/s, corresponding to a flow rate of around 0.7 $\mu\text{l}/\text{min}$ at 4 V in a toroidal conduit, and this velocity in the rectangular loop was around 0.15 mm/sec, corresponding to a flow rate of about 0.009 $\mu\text{l}/\text{min}$ at 2 V.

The major characteristic of MHD micropumps is their applicability to electrical conductive liquids, distinguishing them from EHD micropumps where dielectric liquid has to be utilized. In a conductive liquid, since the number of positive and negative charge carriers is in the balance, the coulomb forces acting on positive and negative charges counterbalance each other and hence, no net electrohydrodynamics pumping effect is generated, while under the magnetohydrodynamic effect the current density vector is independent of the charge carrier's polarity, and a normal force acts on the charge carriers. The major disadvantage of MHD micropumps is the electrolysis of the working fluid and gas generation.

3.4 Numerical Modeling of the Electrohydrodynamics Phenomenon

In this section a number of EHD numerical modeling efforts reported in the literature are briefly reviewed. The EHD phenomenon is a complicated process, since numerous factors are involved. These factors include geometrical parameters, working fluid properties, electro-chemical reaction factors, and many others. Understanding the physics of the EHD process is also still the subject of many ongoing studies, and various questions have yet to be answered. These issues make the numerical modeling of the EHD process extremely challenging. However, using simplified models, a number of numerical studies have been carried out. Depending on the considered medium, the efforts on modeling the EHD process can be divided into two major categories: EHD

numerical simulations inside gases and liquids. Although the governing equations for these two modeling classes are nearly similar, the physics of the EHD phenomena inside gases is better understood. Since most of the EHD applications involve the electrophoresis (Coulomb) force, most numerical simulation efforts have also modeled the electrophoresis action.

For gases, many EHD numerical modeling studies have been reported. Yabe *et al.* carried out numerical and experimental studies on the corona wind between wire and plate electrodes (Yabe, Mori et al. 1978). They calculated the two-dimensional steady incompressible viscous flow field between wire and plate electrodes, taking into account the Coulomb force on the ions. The pressure distribution on the plate obtained by their numerical calculations agreed well with the experimental values near the maximum value. It was also shown that the fluid field was circulating one.

Medlin *et al.* developed a numerical technique for the solution of the governing equations of coupled space-charge and electric field problems, including terms for charge advection and diffusion (Medlin, Fletcher et al. 1998). The methodology involved writing the governing equations in pseudotransient form and discretising using the finite volume method on a structured grid. However, the solution was limited to the electrical equations only, and the fluid flow governing equations was not solved.

Owsenek and Seyed-Yagoobi examined the heat transfer enhancement resulting from the corona wind (Owsenek and Seyed-Yagoobi 1997). The geometry consisted of a fine-wire electrode suspended in the open air above a grounded and heated horizontal surface. An infrared camera system was used to obtain the distribution of local heat transfer coefficients on the corona wind impingement surface. A numerical code was

developed and verified by comparison with the experimental data. The numerical solution technique involved the simultaneous solutions of the discretized Poisson and current conservation equations (see section 2.3.1) in Cartesian coordinates, yielding the current density and electric field.

Many other numerical modeling studies on corona wind and EHD process have also been reported (McDonald, Smith et al. 1977; Kallio and Stock 1986; Dulikravich, Ahuja et al. 1993; Adamiak 1994; Abdel-Salam and Al-Hamouz 1999; Feng 1999; Kim and Whang 2000).

A number of numerical analyses of the EHD mechanism inside liquids have been reported in literatures. In some of these works the EHD pumping action was of interest, while in others the generated charge density, electric, and fluid flow fields were studied.

Seyed-Yagoobi *et al.* (Seyed-Yagoobi, Brayan et al. 1995) improved the one-dimensional theoretical model for an ion-injection pump developed by Melcher (Melcher 1981). The electrode geometry consisted of two parallel grids. All three components of the given density (i.e. conduction, convection, and ionic mobility) were considered, and the distribution of the charge density and electrical field under various conditions was obtained. The solutions presented in nondimensional form. The power efficiency was also found. According to their results, the efficiency increases asymptotically with an increase of $\epsilon U / \sigma_e L$ factor.

Higuera (2000) conducted a numerical study on the EHD flow of a dielectric liquid around a blade electrode. In this investigation, the injection of charge from a blade-shaped, metallic electrode into a dielectric liquid and the Coulomb force that set the liquid into motion were studied. An analysis of this motion and its influence on the

transport of electric charge was carried out for a simple charge injection law. A current pulse regime has been found for low currents.

In most of the EHD numerical modeling works, a unipolar charge injection process with a constant conduction coefficient was taken into account. Pontiga and Castellanos (1996) investigated not only the effect of charge injection but also the dissociation of ionic pairs leading to the electrical conduction process (see section 2.3.1.1). In their analysis the effect of electrophoresis (Coulomb) force on fluid flow was not studied. However, the electrical field and the charge densities of the positive and negative ions were calculated for a one-dimensional problem. Moreover, in their model, the variation of liquid conductivity due to the electric field was considered. The numerical results provided the relationship between the electrical current density and the applied potential. It was also shown that the injection and dissociation may contribute very differently to the total current density, depending on the regime of conduction.

Jeong *et al.* modeled the EHD pumping through conduction phenomenon (Jeong, Seyed-Yagoobi *et al.* 2003). In their analysis, the charge generation due to ion dissociation in the absence of a direct charge injection was modeled. Furthermore, the conduction pumping associated with the dissociation of ionic pairs was calculated, and the pressure head in the absence of liquid flow was evaluated. In their numerical code, the finite volume technique was utilized. The numerical results confirmed the EHD conduction pumping concept theoretically. However, the experimentally measured pressure generations were significantly higher than those numerically predicted.

3.5 Summary

In this chapter some of the earlier works on micropumps as well as related basic research on the EHD phenomena and its applications as related to the present work were reviewed. These studies were divided into EHD pumping mechanisms, non-EHD meso and micro pumping mechanisms, and numerical modeling of the EHD phenomenon. For ion-injection pumps, a subset of EHD pumping mechanisms, a summary of reported experimental works was presented. In the next chapter the numerical modeling procedure will be studied in detail.

CHAPTER 4: NUMERICAL MODELING

4.1 Introduction

In this chapter, the methodology of numerical modeling for electrohydrodynamic processes is presented. As discussed previously, electrohydrodynamics is a complex phenomenon involving the interaction between the electrical and fluid flow fields. The modeling of this process is essentially unfeasible unless several reasonable assumptions and simplifications are made. In the current research, it is not intended to model the interaction of ions and molecules at the molecular level, but rather to find the global effect of an electric field on the fluid flow using a continuum assumption. This assumption can be justified by the fact that the typical length scales in the current research and many similar studies are several times larger than the intermolecular distances.

For the numerical modeling, two classes of EHD problems are simulated. In both classes, the source of motion is the Coulombic force acting on the fluid. However, the difference is in the type of charged carriers participating in the EHD process. In the first approach, only the unipolar ion injection process with an ohmic conduction is considered, and migration of only one type of charge carrier is modeled. In the second approach, the dissociation and recombination of both ion polarities as well as a unipolar ion injection process are taken into account, and the interaction between both ion polarities is simulated. The major application of the first modeling class is to simulate the corona wind in gases and the ion injection EHD pumps, while the second approach is useful to

study the conduction pumping process and the conduction/injection interactions. For each of these approaches, the governing equations, simulation methodologies, and validations of the methods are presented.

4.2 Numerical Modeling for Two Classes of Problems

The objective of numerical simulation is to develop a computational tool to model the fluid flow and thermal fields induced by the EHD process and to study the effects of different governing parameters on the performance of the system. Two modeling approaches have been adopted, which will be discussed in detail in the following sections.

4.2.1 Unipolar Charge Injection with Ohmic Conduction

Consider a pair of electrodes consisting of an emitter and a collector placed inside a fluid. If a high enough electrical potential difference is applied to these two electrodes, the charge injection process in the neighborhood of the emitter will take place. The injected charge carriers migrate toward the collector, dragging the liquid molecules alongside. This process leads to motion of the bulk fluid. Due to the potential difference, an electrical current is established between the electrodes. Three factors contribute to the electrical current flow. The first factor is the migration of injected charge carriers through the emitter under the effect of electric field; the second is the ohmic conduction due to dissociation of ionic pairs; and the third factor is the convection of the injected charges due to fluid movement. The conduction and convection effects of charges are generally negligible in gases (Davidson, Kulacki et al. 1987; Castellanos 1998). Among these factors, the only one that leads to a net Coulombic force on the fluid is the migration of

injected ions. In fact, the conduction and convection do not result in any fluid motion and momentum transfer. In modeling this process, it is assumed that in terms of polarity, only one kind of charge carrier exists (i.e., only positive or negative ions), and these charge carriers are similar species (i.e., they have identical charge mobility). These assumptions will become more apparent when the governing equations are reviewed.

4.2.1.1 Governing Equations

The theoretical model is developed based on the following assumptions:

1. The model is three-dimensional.
2. Only electrophoretic (Coulombic) force is present.
3. Ionization and charge injection take place only at the emitter electrode.
4. The thickness of the ionization layer around the emitter electrode is too small to be considered.
5. The entire inter-electrode spacing is filled with unipolar space-charge of the same polarity as the emitter electrode.
6. Diffusion of ions is neglected.
7. The conduction coefficient (σ_e) does not depend on the electric field.
8. The mobility of ions is constant and independent of the electric field intensity.
9. The fluid flow is steady-state and incompressible.

The governing equations, introduced in section 2.3, are summarized here to clarify the solution methodology.

In the absence of dielectrophoretic and electrostrictive forces, the conservation of mass, momentum, and energy for an incompressible fluid yield

$$\nabla \cdot \mathbf{u} = 0 \quad (4-1)$$

$$\mathbf{r}(\mathbf{u} \cdot \nabla) \mathbf{u} = -\nabla p - m \nabla^2 \mathbf{u} + \mathbf{r} \mathbf{g} - \mathbf{r}_e \nabla f \quad (4-2)$$

$$\mathbf{u} \cdot \nabla T = \nabla \cdot (\mathbf{a} \nabla T) + \frac{\mathbf{n}}{c_p} \mathbf{f} + \frac{|\mathbf{m}_e \mathbf{r}_e| (\nabla \mathbf{f})^2 + \mathbf{s}_e (\nabla \mathbf{f})^2}{\mathbf{r} c_p} \quad (4-3)$$

The Poisson equation (also known as Gauss's law) and conservation of charge are given as

$$\mathbf{e} \nabla^2 f = -\mathbf{r}_e \quad (4-4)$$

$$\frac{\partial \mathbf{r}_e}{\partial t} + \nabla \cdot \mathbf{J} = 0 \quad (4-5)$$

where for the unipolar charge injection with the ohmic conduction, the current density is defined as

$$\mathbf{J} = \mathbf{m}_e \mathbf{r}_e \mathbf{E} + \mathbf{s}_e \mathbf{E} + \mathbf{r}_e \mathbf{u} \quad (4-6)$$

where the terms on the right-hand side represent the ionic mobility, conduction, and convection components, respectively. The electric field is related to electrical potential as

$$\mathbf{E} = -\nabla f \quad (4-7)$$

For gases, the electrical conductivity is practically zero. Thus, the ohmic conduction term can be neglected. When the magnitude of the bulk fluid velocity u is much less than the ion drift velocity $V_e = \mathbf{m}_e \mathbf{E}$, the convection term may be dropped from the current density relation. Typically, ionic motilities for gases are greater than $10^{-4} \text{ m}^2/(\text{V}\cdot\text{s})$. The typical electric field intensity is not less than $50 \times 10^4 \text{ V/m}$, and consequently, values of V_e on the order of 50 m/s are possible. Thus the neglect of the

convective current for gases is reasonable when mean velocity is on the order of 5 m/s or less. Therefore, for gases, the current density is given as

$$\mathbf{J} = m_e r_e \mathbf{E} \quad (4-8)$$

The total electrical current flowing between electrodes can be calculated by

$$I = \int_A \mathbf{J} \cdot d\mathbf{A} \quad (4-9)$$

where A can be any area providing that the entire current density crosses it.

Therefore, the series of equations (4-1)-(4-5) consists of five equations and five unknowns, i.e. \mathbf{u} , p , T , \mathbf{f} , and r_e . In general, the continuity, momentum, Poisson, and charge conservation equations form a system of coupled equations that must be solved simultaneously. Notice that based on the governing equations, there is a double coupling between the electric field and fluid field meaning that each of these fields can be affected by the other. This fact demonstrates the challenges associated with the computational process. However, for gases, the Poisson and charge conservation equations are independent of the fluid flow and can be numerically solved in advance.

4.2.1.2 Boundary Conditions

The boundary conditions for the momentum and energy equations are obvious. The boundary conditions for electric potential, \mathbf{f} , are rather straightforward to describe. At the emitter electrode surface $S_{emitter}$ and collector electrode surface $S_{collector}$, Dirichlet boundary conditions can be specified based on knowledge of the applied voltages. Typically, we have

$$\mathbf{f} = \mathbf{f}_{emitter} \text{ on } S_{emitter} \quad \text{and} \quad \mathbf{f} = 0 \text{ on } S_{collector} \quad (4-10)$$

For other surfaces, a perfect electrical insulation without charge accumulation is generally assumed. Therefore, Neumann's boundary conditions can be applied

$$\partial \mathbf{f} / \partial n = \mathbf{n} \cdot \nabla \mathbf{f} = 0 \quad \text{on all surfaces except the emitter and collector} \quad (4-11)$$

where \mathbf{n} is the local unit normal vector of the corresponding surface.

For the boundary condition of charge density (i.e. \mathbf{r}_e) at the emitter electrode different options have been suggested. For an autonomous ion injection, the charge density is assumed to remain constant.

$$\mathbf{r}_e = \mathbf{r}_{e,emitter} \quad \text{on } S_{emitter} \quad (4-12)$$

However, the value of $\mathbf{r}_{e,emitter}$ is not explicitly available. One option is to specify

$\mathbf{r}_{e,emitter}$ based on the experimentally measured electrical current, I_{exp} . In this case the charge density at the emitter is set such that the calculated electrical current is matched with the experimentally measured electrical current.

$$\mathbf{r}_e = \mathbf{r}_{e,emitter} \quad \text{on } S_{emitter} \quad \text{so that } I_{exp} = \int_A \mathbf{J} \cdot d\mathbf{A} \quad (4-13)$$

For gases, another approach based on Kaptsov's assumption (see section 2.6.3.2) can be adopted. However, Kaptsov's assumption does not provide a direct description of

$\mathbf{r}_{e,emitter}$ but rather specifies that

$$\mathbf{n} \cdot \nabla \mathbf{f} = E_c \quad \text{on } S_{emitter} \quad (4-14)$$

where E_c is the corona onset field and \mathbf{n} is the local unit normal vector that points into the emitter surface. To satisfy Eq. (4-14) in numerical solutions, a value of $\mathbf{r}_{e,emitter}$ is initially assumed in Eq. (4-12). Then, the electric field intensity at the emitter surface is

computed from the obtained solution, and its comparison with the value of E_c according to Eq. (4-14) determines a new value of $\mathbf{r}_{e,emitter}$ for the next iteration. After many such iterations, a consistent value of $\mathbf{r}_{e,emitter}$ can be obtained which satisfies Eq. (4-14). In the case where the emitter electrode is a wire, a reasonably accurate value of E_c can be obtained from Peek's formula (see Eq. (2-42)).

The other option for the emitter charge density boundary condition is to use the available relation of the injected charges for non-polar liquids as given by Eq. (2-44). This technique will be discussed in the next sections.

In the absence of the diffusion term, a boundary condition for the charge density at other boundaries including the collector should also be specified to complete the mathematical description of the problem. Since there is no definitive knowledge available for the charge distribution at these boundaries, it is usually safe to apply a Neumann boundary condition.

$$\mathbf{n} \cdot \nabla \mathbf{r}_e = 0 \quad \text{on } S_{collector} \text{ and other boundaries}$$

(4-15)

4.2.1.3 Discretisation

In order to illustrate the numerical solution methodology, discretisation of the equations will be briefly reviewed. Without losing generality, the discretised form of equations will be developed for a structural Cartesian 2D grid.

The discretised forms of the momentum and energy equations for various numerical schemes have been well established in the literature and are not discussed here (see (Ferziger and Perić 2002)). Notice that the electrical body force and Joule heating terms that appear in these equations are treated like other source terms.

For discretisation of the electrical equations, i.e., Eqs. (4-4) and (4-5), consider the numerical grid shown in Figure 4-1.

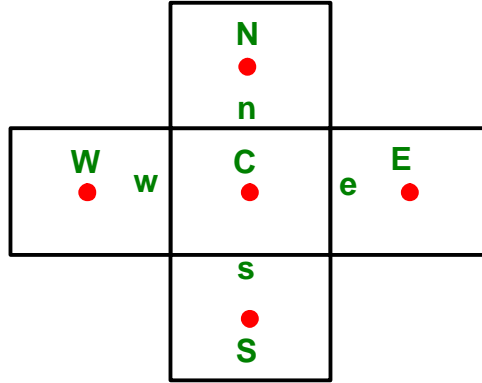


Figure 4-1 Computational grid

Discretisation of the Poisson equation, leads to

$$\left[(\partial \mathbf{f} / \partial n)_e A_e - (\partial \mathbf{f} / \partial n)_w A_w \right]^{k+1} + \left[(\partial \mathbf{f} / \partial n)_n A_n - (\partial \mathbf{f} / \partial n)_s A_s \right]^{k+1} = \left(\frac{-\mathbf{r}_C}{\mathbf{e}} \right)^k dV_P \quad (4-16)$$

where n, s, e, and w denotes the positions on the control volume faces. A and dV are the face area and the volume of the corresponding control volume element, respectively. k and $k+1$ indicate two successive iteration numbers. n is the normal unit vector of the control volume face. This equation can be simplified to the following form:

$$\left[\mathbf{f}_E^{k+1} A_e + \mathbf{f}_W^{k+1} A_w + \mathbf{f}_N^{k+1} A_n + \mathbf{f}_S^{k+1} A_s - (A_e + A_w + A_n + A_s) \mathbf{f}_C^{k+1} \right] = \left(\frac{-\mathbf{r}_C}{\mathbf{e}} \right)^k dV_P \quad (4-17)$$

The discretised form of the charge conservation equation can be written as

$$\frac{dV_P}{dt} \mathbf{r}_C^{k+1} = - \left[\langle \mathbf{r}_C \rangle_e V_e^* A_e - \langle \mathbf{r}_C \rangle_w V_w^* A_w \right]^k + \left[\langle \mathbf{r}_C \rangle_n V_n^* A_n - \langle \mathbf{r}_C \rangle_s V_s^* A_s \right]^k + \left(\frac{1}{dt} - \frac{\mathbf{s}_e}{\mathbf{e}} \right) \mathbf{r}_C^k dV_P \quad (4-18)$$

where V^* stands for the component of the vector $m\mathbf{E} + \mathbf{u}$, which is co-directional with the unit normal vector, \mathbf{n} . $\langle \mathbf{r}_c \rangle$ denotes the charge density value on the face of the control volume, and different schemes, such as the first order or second order upwind methods, can be used to determine this value. Notice that arithmetic averaging between the two adjacent control volumes leads to instability of the solution.

Eq. (4-5) and its discretised form, Eq. (4-18), were written in a time dependent form, even though we are interested in a steady-state solution. This is due to the fact that here, time can be thought of as a relaxation parameter, controlling the rate and stability of the approach to the steady state solution.

4.2.1.4 Implementation of the Solution Technique to the Fluent Solver

To ascertain the correctness of the solution methodology and discretisation of the equations, a two-dimensional Cartesian numerical code was initially developed and its performance was verified. However, since usability of this numerical code was limited to simple geometries, the solution methodology was implemented in Fluent[®], a commercial powerful numerical code, to extend the application of the numerical modeling.

Although there is no standard built-in function in Fluent to solve the governing electrical equations of EHD, it is possible to define a user-defined function that can be dynamically loaded with the Fluent solver to enhance the standard features. The general form of the transport equation for an arbitrary scalar Φ_j that can be solved by Fluent, using a user-defined function is

$$\frac{\partial \mathbf{r}\Phi_j}{\partial t} + \frac{\partial}{\partial x_i} \left(\overline{\mathbf{r}u_i}\Phi_j - \Gamma_j \frac{\partial \Phi_j}{\partial x_i} \right) = S_{\Phi_j} \quad j = 1, 2, \dots, N$$

(4-19)

where Γ_j and S_{Φ_j} are the diffusion coefficient and the source term supplied by the user for each N scalar equation.

To convert Eq. (4-4) into the form of Eq. (4-19), the variables are defined as follows:

$$\Phi_1 = \mathbf{f}, \quad \Gamma_1 = e, \quad S_{\Phi_1} = \mathbf{r}_e, \quad \text{and} \quad \overline{u_i} = 0$$

(4-20)

Furthermore, the transport equation must be solved in its steady state form.

For the charge conservation equation, Eq. (4-5), the corresponding variables of Eq. (4-19) are defined as

$$\Phi_2 = \mathbf{r}_e, \quad \Gamma_2 = 0, \quad S_{\Phi_2} = -\frac{\mathbf{r}\mathbf{S}_e}{e} \mathbf{r}_e, \quad \text{and} \quad \overline{u_i} = \mathbf{m}\mathbf{E}_i + u_i$$

(4-21)

In order to evaluate each of these terms, a special macro should be written so that each computational control volume is specified and calculated. Special treatment is needed to define the advective flux term for the user-defined charge density transport equation. This is because Fluent stores the gradient of the user-defined scalars on the centroids rather than on the faces of the control volume. For the computation of the advective flux term, the face normal component of $E = -\nabla \mathbf{f}$ on each control volume face is required. An arithmetic averaging of the gradient term between neighboring centroids does not provide adequate accuracy for non-uniform and unstructured grids. For a higher order accuracy calculation of this term on each face, not only the charge density

gradient but also its own value on the adjacent control volume centroids must to be taken into account.

To implement the source terms of the momentum and energy equations, again special macros must be used. Through these macros the geometrical parameters of computational cells and the value of different variables are accessible.

The written user-defined code contains the following Fluent macros:

1. A source-term macro to define the charge density equation source term;
2. A source-term macro to define the potential equation source term;
3. A convective-flux macro to define the convection terms of the potential and charge density equations;
4. A diffusivity defining macro to set the diffusivity coefficient for the charge density and potential equations;
5. Three source-term macros to define the body forces for the three components of the momentum equation;
6. A source-term macro to define the source term for the energy equation;
7. A macro to calculate the three components of current density vector defined in Eq. (4-6) at the cell centroids. These stored variables will be used to calculate the total current passing through the electrodes.

4.2.1.5 Numerical Solution Algorithm

The overall algorithm for solving the system of Eqs. (4-2), (4-3), (4-4), and (4-5) to the converged solution is summarized in following steps:

1. Set the boundary conditions of the governing equations appropriately.

2. Set the initial values for the charge density, ρ_c , equal to zero and for the electrical potential, ϕ , equal to the arithmetic average of the applied potential difference to the electrodes. Set the initial values of the velocity and temperature fields accordingly.
3. Turn on the potential Poisson equation solver and solve the equation in the absence of any charge density field. Continue until a converged solution is obtained.
4. Turn on the charge density transient equation solver and solve both charge density and potential Poisson equations simultaneously. Continue until a steady state solution is obtained.
5. In the cases of gases, turn off the charge density and potential equations and turn on the steady state momentum equation. Solve until a converged solution is obtained. Now, turn on only the energy equation and solve until a converged solution is reached. In case of liquids, solve the potential, charge density, and momentum equations, simultaneously, and continue until a steady state solution is found. Solve the energy equation afterwards and obtain a converged solution.
6. Calculate the electrical current and compare it with the experimentally measured current. If it matches report the results; otherwise, change the emitter charge density boundary value and return to step 2.

4.2.1.6 Verification of Numerical Modeling Technique

In this section, the validity of the developed numerical solution methodology is reviewed. Two cases are taken into account where the numerical solutions are compared against the analytical and experimental results, respectively.

A. One-Dimensional Ion-Injection Pumping

Consider two parallel permeable electrodes placed inside a fluid passage forming emitter and collector electrodes. The structure of electrodes is such that the flow can pass through them without any resistance. A high potential difference is applied between the electrodes, and due to the ion-injection process a pressure head is generated between these two electrodes. Let's assume that the problem is one-dimensional; i.e., all the variables are only a function of the x coordinate. This might be a hypothetical situation; however, two mesh-type electrodes can nearly satisfy this condition.

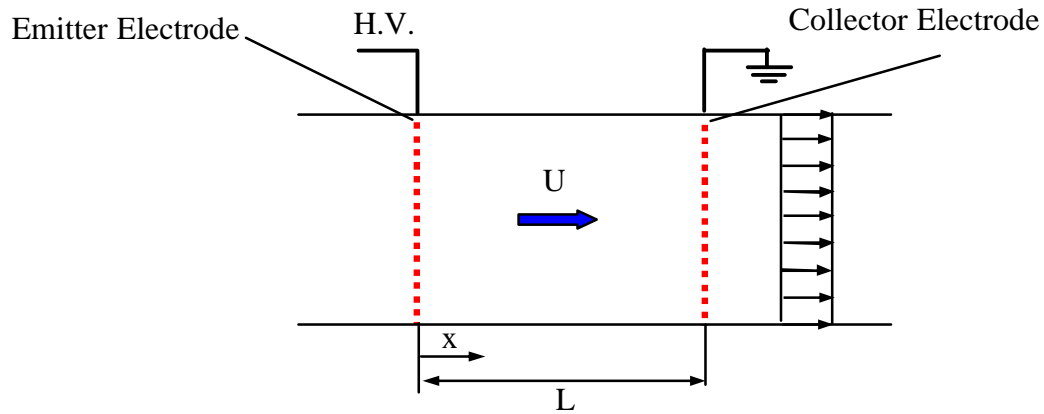


Figure 4-2. Schematic of one-dimensional unipolar ion-injection pumping

Melcher (Melcher 1981) derived an analytical solution for the one-dimensional unipolar ion-injection process when the electrical conduction is negligible ($\sigma_e \approx 0$) by solving Eqs. (4-2),(4-4) and (4-5). This solution is given as

$$\frac{r_e}{r_{e,0}} = \left[1 + \frac{2}{R_e} \frac{i_0 x}{i L} \right]^{-1/2}$$

(4-22)

$$\frac{f - f_0}{f_0} = \frac{UL}{m_e f_0} \left[\frac{x}{L} - \frac{R_e}{3} \left(\frac{i}{i_0} \right)^2 \left[\left(1 + \frac{2}{R_e} \frac{i_0 x}{i L} \right)^{3/2} - 1 \right] \right]$$

(4-23)

$$\frac{\Delta p}{e f_0^2 / L^2} = \frac{(p_L - p_0)}{e f_0^2 / L^2} = \frac{1}{2 f_0^2 / L^2} (E_L^2 - E_0^2)$$

(4-24)

where $r_{e,0}$ is the charge density at the emitter electrode and f_0 is the applied potential

to the emitter electrode. $R_e = \frac{Ue}{m_e r_{e,0} L}$ is a dimensionless number, $\frac{i}{i_0} = \frac{J.A}{r_{e,0} U A}$ is

dimensionless current ratio, and A is the area of each electrode. The boundary condition

of the potential field at the collector electrode, i.e. $f_L = 0$, leads to the determination of

the electrical current, i , passing through the electrodes.

Using the numerical modeling technique that was developed for this investigation, the governing equations of unipolar charge injection were solved. The computational domain was $x = 1$ unit by $y=0.5$ unit divided into $n_x = 50 \times n_y = 25$ Cartesian cells. The symmetrical boundary conditions at the top and bottom edges of the computational domain insured the one-dimensionality of the problem. A comparison between the analytical and numerical solutions for the charge density and the potential field along the axial direction is presented in Figure 4-3 and Figure 4-4, where the solutions were

obtained for $R_e = 1$ and $\frac{UL}{m_e f_0} = 1$. In Figure 4-5 the analytical and numerical solutions of

the dimensionless pressure head are compared as the dimensionless velocity,

$$R_e = \frac{Ue}{m_e r_{e,0} L}, \text{ varies.}$$

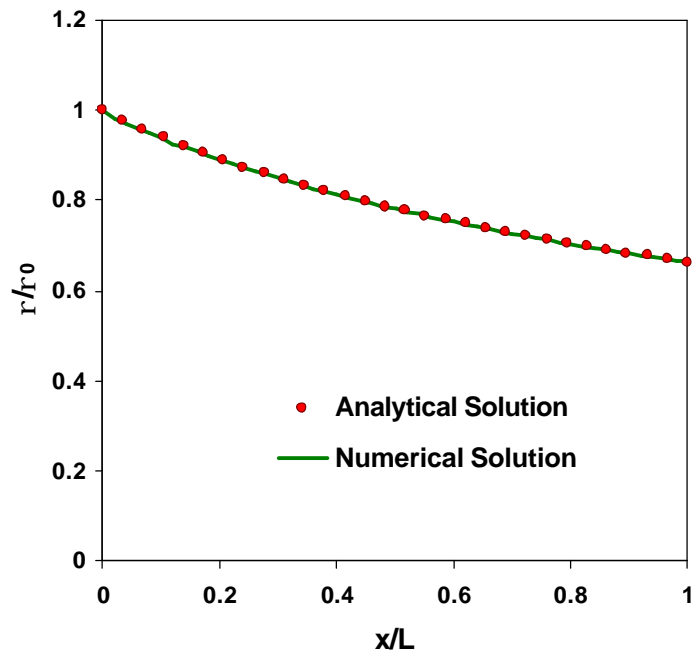


Figure 4-3 A comparison between numerical and analytical solutions of dimensionless charge density versus dimensionless axial length for one-dimensional unipolar ion-injection process

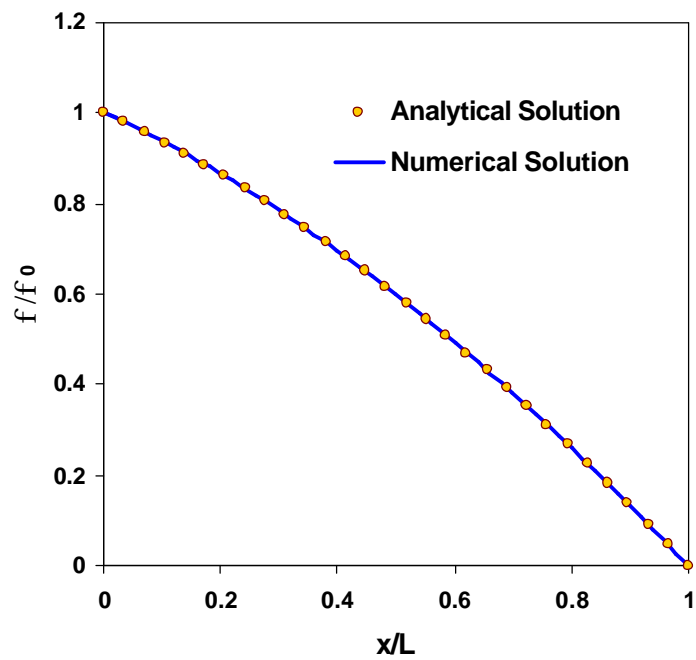


Figure 4-4 A comparison between numerical and analytical solutions of dimensionless potential field versus dimensionless axial length for one-dimensional unipolar ion-injection process

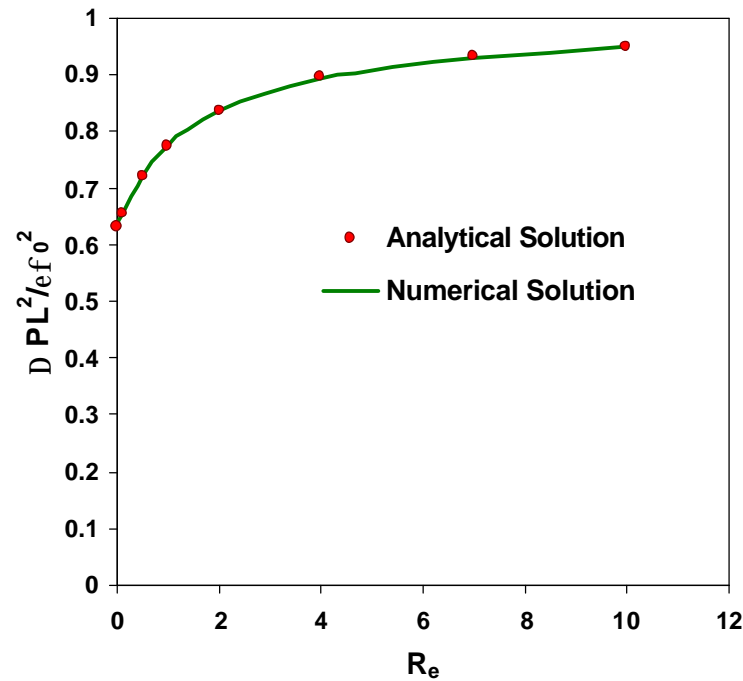


Figure 4-5 A comparison between numerical and analytical solutions of dimensionless pressure head versus dimensionless velocity for one-dimensional unipolar ion-injection process

As seen, in all cases a strong agreement between numerical and analytical solutions was obtained, which demonstrates the validity of the numerical modeling methodology.

B. Corona Wind in Wire-Plate Geometry

Consider a thin wire placed at a certain distance from a plate. If the wire is charged with a high voltage and the plate is grounded, an ion-injection process takes place at the high electric field region in the vicinity of the wire due to its small radius of curvature. While the injected ions travel from the wire (emitter electrode) toward the plate (collector electrode), they drag the neutral air molecules along with and generate a jet-type flow known as corona wind. The velocity of this jet flow depends on many parameters such as the applied voltage, the inter-electrode distance, and wire thickness.

Moghaddam *et al.* conducted an experimental study to measure the corona wind velocity using Laser Doppler Velocimetry (LDV)(Saidi, Moghaddam et al. 2002). The experiment was carried out with a prototypical wire-to-plate geometry (positive wire, grounded plate). In two series of experiments, the flow was seeded with $2.5\mu\text{m}$ dry glass microspheres and $0.5\mu\text{m}$ polystyrene nanospheres. The velocity profiles were obtained on different transverse axes. The test-section schematic is depicted in Figure 4-6.

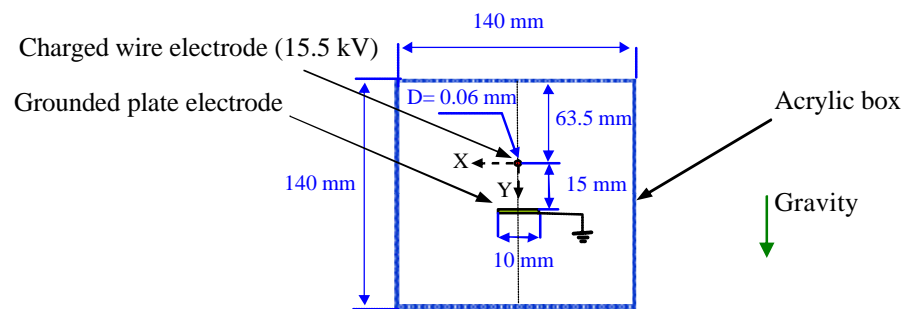


Figure 4-6 Wire-plate test-section (Saidi, Moghaddam et al. 2002)

To investigate the effects of the numerical simulation technique in modeling of EHD induced flow, the wire-plate problem was numerically simulated. Because the test section is symmetrical, only half of the test-section was considered as the computational domain, and a two-dimensional model was constructed. The potential on the wire and the plate were set to 15.5 kV and zero, respectively, to meet the actual experimental conditions. On the wire surface an autonomous ion injection was assumed. Thus, the charge density was considered uniform and constant. The value of the charge density on the wire surface was found by trial and error to be $\rho_e = 0.0008$ C/m³, so the numerically calculated electrical current matched the experimentally measured one ($i = 0.71 \times 10^{-3}$ A/m). In this modeling the effects of electrical conduction and convection were ignored (see Eq. (4-6)), since these terms are generally negligible for the EHD process in gases.

The computational domain was divided into 38000 triangular unstructured cells. In order to capture the steep variation of the electric field, a fairly dense grid in the vicinity of the wire electrode was generated. The computational cells are shown in Figure 4-7.

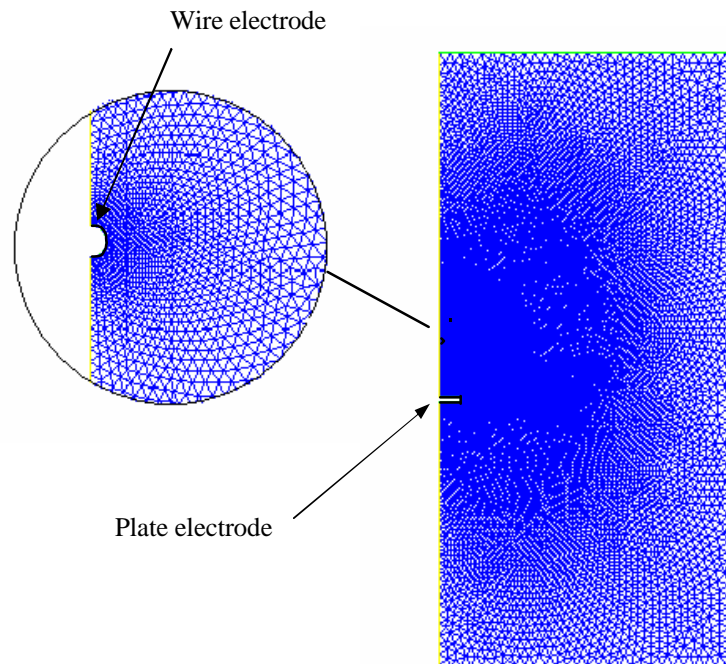


Figure 4-7 Unstructured computational mesh; The computational domain consisted of 38000 cells

The computation process was started by solving the charge density and the potential equations simultaneously. When the solution converged, the momentum equation was solved. For modeling of the convection term of the momentum equation, initially, the first order upwind (FOU) scheme for the laminar flow was used, and the solution converged. However, when second order upwind (SOU) scheme was used to increase the accuracy of the results, no convergence in solution was observed, and the residuals remained oscillatory. This issue was solved when the standard k- ϵ turbulence flow solver was used. This might be due to the artificial numerical diffusion associated

with the FOU scheme suppressing the flow fluctuations. It is difficult to justify the presence of the turbulent flow regime in this problem, since no critical Reynolds number for this type of EHD-driven flow has been reported previously. However, the flow can be compared with a lid-driven cavity flow. In the lid-driven cavity flow, the fluid is contained in a cavity where one of the walls moves with a specified velocity setting the fluid inside the cavity into motion. For this problem, a Reynolds number based on the moving wall velocity (i.e. the maximum velocity of the fluid) and the dimension of the cavity can be defined. If we assume that the corona wind inside the test section is equivalent to a lid-driven cavity flow where the maximum velocity of the corona jet (about 1.6 m/s) is equal to the moving wall velocity and the distance between the plate and the upper surface of the test section (about 78.5 mm) is equal to the cavity size, then the corresponding Reynolds number will be about 7900 which is relatively high. According to Poliashenko and Aidun (Poliashenko and Aidun 1995) for $Re > 7000$ the cavity flow becomes unstable. Although this does not necessarily mean that the flow is fully turbulent, it can explain the instability observed in the numerical modeling as the flow can be in a transitional regime. The use of turbulent model can be justified with the fact that no numerical scheme for the modeling transitional regime is provided in Fluent. Therefore, the results of laminar and turbulent modeling can be considered as two extreme cases and the actual flow regime might fall in between of these two cases. The results of pressure and velocity distributions for laminar flow with FOU scheme are presented in Figure 4-8 and Figure 4-9.

A comparison between experimental and numerical velocity profiles is presented in Figure 4-10, Figure 4-11, and Figure 4-12. As seen there, a clear difference between

experimental results with 2.5 μm and 0.5 μm seeding particles exists under the wire. According to Moghaddam *et al.*, this is because the seeding particles absorb electrical charge as they travel in ionized field, which leads to a slip between the seeding particles and fluid flow. Two processes, diffusion and field charging, contribute to particle charging. Moghaddam *et al.* studied the size effect on the particle charging process. Their study showed that charging the particles depends on their size: as particle size decreases, so does its acquired charge. According to their estimation, the maximum slip velocity of the 0.5 μm particles may not be greater than 0.25 m/s. A comparison between numerical and experimental results shows that the numerical simulation predicts a higher velocity above and a lower velocity below the wire. An integration of the area under the velocity profiles 8 mm below the wire shows that while the computational volumetric flow rate per unit length is about 26.6 m^2/s for the second order upwind turbulent scheme, the experimental volumetric flow rate per unit length is about 20.7 m^2/s for 0.5 μm seeding particles and 31.3 m^2/s for 2.5 μm seeding particles. Moreover, the generated wake behind the wire is more pronounced in the numerical result than it is in the experimental measurements (see also Figure 4-9). Moving away from the vertical axis of symmetry, the numerical calculated velocity diminishes more slowly than the measured one. This might be due to a larger domain of influence for the EHD force predicted by numerical simulation than the reality. Overall, experimental results showed a higher EHD force around the axis of symmetry for both 2 mm above and 8 mm below the wire. Notice that the effect of the EHD body force is to decelerate and accelerate the air flow above and below the wire, respectively. There are several factors that might have resulted in the difference between the experimental and numerical results. First, the effect of an ionized

field on charging of $0.5 \mu\text{m}$ seeding particles is uncertain, despite Moghaddam's *et al.* argument. The seeding particles may absorb more charge than calculated due to their recirculation motion inside the enclosure. Moreover, the uncertainty of the measurement also incorporates in this difference. Their results showed a standard deviation of seeding particle velocity in the range of $\pm 0.25\text{-}0.4$ m/s below the wire electrode. Secondly, in numerical modeling, a uniform distribution of the charge density on the electrode surface was assumed, while in reality the charges might be more concentrated on the wire surface points around the axis of symmetry. In addition, we should notice that the numerical simulation is based on a 2-D model. However, the actual air flow might be a 3-D flow considering a fairly short length of the wire (75 mm). The corona wind generates a low pressure zone around the wire. Therefore, an axial flow in z-direction might be generated. This can explain why the measured velocity above the wire is less than the numerical modeling velocity. In this case, the corona jet flow under the wire is supplied by two flows: the perpendicular flow above the wire (in y-direction) and axial flow (in z-direction). The numerical model does not consider the axial flow. Therefore, it predicts a higher velocity above the wire. Notice that the numerical simulation of 3-D model is not practical because a very large number of computational cells are needed. We should bear in mind that the EHD phenomenon is very complex process involving many different parameters, which may make a numerical model essentially very challenging.

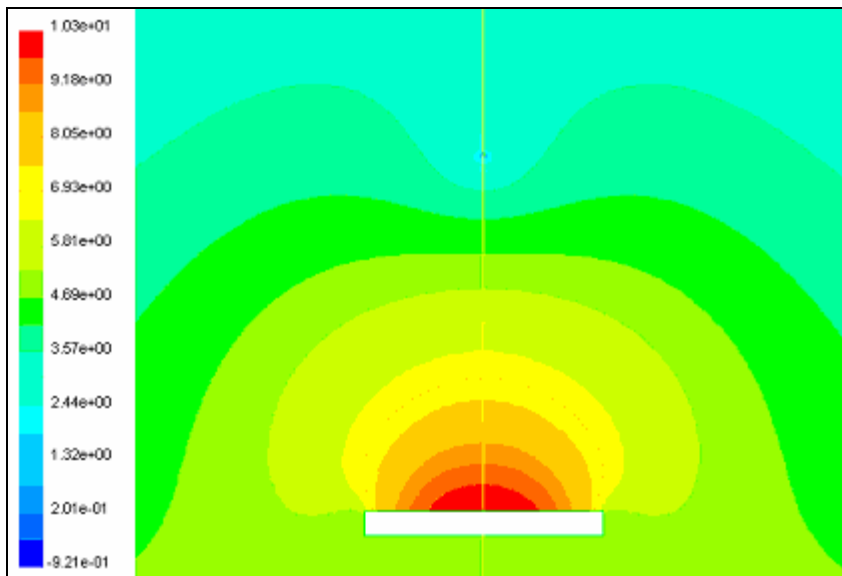


Figure 4-8 Pressure distribution in vicinity of wire and plate electrodes

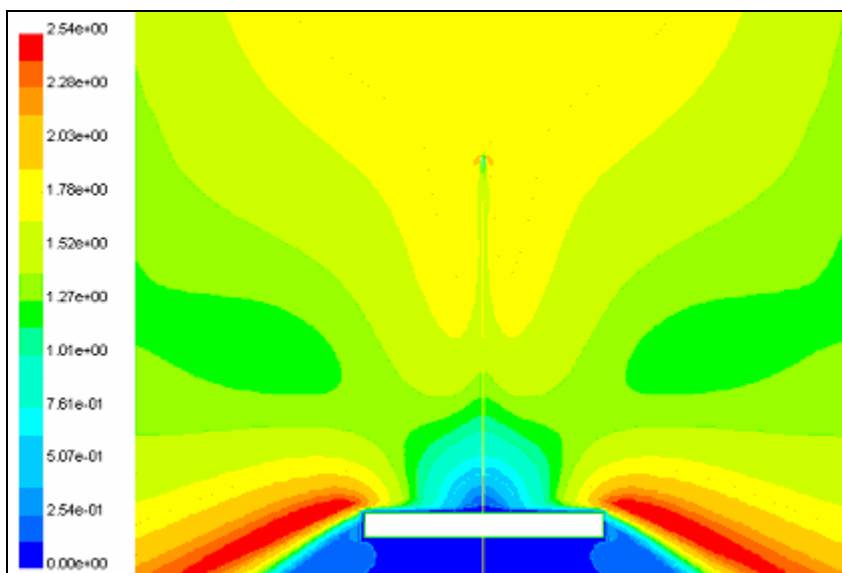


Figure 4-9 Velocity magnitude in vicinity of wire and plate electrodes

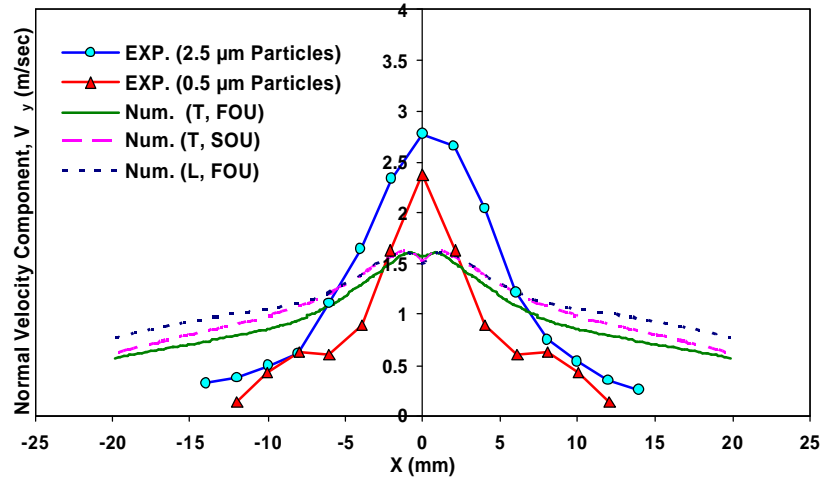


Figure 4-10 Numerical and experimental velocity profiles on a horizontal axis 8 mm below the wire- T: turbulent model, L: laminar model, FOU: first order upwind scheme, SOU: second order upwind scheme

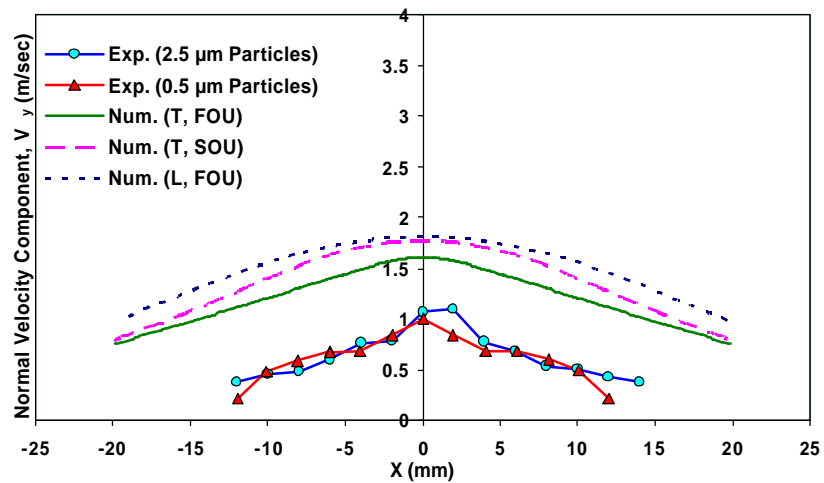


Figure 4-11 Numerical and experimental velocity profiles on a horizontal axis 2 mm above the wire- T: turbulent model, L: laminar model, FOU: first order upwind scheme, SOU: second order upwind scheme

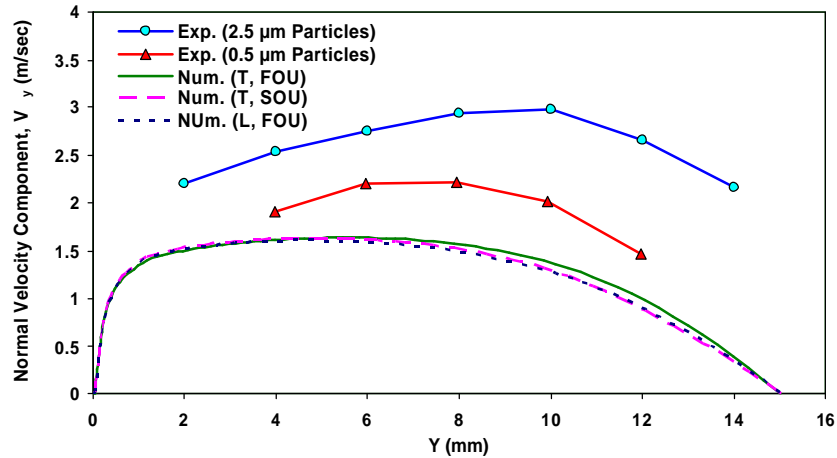


Figure 4-12 Numerical and experimental normal velocity component on the vertical axis of symmetry passing through the wire-T: turbulent model, L: laminar model, FOU: first order upwind scheme, SOU: second order upwind scheme

To investigate the independency of numerical results from the computational grid, the velocity profiles for two computational grids, dense and coarse grids, are presented in Figure 4-13. As seen here, the difference between the two velocity profiles is relatively small.

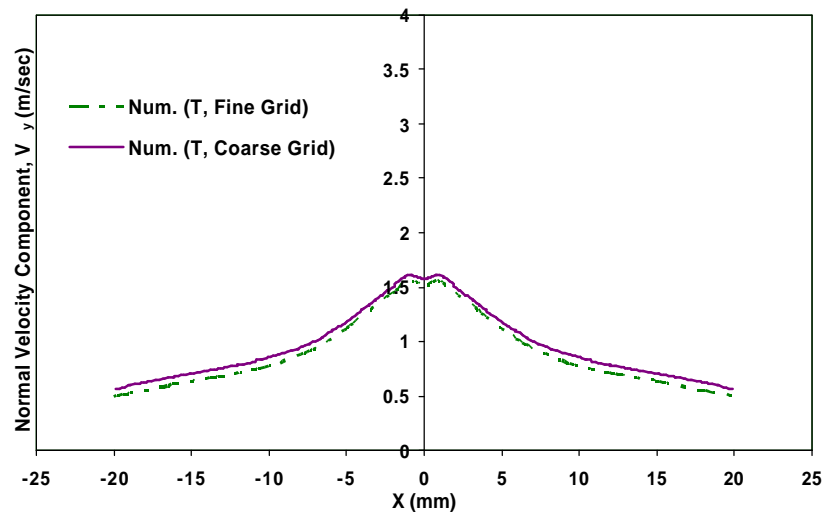


Figure 4-13 Numerical velocity profiles using the coarse grid with 38000 cells and fine grid with 57000 cells

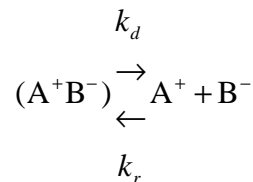
To evaluate the efficiency of the corona wind, Eq. (2-37) was numerically calculated. The integration was computed over the entire computational domain. It was found that the efficiency of the EHD process for the wire-plate geometry was about 0.5%. Moreover, the result shows that in the neighborhood of the wire the integrand given in Eq. (2-37) is negative above and positive below the wire. Therefore, covering the upper half of the wire with an electrical insulating layer can increase the efficiency of the process (up to 10%). Moghaddam et al. calculated the efficiency based on the kinetic energy induced by EHD mechanism in a control volume around the wire. Based on their technique, the efficiency of the process was estimated to be 0.4%, which is close to the value obtained numerically.

To conclude, while a difference between numerical and experimental results is visible, the numerical technique can conveniently serve as an excellent computational tool in assessment of EHD process efficiency and usefulness.

4.2.2 Dissociation-Injection Process

In the previous section a numerical methodology for modeling the ion-injection process with ohmic conduction was presented. In that model it was assumed that the conduction process was ohmic, meaning that the current density due to conduction was proportional with the electric field intensity and the proportionality coefficient (σ_e) was constant. In practice, however, the conductivity coefficient can vary with a strong electric field. To consider the effect of electric field on the conduction process, the dissociation of ionic pairs must to be considered. The ionic pairs are cations and anions associated with electrostatic forces. These ions have their origin in the impurities that the liquid may contain. In the absence of electric fields, the rate of dissociation of the ionic pairs and the

rate of recombination of ions are identical. However, application of a strong electric field can change this scenario. In fact, the dissociation rate is strongly affected by the electric field and can increase many orders of magnitude when the electric field is applied. This dissociation-recombination reaction can be simply shown as



(4-25)

where (A^+B^-) represents neutral ionic pairs, while A^+ and B^- represent cations and anions, respectively. This equation shows that the free ions are continuously generated by the dissociation of ionic pairs and conversely, the ionic pairs are formed by the recombination of positive and negative ions. k_d and k_r are the dissociation and recombination coefficient, respectively. As explained, application of an electric field can shift this equation toward the dissociation of ionic pairs and generation of additional ions.

Thus, two mechanisms lead to ion generation inside a liquid: direct ion injection and ionic pair dissociation. Notice that it is assumed that the ion injection process is unipolar, which means that only positive or negative ions are directly injected. However, the dissociation process generates both positive and negative ions. For this reason, modeling of this process involves determining the concentration of both positive and negative ions. To explain the mechanism of the dissociation-injection process, consider two parallel electrodes placed inside a nonpolar liquid. If a potential difference is applied to these two electrodes, in the absence of injection process an electrical current flow will be established between the electrodes. If the conduction process is ohmic, the concentration of positive and negative ions at any point between electrodes will be

identical and the electric field will be constant. However, in practice, in the vicinity of the electrodes the concentration of the ions with the same polarity as the electrode diminishes while moving toward the electrode surface. This region around the electrode, in which the concentrations of positive and negative ions are not in balance, is called the heterocharge layer. In this layer the magnitude of the electric field will be higher than the outer region. Notice that in the absence of the charge injection, the overall numbers of positive and negative ions are identical. When the charge injection takes place, the balance between the number of positive and negative charges will no longer exist, and even outside the heterocharge layer the concentration of positive and negative ions may not be identical.

4.2.2.1 Governing Equations

The assumptions made to derive the governing equations and model the dissociation-injection process are as follows:

1. The model is three-dimensional.
2. Only electrophoretic (Coulombic) force is present.
3. Charge injection takes place only at the emitter electrode.
4. Both positive and negative charge carriers are present.
5. Diffusion of ions is neglected.
6. The mobility of ions is constant and independent of the electric field intensity.
7. The fluid flow is steady state and incompressible.

The governing equations for the dissociation-injection process were introduced in section 2.2.1.1. However, the entire governing equations are restated here for ease of discussion.

The conservation of mass, momentum, and energy for an incompressible fluid resulted in

$$\nabla \cdot \mathbf{u} = 0 \quad (4-26)$$

$$\rho(\mathbf{u} \cdot \nabla) \mathbf{u} = -\nabla p - \mu \nabla^2 \mathbf{u} + \rho \mathbf{g} - (\rho_e^+ - \rho_e^-) \nabla \phi \quad (4-27)$$

$$\mathbf{u} \cdot \nabla T = \nabla \cdot (\mathbf{a} \nabla T) + \frac{\mathbf{n}}{c_p} \mathbf{f} + \frac{(\mathbf{m}_e^+ \mathbf{r}_e^+ + \mathbf{m}_e^- \mathbf{r}_e^-)(\nabla \mathbf{f})^2}{r c_p} \quad (4-28)$$

The Poisson equation is given as

$$\epsilon \nabla^2 \mathbf{f} = -(\mathbf{r}_e^+ - \mathbf{r}_e^-) \quad (4-29)$$

The positive and negative charge conservation equations are

$$\frac{\partial \mathbf{r}_e^+}{\partial t} + \nabla \cdot \mathbf{J}^+ = k_d c - k_r \mathbf{r}_e^+ \mathbf{r}_e^- \quad (4-30)$$

$$\frac{\partial \mathbf{r}_e^-}{\partial t} + \nabla \cdot \mathbf{J}^- = k_d c - k_r \mathbf{r}_e^+ \mathbf{r}_e^- \quad (4-31)$$

where

$$\mathbf{J}^\pm = \pm \mathbf{m}_e^\pm \mathbf{r}_e^\pm \mathbf{E} + \mathbf{r}_e^\pm \mathbf{u} \quad (4-32)$$

and the total current density is given by

$$\mathbf{J} = \mathbf{J}^+ - \mathbf{J}^- \quad (4-33)$$

The relationship between current density and total current as given by Eq. (4-9) stands in this case as well. The rest of the parameters appearing in Eqs. (4-30) and (4-31) can be calculated based on other variables as their relationships are given in section 2.2.1.1.

Therefore, these governing equations form a set of six equations and six unknowns.

4.2.2.2 Boundary Conditions

Boundary conditions for Eqs. (4-26) to (4-29) are identical to those presented in section 4.2.1.2. For charge conservation equations, the boundary conditions on the emitter and collector electrodes are:

$$\mathbf{r}_e^+ = \frac{\mathbf{r}_e^0}{2bK_1(b)} \text{ and } \mathbf{n} \cdot \nabla \mathbf{r}_e^- = 0 \text{ on } S_{emitter} \quad (4-34)$$

$$\mathbf{n} \cdot \nabla \mathbf{r}_e^+ = 0 \text{ and } \mathbf{r}_e^- = 0 \text{ on } S_{collector} \quad (4-35)$$

(Pontiga and Castellanos 1996). Here it is assumed that the positive charges are injected from the emitter electrode into a nonpolar liquid (i.e. the emitter electrode is an anode). Variable b is defined in Eq. (2-17) and the parameter \mathbf{r}_e^0 represents the charge density on the emitter electrode as the electric field approaches zero. The value of this parameter is not known. However, Pontiga and Castellanos (Pontiga and Castellanos 1996) argue that since the injected ions originate from the ionic pairs absorbed on the metal, the injected charge density can be expected to be related in some way to the residual conductivity of the liquid. According to them, the dimensionless number

$$A = \frac{\mathbf{r}_e^0}{\mathbf{s}_e / (\mathbf{m}_e^+ + \mathbf{m}_e^-)} \quad (4-36)$$

is of an order of unity in most of dielectric liquids.

On the other boundaries, rather than the emitter and collector electrodes, it is usually safe to apply a Neumann boundary condition.

4.2.2.3 Discretisation, Numerical Solution Algorithm, and Implementation of the Solution Technique with the Fluent Solver

The discretisation procedure of governing equations is similar to the unipolar charge injection with ohmic conduction case, which was presented in section 4.2.1.3 and will not be repeated here. The major difference here is that the number of equations is six now compared to the five in previous case. In addition, unlike the previous case, the charge conservation equations for the positive and negative charges involve source terms which must be discretised as well.

The solution algorithm and its implementation technique using the Fluent solver are also similar to the previous case as presented in sections 4.2.1.4 and 4.2.1.5. Therefore, the same methodology can be used. However, it should be noticed that in the current case charge density of both polarities should be calculated. Moreover, the implementation of the charge injection boundary conditions is more involved since it depends on the electric field as well.

4.2.2.4 Verification of Numerical Modeling Technique

To verify the validity of the developed numerical method in modeling the injection-dissociation process, a sample problem was solved and the result was compared with another numerical result reported in the literature. This problem consisted of two parallel flat electrodes placed inside a nonpolar liquid. A high electric potential was applied to one of the electrode (emitter) while the other electrode (collector) was

grounded. The problem was to some extent similar to one-dimensional ion-injection pumping problem presented in section 4.2.1.6. However, there are some distinct differences between these two problems. In current problem not only the injection, but also the dissociation process was taken into account. Furthermore, it was assumed that the density of injected charges from the emitter electrode was a function of the electric field as given by Eq. (4-34); while, in the previous problem, an autonomous ion injection was assumed where the charge density on the emitter electrode remained constant.

Pontiga and Castellanos (Pontiga and Castellanos 1996) obtained a numerical solution for this problem assuming that the effect of the convective term due to liquid velocity in the generated current density is negligible. However, their study focused only on obtaining the current- voltage relation, and no effort was paid to solve the Navier-Stokes equation and model the influence of injection-dissociation process on the fluid flow. According to their study, in the absence of any fluid flow, the problem can be completely formulated by using four dimensionless numbers, given as

$$\mathbf{g} = \frac{m_e^+}{m_e^-}, \quad C_0 = \frac{sL^2}{(m_e^+ + m_e^-)\mathbf{f}}, \quad \bar{b} = \left[\frac{e_0^3 \mathbf{f}}{16pe k^2 T^2 L} \right]^{1/2}, \quad A = \frac{\mathbf{r}_e^0}{s_e / (m_e^+ + m_e^-)} \quad (4-37)$$

In the current modeling effort the same problem is solved. The computational domain consists of a two-dimensional region divided by 50×10 computational cells. The value of the parameters are selected such that the dimensionless numbers are $\mathbf{g} = 1$, $C_0 \bar{b}^2 = 10^{-2}$ and $A = 1$. The computational process starts with solving the potential field in the absence of any charges. When a converged result is obtained, the positive and negative charge conservation equations are solved simultaneously with the potential

equation. The computational iteration terminates when the maximum residual drops off at least six orders of magnitude.

The total current density flowing between electrodes can be calculated from Eq. (4-33), which has a constant value at any point between electrodes. On the emitter electrode, the total current can be split into an injected current, j_i , and dissociation current, j_d , which are given as

$$j_i = \mathbf{m}_e^+ \mathbf{r}_e^+(0)E(0), \quad j_d = \mathbf{m}_e^- \mathbf{r}_e^-(0)E(0) \quad (4-38)$$

However, due to the recombination between the injected charge carriers and ions generated by dissociation, these two parts do not remain constant between the two electrodes.

A comparison between the current density obtained and the numerical result reported by Pontiga and Castellanos (Pontiga and Castellanos 1996) is presented in Figure 4-14. Here the current density is made dimensionless using the parameter $j_{sat} = \sigma_e / \epsilon (\mu_e^+ + \mu_e^-)$, which corresponds to the saturation current when no injection and enhanced dissociation is present. Notice that since j_{sat} is independent of the voltage and $C_0^{-1} \propto \phi$, a direct comparison of the result presented in Figure 4-14 with the current-voltage characteristic obtained in real experience can be made. As seen, overall a good agreement between the two computational results is obtained. Nevertheless, a relatively small deviation between the calculated dissociation current results is observed. This might be due to the imprecise technique used to extract the Pontiga and Castellanos data from their published paper. Notice that for the current modeling each data point is obtained by calculation of the current density for a specific voltage.

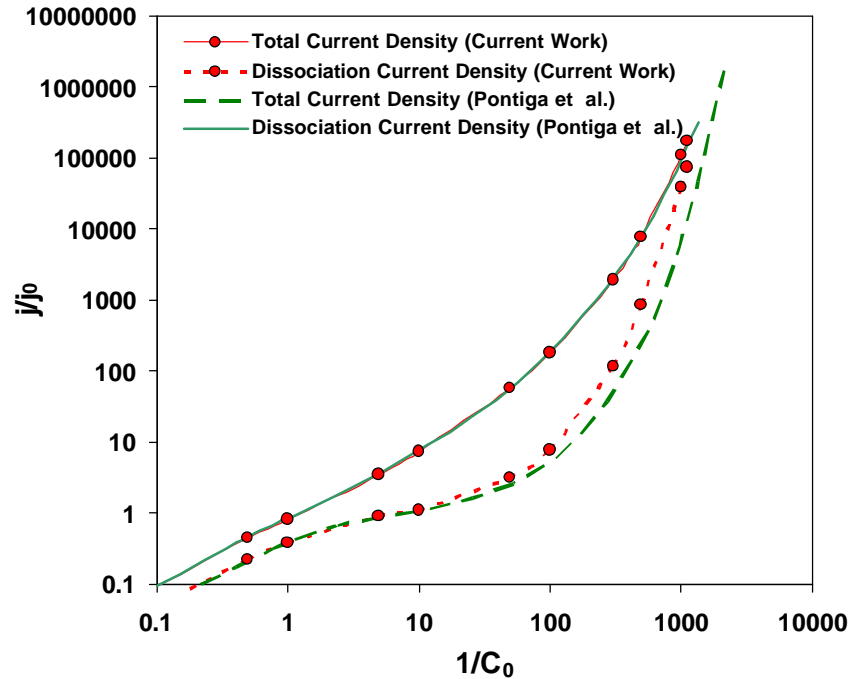


Figure 4-14 A comparison between result of current model and Pontiga et al. numerical result for total current density (solid line) and dissociation current density (dashed line) as a function of C_0^{-1} for $C_0 \bar{b}^2 = 10^{-2}$ and $A = 1$

As seen, at moderate voltage, the dissociation current makes up a relatively small portion of the total current. In fact, in this region the injection is the dominant process. However, at low voltages (ohmic region) and very high voltage, the dissociation current forms a considerable amount of the total current. On the other hand, unlike the injection process, the dissociation process does not lead to a pumping effect for a parallel-electrode geometry. Therefore, it is expected that the pumping action will be more efficient in middle range voltages. The pumping action for the injection and dissociation processes will be reviewed in next chapters.

4.3 Summary

In this chapter the developed numerical modeling procedure for the electrohydrodynamic process was reviewed in detail. In this modeling it was assumed

that the driving force was the Coulomb force only and the fluid flow regime was single-phase. The electrohydrodynamic problems were divided into two classes: unipolar charge injection with ohmic conduction and dissociation-injection processes. For each class of problems, the governing equations, the solution methodology, and the verification process were reviewed. The verification results showed that the developed numerical modeling method can serve as a reliable tool to study electrohydrodynamic phenomena.

CHAPTER 5: EHD MESOPUMP DESIGN AND FABRICATION

5.1 Introduction

The objective of this chapter is to introduce the design of an EHD mesopump with micro fabricated electrodes and to review its fabrication methodology. First, the general design requirements of an EHD ion-injection pump will be examined, and a preliminary design will be introduced. Next, a number of issues pertaining to this preliminary design will be discussed, and a solution will be proposed involving microfabrication techniques. Finally, a mesopump design with an appropriate scheme for microfabrication will be introduced, and its process flow will be reviewed. We will also review the pump packaging technique along side.

5.2 Requirements and the Preliminary Design

As discussed in the previous chapters, the operating principle of an ion-injection pump is based on the generation of ions in the vicinity of an electrode called an emitter electrode, acceleration of these ions along the electric field, and eventually their neutralization at an electrode of opposite polarity located downstream, called a collector electrode. Because of momentum exchange between the ions and fluid neutral molecules, the flow of ions “drags” the bulk liquid in the forward direction, thereby producing the pumping effect. The basic requirement for enhancement of the ion-injection process is a high intensity electric field at the emitter electrode. A localized high intensity electric

field can be achieved by designing an emitter electrode that contains several sharp points. The more sharp points that exist, the greater the ion generation. This fact is schematically illustrated in Figure 5-1. As seen there, an increase in the number of sharp points results in an increase in more electric field spots.

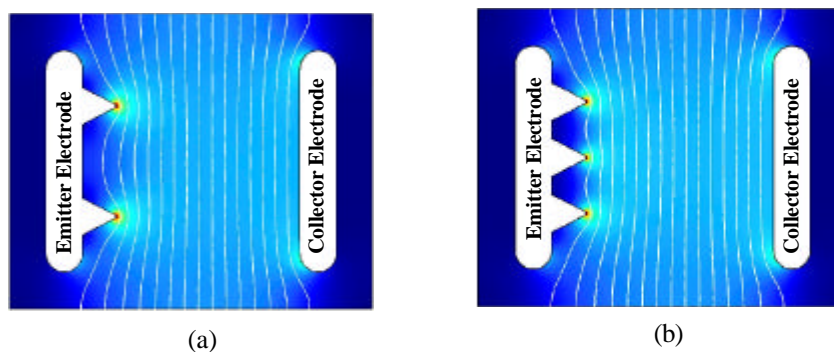


Figure 5-1 Increasing the number of sharp points on the emitter electrode enhances ion-injection process.

The arrangement of these sharp points, which act as ion generation/injection locations with respect to the collector electrode, is important in the performance of the ion-injection pump. If the points are positioned at various distances from the collector electrode, the intensity of electric field at the vicinity of the sharp point will also vary, in that those sharp points that are closer to the collector electrode will inject ions more effectively than the rest. In other words, not all the sharp points participate evenly in the ion-injection process. In addition, a complete electrical breakdown (spark-over) will not take place simultaneously at all these sharp points. As the voltage between the emitter and collector electrodes is increased, the sharp points on the emitter that are closer to the collector electrode will reach the breakdown electric field intensity earlier than the remaining sharp points, and as a result an early spark inside the liquid initiates from these points, while the remaining sharp points may not participate. Therefore, the best arrangement of sharp points of the emitter is the one for which the distances to the

collector electrode are nearly identical so that all the sharp points can participate in the ion generation equally and uniformly. Henceforth we will call these sharp points injection points. These situations are illustrated in Figure 5-2. Case (a) represents the situation where injection points are positioned at equal distance from the collector so that the localized electric field intensities at their tips are identical. In case (b), since the distances of injection points from the collector electrode are not equal, the electric field intensities at the tips are uneven.

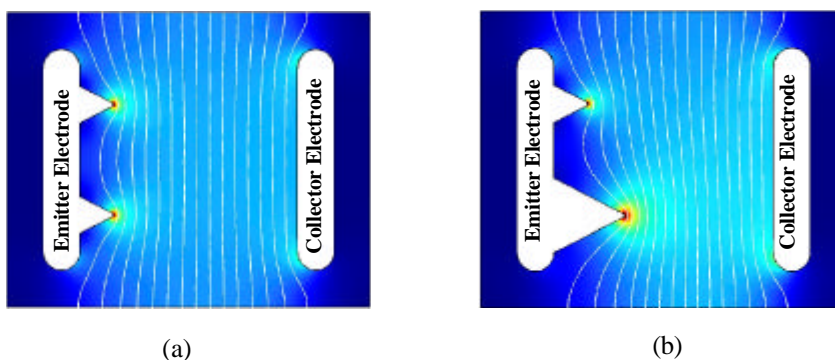


Figure 5-2 The electric intensity at the sharp points depends on their distances from the collector electrode. The electric field intensifies as the emitter sharp points get closer to the collector electrode.

Within this array of injection points, the distance from one injection point to its adjacent point is also a fundamental factor in determining ion generation efficiency. As this distance decreases, the localized field intensity will be reduced, which, in turn, lowers the ion injection rate. For example, as depicted in Figure 5-1, the maximum localized electric field intensity in case (b) is less than case (a). On the other hand, increasing the distance among the injecting-points may result in a larger dimension of the pump.

In order to enhance the performance of pumping, it is important that the EHD force is uniformly applied axially across the entire cross-section of the liquid channel. If, for example, this force is only applied to the peripheral region close to the edges of the

flow channel, as the back pressure increases a recirculation flow inside the pump will be generated, which dissipates energy and reduces pump performance. Therefore, in an ideal situation the sources of ion generation should be distributed uniformly across the cross-section of the flow channel. Figure 5-3 illustrates these circumstances. In case (a) the injection points are positioned compactly. Thus, the effective Coulombic drag force is approximately uniform throughout the inter-electrode gap. However, in case (b), since the injection points are positioned sparsely, a non-uniform force will be introduced on the liquid medium that can result in a recirculation motion, as depicted.

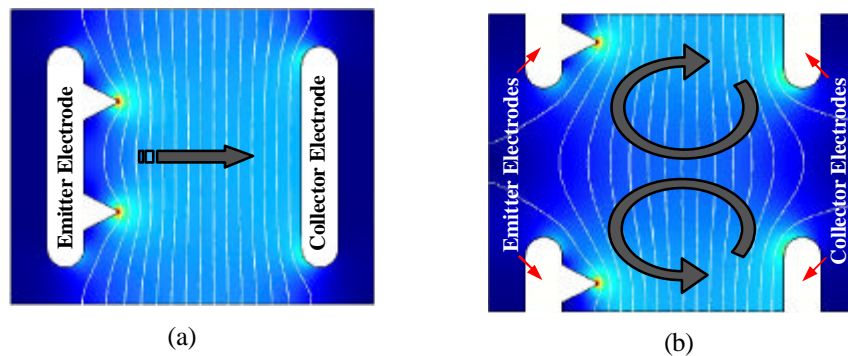


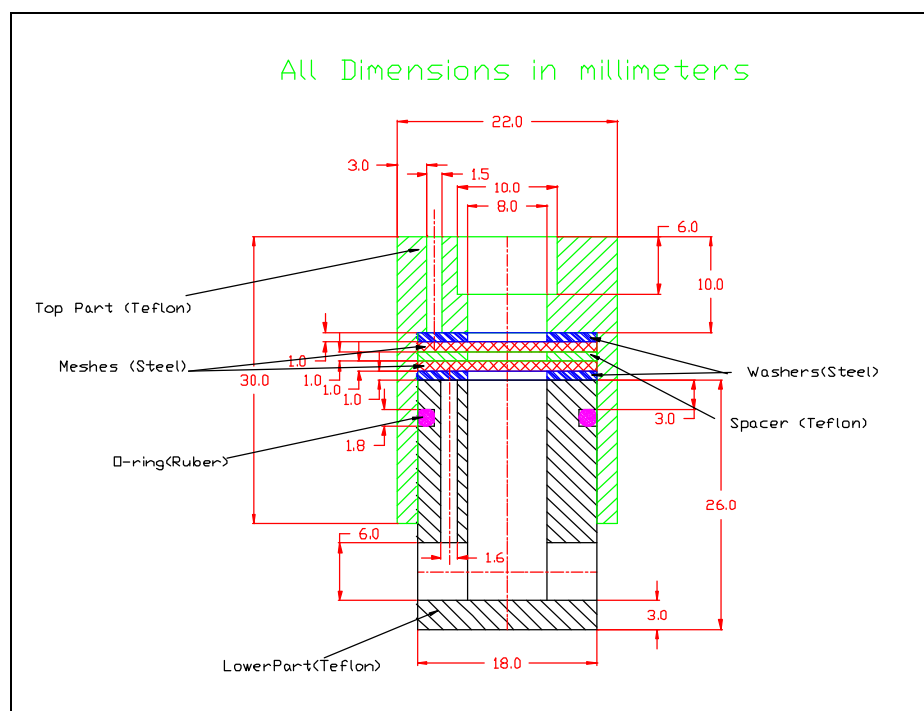
Figure 5-3 If the ion-injection points are positioned far away from each other, the electric force will not be uniform. This may result in a recirculation motion of the liquid.

Internal pressure drop is also important in the design of miniaturized pumps. If the pump has a very constricted channel, the internal pressure loss of the pump will be considerable. As a result, a significant amount of the generated pressure head will be spent in compensating for this internal pressure loss, and the pump may not deliver a useful flow rate.

5.3 A Preliminary Ion-Injection Pump Design

In view of the requirements discussed in the previous section, a preliminary EHD ion-injection pump was designed. In this design of the ion-injection pump, the emitter

and collector electrodes were in the form of stainless steel wire mesh. The use of wire mesh as an electrode has been reported by previous researchers (Bologa, Kozhevnikov et al. 2000), and (Bryan and Seyed-Yagoobi 1992). The objective of this preliminary design of an ion-injection pump was to investigate the advantages and drawbacks of using wire mesh as electrodes. A schematic drawing and 3-D model of the pump is depicted in Figure 5-4. As shown there, the pump consists of two circles of wire mesh that act as electrodes and are separated by a spacer to maintain a uniform gap between them. The body of the pump is composed of two pieces, the lower and upper, that are made of Teflon[®].



(a)

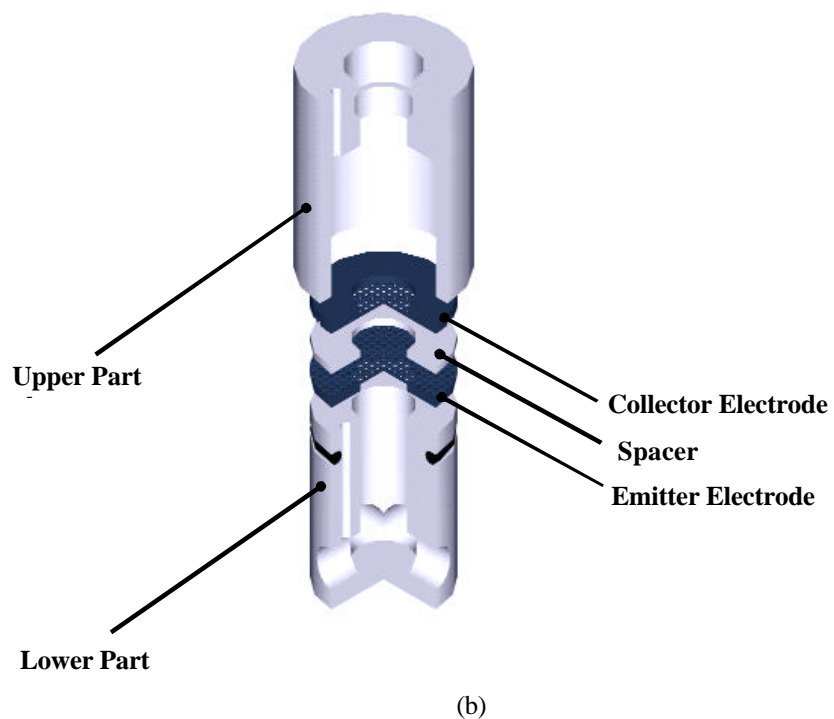


Figure 5-4 A preliminary EHD ion-injection pump, (a) dimensional drawing, (b) 3D model

A photograph of the manufactured components is depicted in Figure 5-5.

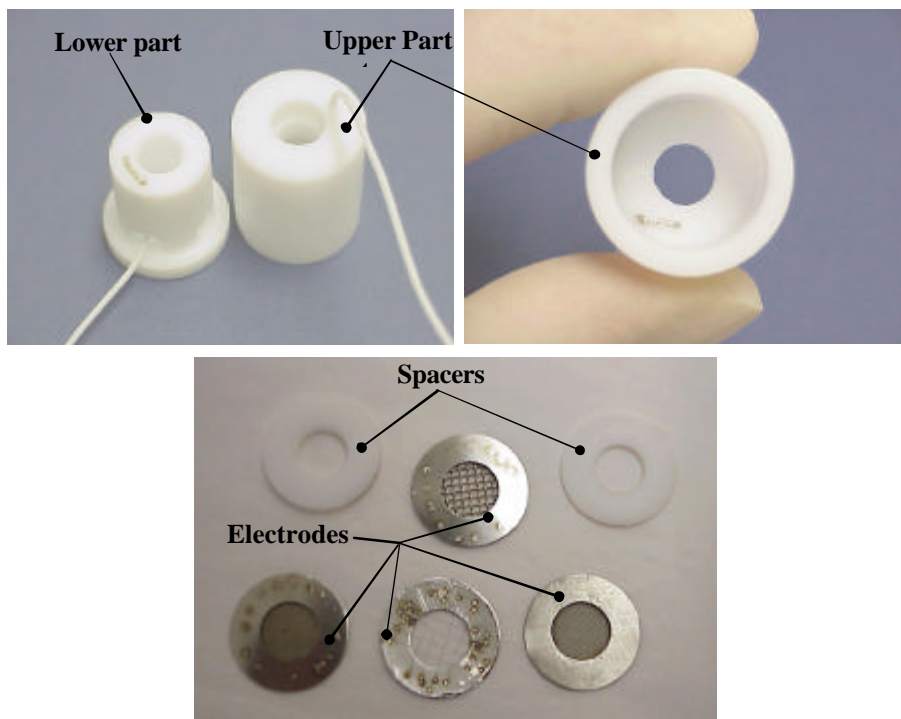


Figure 5-5 Fabricated components of an ion-injection EHD pump (preliminary design)

As a high voltage current is established between electrodes, a stream of ions moving from the emitter electrode to the collector electrode is generated. As a result of the ions' momentum transfer to the liquid medium, a pumping action is induced.

An experimental test was conducted to measure the static pressure generated. The working liquid was HFE-7100[®] and the spacer thickness was 3 mm (see Chapter 6 for a description of HFE-7100[®] characteristics). Figure 5-6 shows the generated static pressure head when the collector electrode was grounded and an electrical potential of 30 kV with negative polarity was applied to the emitter electrode. In this test the pump was entirely submerged in the liquid, and a vertical glass tube was connected to the outlet port of the pump. The difference of fluid levels inside and outside this tube formed a measure of the static pressure head of the pump. This experiment demonstrates that wire mesh structures can be successfully used as electrodes. However, a number of difficulties were noted. For example, the required electrical potential was quite high and the pump's performance was non-repeatable. Moreover, the wire mesh structure did not fulfill some of the requirements listed in previous sections. This will be discussed further in the next section, where the advantages of using microfabrication techniques are discussed.

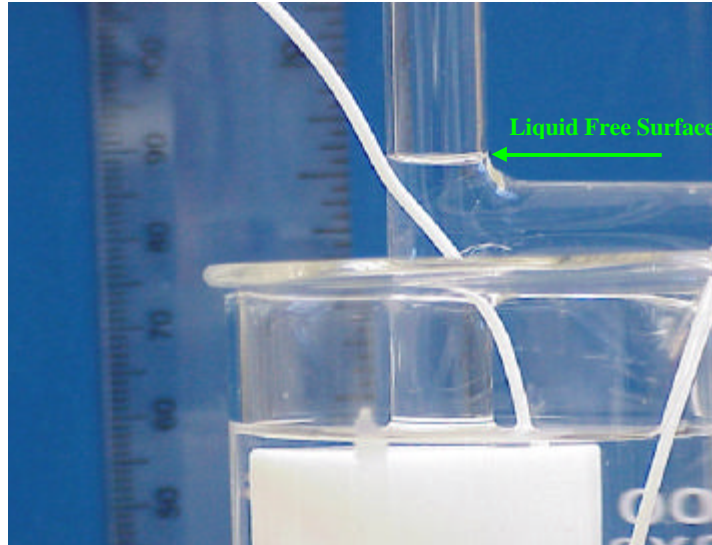


Figure 5-6 Static pressure test on the preliminary EHD pump design; the column height of HFE 7100 liquid represents the static pressure generated.

5.4 Why the Microfabrication Technique for Electrodes?

As pointed out in the previous section, the operational electrical potential for the preliminary EHD pump design was relatively high. To reduce this electrical potential, it is necessary to decrease the gap between the emitter and collector electrodes. This is because the ion-injection process depends on the electric field intensity, which is directly proportional to the electrical potential difference and inversely proportional to the gap between the electrodes. The electric field intensity is held constant if the gap and the applied electrical potential are decreased simultaneously at the same rate.

However, decreasing the gap distance between electrodes introduces new challenges. As explained in section 5.2, if the injection points on the emitter electrode are not positioned at the same distance from collector electrode, the pumping efficiency will decrease, and an early breakdown (spark) can occur. Such a phenomenon is least desirable. The possibility of sparking will increase as the distance between the electrodes decreases, since non-uniformities on the wire mesh act as uneven injection spots. Due to

the fabrication tolerances and production technology of metal wire mesh, control of these non-uniformities is not feasible. Furthermore, as the gap between electrodes decreases, the sharpness (i.e. curvature) of the injection points must increase as well to maintain a high enough localized electric field intensity. This requires that the diameter of wire in the mesh structure be sufficiently small. Such meshes are not commercially available.

Another disadvantage of the wire mesh electrode is associated with the injection of some ions in the opposite direction of the fluid flow. This phenomenon is illustrated in Figure 5-7. In this figure the wire-plate electrode geometry is shown. Due to injection of ions and Coulomb force, a net flow directed from left towards right is generated. Those streams of ions that emanate from the front side of the emitter wire facing the plate promote the flow of the fluid, while the ions emanating from the rear side of the wire locally undermine the flow by initially moving in the opposite direction. Of course, the net force will be from the left to the right.

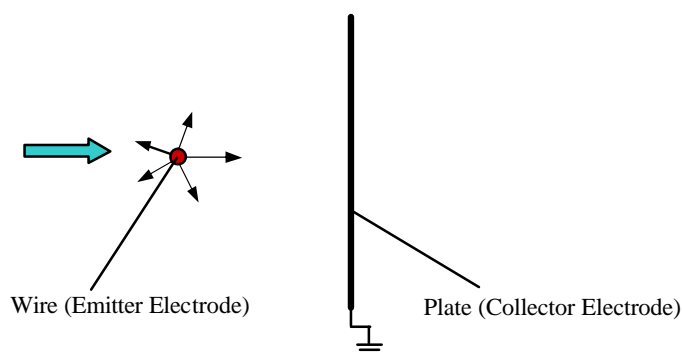


Figure 5-7 Direction of ion-injection process around a wire electrode

Microfabrication techniques can address some of the major issues associated with using wire mesh structures as electrodes. Due to the remarkable tolerance levels of these techniques, the irregularities and imperfections can be minimized and the injection points can be positioned at equal distances from the collector electrodes. As a result, these

techniques allow us to decrease the inter-electrode gap without encountering early spark incidents. Moreover, these techniques provide us a larger degree of flexibility in dimensional design of the electrode geometry, allowing us to optimize the structure of the electrode. These techniques also offer the opportunity to decrease the radius of curvature of the injection points, which intensifies as the localized electric field promotes the ion injection process.

5.5 Mesopump Design

In the design of the mesopump and its fabrication process the objective is to incorporate the benefits that the mesh-structure electrode and microfabrication technology offer. As discussed earlier, the mesh-structure electrode provides a uniformly distributed driving force across the flow channel, with the injection spots equidistant from the collector electrode. The microfabrication technology allows us to scale down the pump size and the distance between the electrodes while the preserving electrode uniformity and avoiding unevenness.

The mesopump consists of a number of components, the most important of which is the set of electrodes. In this design each electrode is a perforated thin film of gold deposited on a silicon wafer (substrate). The holes are square and are separated by a thin web of ribs. Standard silicon micromachining, a common technique in fabrication of MEMS devices, was used to construct the desired structure. This fabrication technique provides a great degree of flexibility in its application, which is easily performed in the university research labs. Hence the technique can be optimized to provide us with the best procedure for fabricating our desired structure. In Figure 5-8 a schematic of the electrode is shown. The shaded region illustrates the gold film deposited on a silicon

base wafer where the wet etching technique was used to make a two-dimensional array of square perforations. The electrical connection was made by attaching a voltage source to the bond pad leading away from the electrode web. Dimensions 'd' and 't' in this figure represent edge-to-edge distance and web thickness, respectively. The five different designs fabricated had measurements of (75, 405), (75, 700), (75, 2444), (150, 625) and (150, 2369), where numbers inside the parentheses refer to dimensions t and d, respectively, in micrometers. These dimensions are selected based on our previous tests on preliminary design of EHD pump. From different mesh electrode structures that were used (see Figure 5-5) it was concluded that the best performance was obtained when the emitter has a larger perforation size and thinner wire while the collector has perforations of a smaller size. Moreover, the web width (t) was selected based on the minimum size that was safely achievable by using microfabrication.

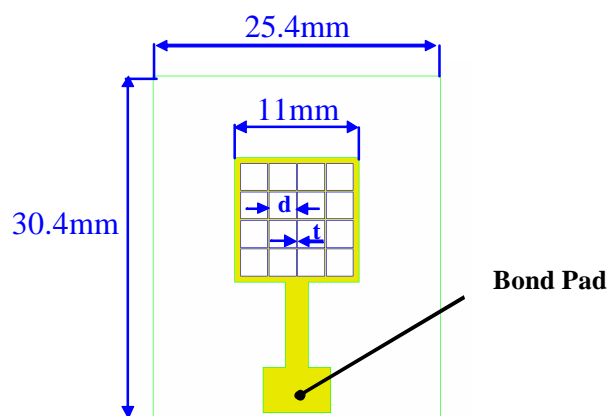


Figure 5-8 Schematic diagram of electrodes of mesopump

It is important to note that the gold film cannot be directly deposited on the silicon wafer because of lack of adhesion. The solution to this problem is to deposit an intermediate layer that will promote gold-silicon adhesion strength. There are also other

layers that serve other purposes as discussed below. A schematic cross-section of the electrode is shown in Figure 5-9. The layers consist of the following:

- Silicon wafer (525 μm thick): provides structural platform for the electrode;
- Silicon oxide film (1.5 μm thick): acts as a dielectric layer and insulates silicon from high voltage applied to the gold electrode;
- Silicon nitride film (0.3 μm thick): acts as a mask during wet etching process and provides an dielectric insulation base for chromium and gold films;
- Chromium film (150 \AA thick): provides sufficient adhesion between gold and silicon nitride films;
- Gold film (0.35 μm thick): acts as the pump electrode.

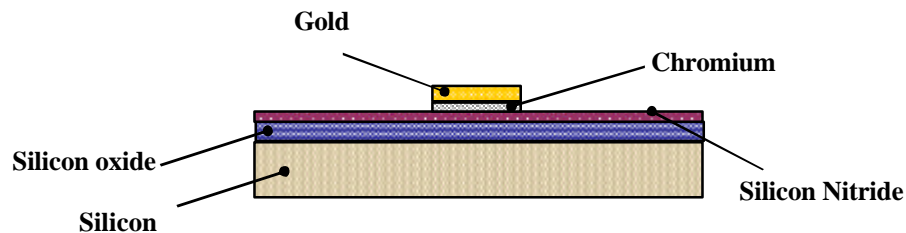


Figure 5-9 Various layers deposited on the silicon wafer (not to scale)

Notice that unlike the previous wire-mesh electrode, this electrode design does not suffer from the backward ion injection phenomenon discussed in section 5.4. This is because the gold layer is exposed only on the front side and is insulated from the back side by insulating layers, i.e. silicon nitride and oxide.

The electrodes are separated using a thin layer of Pyrex 7740 (250 μm thick) acting as a spacer. A schematic sketch of the spacer is depicted in Figure 5-10. Pyrex has a very high dielectric strength that makes it a suitable choice for separating the electrodes.

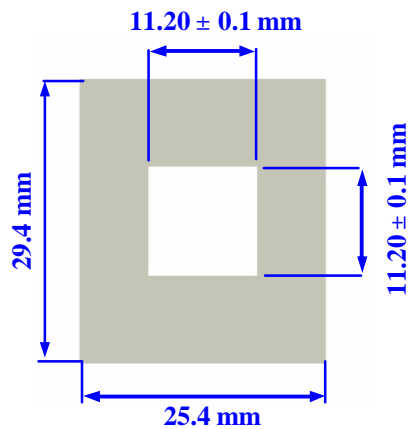


Figure 5-10 Schematic sketch of Pyrex spacer

The electrodes and spacer combination are encased in a housing that is machined from an acrylic block, as shown in Figure 5-11. This housing possesses a fluid interconnector at either end for the inlet and outlet of the flow.

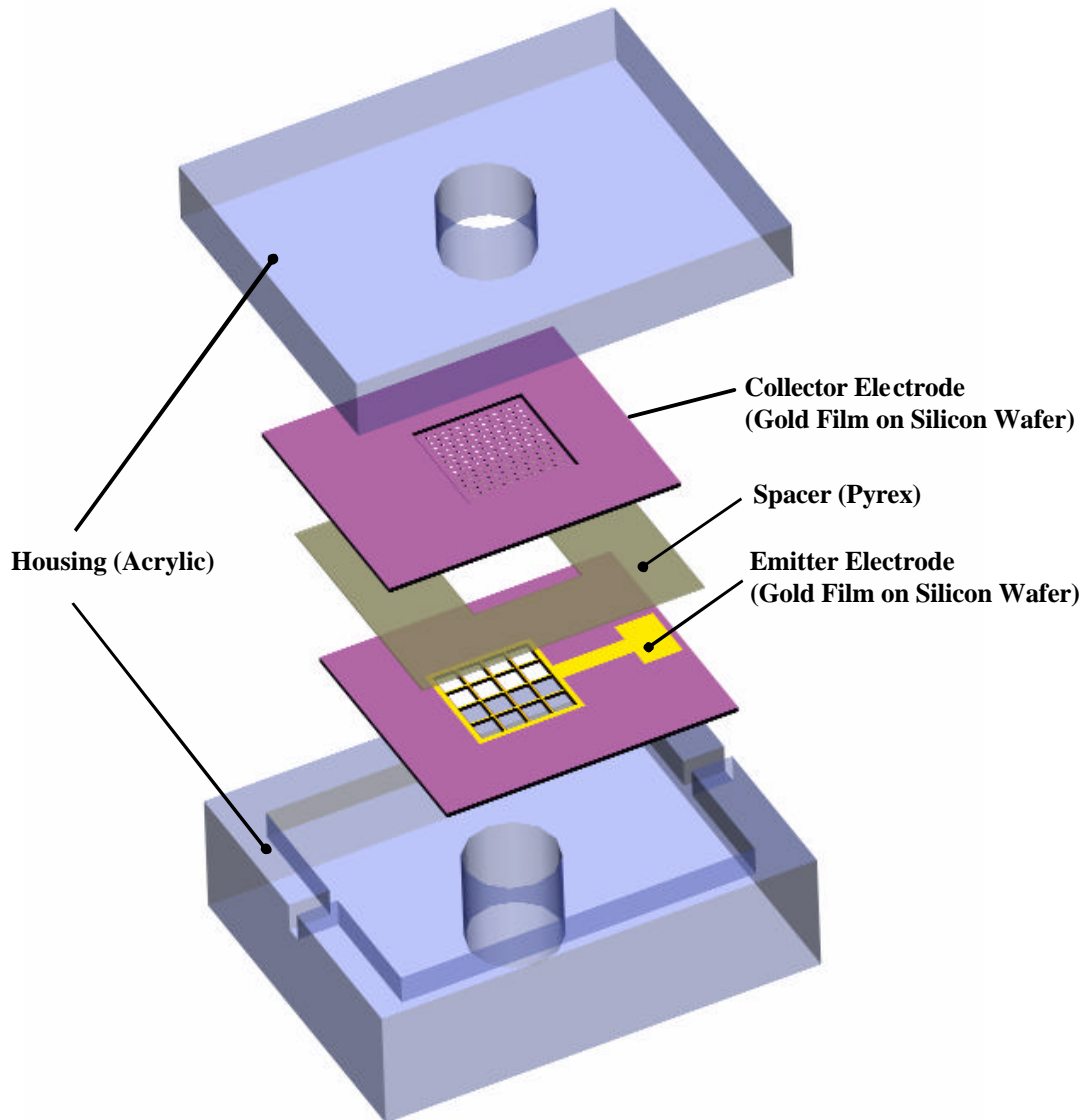


Figure 5-11 Schematic diagram of Mesopump components

5.6 Microfabrication and Packaging Processes

In this section the microfabrication manufacturing process for the electrodes will be reviewed in detail. As explained above, the electrode structure is an array of perforations where the silicon wafer serves as a structural platform or substrate for the gold film. To microfabricate such a structure, the bulk silicon and the deposited films must be etched

away. In this etching process, the objective is to selectively remove material using a photoresist pattern that acts as an etch mask. For a successful etch, there must be sufficient etch selectivity of the material being etched against the masking material. Based on the directional nature of the etching process, etchants can be typically divided into two major categories, namely isotropic and anisotropic. Isotropic etchant etches uniformly in all directions, resulting in rounded cross-sectional features (see Madou, 2002)). In contrast, an anisotropic etchant etches in primarily one direction into the substrate, resulting in trenches or cavities surrounded by flat and well-defined surfaces. The chosen direction of the etch for this category of etchants is determined from the crystalline structure of the substrate.

Also, according to the nature of the medium, etchants can be classified into two other groups, dry and wet etchants. Dry etching covers a family of methods by which a solid surface is etched in the gas or vapor phase, physically by ion bombardment, chemically by a chemical reaction through a reactive species, or by a combination of physical and chemical mechanisms. Wet etching refers to those techniques that remove material by direct contact of a chemical etchant solution.

A comparison of wet and dry etching techniques reveals their respective advantages and drawbacks. Wet etching offers the advantages of low-cost batch fabrication, good selectivity, easy scale-up of process, a fast etching rate, and simplicity due to few controlling parameters, while dry etching provides good control of etch rate, low cost of chemicals and applicability for sub-micron features (see (Madou 2002) for a comprehensive comparison of these two etching techniques).

The wet etching technique is much simpler than the dry etching technique. Also, an anisotropic etchant enables us to have a better control of the etch directions in comparison to isotropic etching. Hence, in the present research, anisotropic wet etching was used to fabricate the desired structure in bulk silicon. One of the most common anisotropic etchants is an aqueous solution of potassium hydroxide (KOH).

In anisotropic wet etching of silicon, the etch rate and direction are determined by the crystal structure of silicon. Silicon wafers are slices that have been precisely cut from a large block of silicon that was grown from a single seed crystal. The silicon atoms are all arranged in a crystalline structure, so the wafer is monocrystalline silicon (as opposed to polycrystalline silicon). Silicon wafers with different crystalline orientations and different thicknesses are commercially available, among which [100]- and [110]-oriented wafers are commonly used (see (Madou 2002) for a definition of crystallographic plane notations). The shapes of the resultant features are radically different for each type of these wafers when an anisotropic etchant is used.

In [100]-oriented wafers the etch front begins at the surface of the substrate in the openings of the etch mask and proceeds in the $\langle 100 \rangle$ direction, which is the perpendicular to the wafer face, creating a cavity with a flat bottom and skewed sides. The sides of the cavity are $\{111\}$ planes making a 54.74° angle with respect to the $\{100\}$ planes (i.e., the wafer face). The etching process ultimately stops when the four $\{111\}$ planes intersect, forming a cavity in the shape of an inverted pyramid or a V-shaped trench. This occurs only if the substrate is thicker than the projected etch depth. If the thickness of the substrate is less than the projected depth of the pyramidal cavity, the result is a through hole or perforation in the wafer. However, the area of the hole is

greater on one face of the wafer than it is on the other. This choice dictates that the side walls of the square window in a [100]-oriented wafer will be sloped inward instead of being vertical. It can be shown that for a 525 μm wafer thickness, the etching process will ultimately halt if the size of the etched hole is smaller than 743 μm , and therefore no through hole will be formed. In order to create a through hole, the thickness of the substrate needs to be reduced by etching from one face.

The shape of an etched trench or cavity in [110] wafers is drastically different. In silicon [110] wafers, four of eight equivalent $\{111\}$ planes are perpendicular to the $\{110\}$ -wafer surface. The remaining four $\{111\}$ planes are skewed at 35.26° with respect to the surface. The four vertical $\{111\}$ planes intersect to form a parallelogram with an inside angle of 70.5° . A groove etched in [110] wafers has the appearance of a complex polygon delineated by six $\{111\}$ planes, four vertical and two skewed. Etching in [110] wafers is useful for forming trenches with vertical sidewalls, though they are not orthogonal to each other.

For the fabrication of the mesopump, the [100]-oriented wafer was used, because for [110] wafers the etching window opening must be in parallelogram form rather than square shaped in order to obtain vertical walls. Also, since the difference between the opening areas of a through hole on the two faces of the substrate decreases if the wafer thickness is small, the large area on the back face of the wafer was etched to decrease the thickness. The front face of the wafer carrying a patterned mask (defining the array of perforations) was then etched to create the through holes. The details of the microfabrication process are presented in next section.

5.6.1 Step-by-Step Microfabrication Procedure

In this section step-by-step process flow for the micro fabrication of the electrodes is reviewed and a production recipe is presented.

5.6.1.1 Silicon Wafers

The substrate used in the current process was a standard 100-mm double-side polished wafer with a nominal thickness of 525 μm . Both sides of the wafer possessed the layers of thermally grown silicon dioxide (SiO_2) and silicon nitride (Si_3N_4). Because this is a double-side polished wafer, photolithography can be performed on both faces of the wafer.

The silicon nitride film serves as a mask during the wet etching process, and as an electrical insulator between the metallic film and silicon substrate. Notice that a layer of photoresist cannot act as a mask in the wet etching process, as it will be attacked by solution. Silicon nitride can be deposited by a wide variety of techniques. Due to their more uniform film properties, Low Pressure Chemical Vapor Deposition (LPCVD) deposited nitride wafers were purchased. The thickness of the nitride film was 3000 \AA . This is about the maximum available thickness that can be safely achieved by the LPCVD process. A number of important properties of the silicon nitride thin film are given in Table 5-1.

Table 5-1 Properties of Silicon Nitride

Properties	Value
Etch rate in KOH (water) 85°C 44g/100ml (nm/min)	< 1
Etch rate in conc. HF (\AA /min)	200
Residual stress (MPa)	100 (Tensile)

Electrical resistivity ($\Omega \cdot \text{cm}$)	10^{16}
Dielectric constant	6-7
Dielectric strength (kV/ μm)	0.1

Source: (Madou 2002)

The silicon dioxide layer, beneath the nitride layer, is first deposited on the silicon substrate wafer to offset the tensile residual stress of the silicon nitride layer, since the residual stress of the oxide layer is compressive. This is a general practice in the field of microfabrication. Moreover, this layer provides an electrical insulating layer similar to nitride layer. The oxide layer in our wafer was $1.5 \mu\text{m}$ thick and thermally grown on silicon. Several key properties of the thin layer of thermal silicon dioxide are given in Table 5-2.

Table 5-2 Properties of Thermal SiO_2

Properties	Value
Etch rate in KOH (water) 85°C 44g/100ml (nm/min)	2.8
Etch rate in conc. HF ($^\circ\text{A}/\text{min}$)	20,000
Residual stress (MPa)	20-40(compressive)
Resistivity ($\Omega \cdot \text{cm}$)	$0.3-0.5 \times 10^{16}$
Dielectric constant	3.9
Dielectric strength (kV/ μm)	0.02-0.03

Source: (Madou 2002)

In Figure 5-12 a schematic of the cross-section of a blank wafer is depicted.

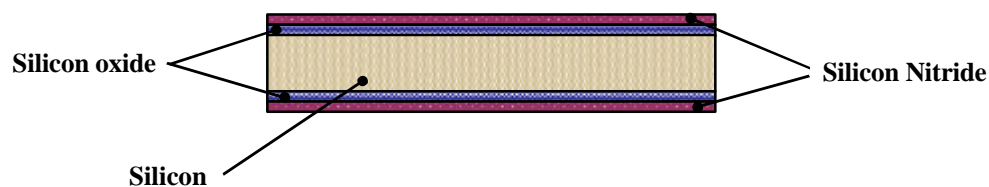


Figure 5-12 Cross-section of a blank wafer

5.6.1.2 Chromium and Gold Film Deposition

In next stage of the microfabrication process, one side of the wafer should be coated with chromium and gold films. There are different techniques for metal deposition, such as thermal evaporation and sputtering. Thermal evaporation is based on evaporating a metal target and depositing the vaporized molecules onto a substrate inside an evacuated chamber. In sputter deposition, minuscule chunks of metal are eroded from a target by a controlled bombardment of a flux of ions of an inert gas in a vacuum chamber, and deposited on a wafer placed at a suitable orientation with respect to the target. Sputtering is generally preferred over thermal deposition in many applications due to the higher adhesion strength of the film to the substrate. However, thermal evaporation provides a better purity of the deposited film, since a very high vacuum is applied. In the current process, thermal evaporation was used due to the ease of access to the necessary facility.

Thermal evaporation itself is divided into various types based on the heating technique such as resistive heating and electron beam. Our experience with resistively heated thermal evaporation did not result in appropriate metal deposition. Therefore, e-beam evaporation was used. E-beam evaporation results in higher quality films since the contamination is less than that in resistive heating.

Before deposition of the metal layers, the surface of the wafer must be carefully cleaned from any organic/inorganic contamination, in order to increase the adhesion. The wafer can be cleaned with wet chemicals followed by exposure to oxygen plasma. Pirhana is an appropriate liquid chemical for removing organic contaminations by oxidizing them. The pirhana solution is a 5:1 mixture by volume of H_2SO_4 with H_2O_2 . The

wafer was immersed in this solution for at least 3 minutes and then rinsed with DI water for at least 1 minute. Afterward the wafer was cleaned using oxygen plasma for 2 minutes in a chamber at a pressure of about 300 million Torr. Immediately after performing cleaning process, the wafer was transferred into the e-beam chamber to prevent any contamination.

As pointed out earlier, to provide adequate adhesion between the gold film and the substrate, a layer of chromium must be deposited beneath the gold film. In the current process, the thicknesses of the deposited chromium and gold films were 150°A and 3000°A , respectively. Figure 5-13 shows a cross-section of the wafer at the end of this stage.



Figure 5-13 Schematic sketch of the wafer cross-section after chromium-gold deposition

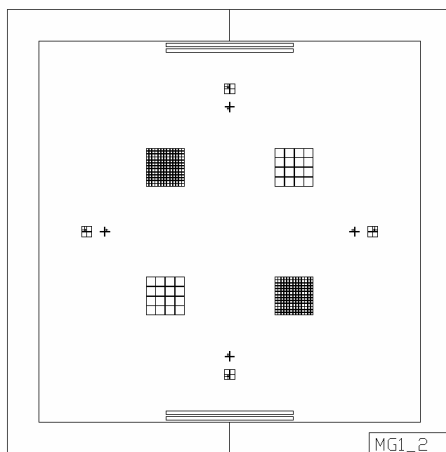
5.6.1.3 Photolithography to Generate the Pattern of Perforations

After deposition of the gold film, the square perforations must be patterned on the front side of the wafer. To accomplish this, the wafer should be coated with a uniform layer of photoresist, a photo-sensitive liquid polymer layer. Then the desired pattern, printed on a mask, is transferred to this layer using the optical exposure technique. In initial stages of the present research, a plastic transparency mask was used for a trial run, and after resolving the various practical issues related to the microfabrication procedure, a glass photomask was utilized for the final run. Photomask is a soda-lime glass plate of near-optical flatness with a patterned chromium layer that acts as an absorber of incidental light. This patterned face of the photomask is placed in contact with the

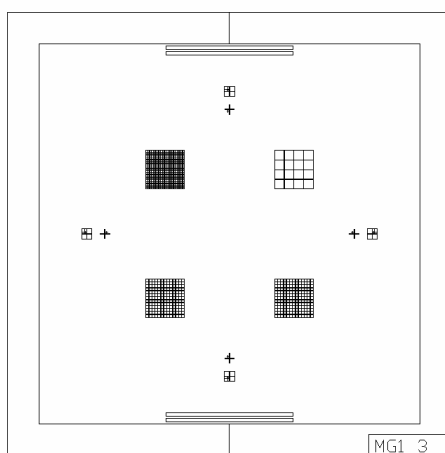
photoresist layer on the silicon substrate, and the combination is exposed to radiation from an ultraviolet source, thus developing the exposed regions of the photoresist. Two CAD drawings of the photomasks are presented in Figure 5-14. Notice that on every wafer four electrodes are fabricated. Together, the two masks, as shown in Figure 5-14, result in five different designs of the electrodes.

The photolithography process involves several steps that are listed below:

- I. Clean the wafer and then dehydrate it at 110 °C for 3 minutes;
- II. Apply a photoresist-adhesion promoter, Hexamethyldisilazane (HMDS), on the wafer;
- III. Apply and spin positive photoresist (Shipley 1813[®]) at 3000 rpm to obtain a thickness of 1.5 μm (see (Franssila 2004) for a description of positive photoresist);
- IV. Soft bake the wafer for 1 minute at 110°C on hotplate;
- V. Place the wafer with photoresist layer on the chuck of a lithography machine and align the wafer with the features on the mask;
- VI. Expose the photoresist to UV radiation for about 5.6 seconds (for exposure dose of 200 mJ/cm^2);
- VII. Rinse the wafer with the developer solution (Microposit 352[®]) for 30 sec to dissolve the exposed regions on the photoresist layer;
- VIII. Finally, rinse with DI water, inspect the pattern, and hard bake the photoresist for 30 minutes at 110° C on a hot plate.



(a)



(b)

Figure 5-14 Two CAD drawings of the photomasks used to pattern checkerboard shape windows

Figure 5-15 shows a schematic of the wafer cross-section after the photolithography stage.



Figure 5-15 Photoresist is patterned on the wafer front side

5.6.1.4 Etching the Gold and Chromium Films

In the next stage the gold and chromium films are etched sequentially. During this process, the photoresist acts as a mask, and as a result, only uncovered area are etched away. First, the wafer was immersed inside the gold etchant chemical (aqueous KI solution) for a few seconds depending on the chemical etch rate. Then, the wafer was inspected visually under a microscope to ensure that all the exposed gold film was removed. After rinsing with wafer, the wafer was immersed inside the chromium etchant chemical (HCl, CeSO₄ solution) for a period of time. The etch rate depends on the etchant and temperature of the solution. Sometimes heating the solution was necessary. Figure 5-16 shows the wafer cross-section sketch at the end of this stage.

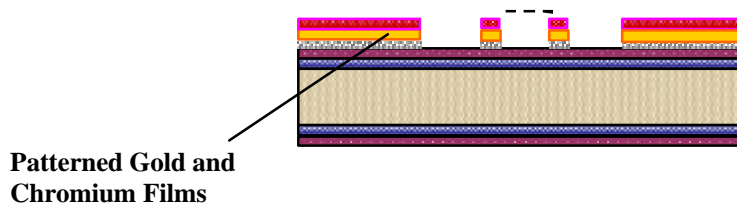


Figure 5-16 Gold and chromium films are etched

5.6.1.5 Etching the Nitride Layer Using RIE

After patterning the metal layers, the silicon nitride layer was etched using the Reactive Ion Etching (RIE) technique. The basic principle of this technique involves the generation of chemically reactive neutrals and ions that are accelerated under the effect of an electric or magnetic field towards a target substrate. Here, the ion bombardment on the silicon surface plays a central role. The reacting agent used to etch the silicon nitride layer was a mixture of CF₄ and O₂ gases. The volumetric ratio and the etching duration depends on the surface area of the sample, the geometry of the machine chamber, and the

RF power used for ionization of the reaction mixture. According to our experience, flow rates of 15.29 cfm CF_4 and 4.1 cfm O_2 produced an acceptable rate and uniformity of etching. The time needed to etch a 3000 \AA nitride layer was about 4 minutes. During this process the photoresist acted as a masking layer. At the end of this process the photoresist was removed using photoresist-solvent such as acetone. The wafer cross-section after this step is schematically depicted in Figure 5-17.

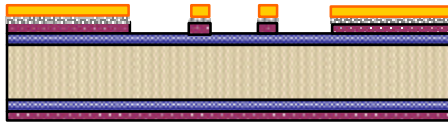


Figure 5-17 Nitride layer is etched using RIE technique

5.6.1.6 Photolithography and Wet Etching to Pattern the Bond Pads

In this stage the gold and chromium layers surrounding the patterned windows are removed and bond pads are formed. In order to protect the cavities patterned on the gold, chromium and nitride layers, a thick layer of photoresist must be spun over it. A CAD drawing of the mask utilized in this stage is given in Figure 5-18. Notice that the photomask must be aligned with respect to the previously fabricated features on the wafer. This can be accomplished by aligning the four alignment marks on the photomask and the wafer.

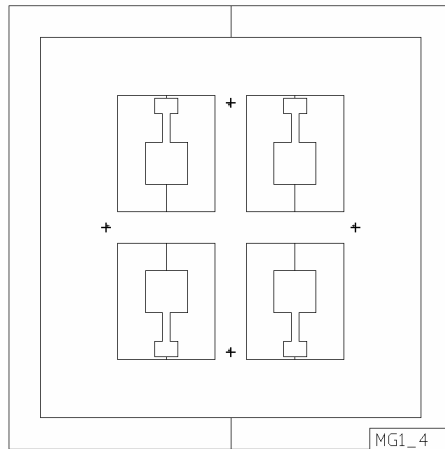


Figure 5-18 CAD drawing of the photomask used to pattern bond pads

The photolithography procedure for spinning a thick layer of photoresist is as follows:

- I. Clean the wafer and then dehydrate it at 110 °C for 3 minutes;
- II. Apply adhesion promoter, Hexamethyldisilazane (HMDS), on the wafer;
- III. Apply and spin positive photoresist (AZ9245[®]) at 1750 rpm for 5 seconds and then at 3000 rpm for 40 seconds to obtain a layer 5 μm thick;
- IV. Soft bake the wafer for 90 minutes at 110°C on hotplate;
- V. Align the mask with the features on the wafer;
- VI. Expose the photoresist to UV radiation for about 8.4 seconds (for an exposure dose of 300 mJ/cm²);
- VII. Immerse the wafer inside the developer (AZ400K[®]:water =1:3 by vol.) for 2-3 minutes;
- VIII. Rinse with DI water, inspect the patterns.

After photolithography, the gold and chromium films are etched. Figure shows the wafer cross-section at the end of this stage.

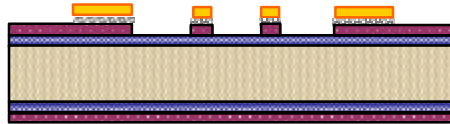


Figure 5-19 Chromium and gold layers are etched to form bond pads

5.6.1.7 Photolithography to Pattern the Wafer Backside Cavity

As explained earlier, in order to make through holes and reduce the effect of side wall skew for the etched square windows, the wafer thickness had to be reduced. This was done by etching the wafer from the backside. Therefore, a photolithography process was carried out on the wafer backside. The photolithography on the back face was also used to pattern the dicing mark lines on the wafer rear side. Doing so, we made sure that backside photomask was aligned with respect to the front side features, which was accomplished using the backside alignment technique. This technique uses an IR beam and relies on the fact that the silicon wafer is transparent to the IR beam. For protection during backside photolithography, the features on the wafer front side were first covered with a thick layer of photoresist. A CAD drawing of the backside mask is presented in Figure 5-20.

The photolithography procedure is the same as the one described earlier. The wafer cross-section at the end of this stage is presented in Figure 5-21.

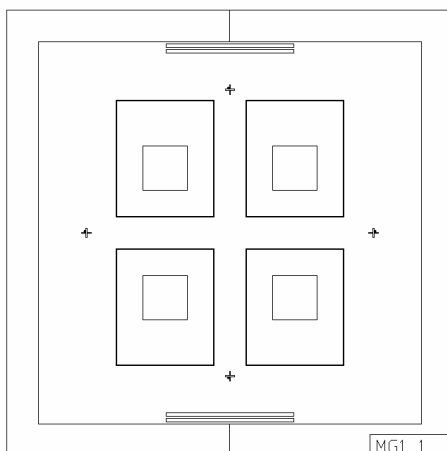


Figure 5-20 CAD drawing of the photomask used to pattern backside windows and dicing lines

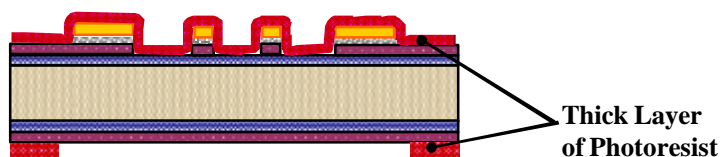


Figure 5-21 Photoresist is patterned on the wafer backside and spun on the entire wafer front side

5.6.1.8 Etching the Nitride Layer on the Backside of the Wafer Using RIE

After spinning and patterning the photoresist, the nitride layer on the backside of the wafer can be etched, as shown in Figure 5-22. The dry etching procedure using the RIE technique is the same as the one given earlier. After this stage, the photoresist is removed using the photoresist stripper solvent.

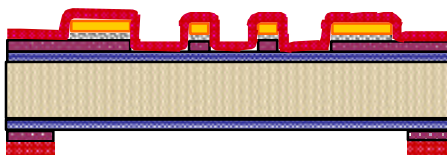


Figure 5-22 Silicon nitride film is etched on the backside of wafer

5.6.1.9 Etching the Oxide Layer on Both Sides of the Wafer

As pointed out earlier, an aqueous solution of potassium hydroxide (KOH) is used to etch bulk silicon and create through holes. However, the KOH etch rate of silicon dioxide is very low (see Table 5-2). Therefore, the silicon dioxide layer had to be removed by a more aggressive etchant before the bulk silicon underneath could be etched. This process was carried out using an isotropic silicon oxide etchant. Hydrofluoric acid (HF) and buffered hydrofluoric acid (BHF) are two standard silicon dioxide etchants. Both HF and BHF show high oxide-to-nitride selectivity (~100:1). Using concentrated hydrofluoric acid, etching the 1.5 μm oxide layer took about 1 minute. HF and water both wet silicon dioxide and silicon nitride but do not wet silicon. The length of the etch process may be controlled by visually monitoring the wafer. Occurrence of a hydrophobic condition on the wafer signals completion of the etch step. The schematic of the wafer cross-section at the end of this stage is presented in Figure 5-23.

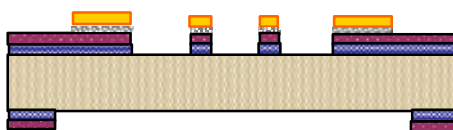


Figure 5-23 Wafer cross-section after etching silicon dioxide layers

5.6.1.10 Etching of Silicon from Both Sides of Wafer

As mentioned before, anisotropic (or directional) etchants etch much faster in one direction than in another, exposing the slowest etching crystal planes over time. Values of the relative etch rates for three planes of interest can be as high as (111) : (100) : (110) = 1: 400:600 (Kovacs, Maluf et al. 1998). These values strongly depend on the chemical composition, concentration, temperature of the etchant solutions used, and agitation in the

etch bath. The silicon etch rate is maximized at 72 °C for a KOH concentration of 20 % by weight. However, the average surface roughness of Si continuously decreases with increasing KOH concentration. The roughness is thought to be due to the development of hydrogen bubbles, which obstruct the transport of fresh solution to the silicon surface, causing micromasking. Average roughness is also influenced strongly by fluid agitation. Stirring can reduce the roughness by the removal of hydrogen bubbles, produced from the reaction, from the etching surface.

For anisotropic etching of our wafer using KOH, the recipe given in Table 5-3 was used. Before the silicon wet etching process, the wafer was immersed in buffered hydrofluoric acid (BHF) for 90 seconds to etch any remaining oxide residing on the silicon surface.

Table 5-3 KOH solution recipe

KOH solution concentration (by weight)	% 25
Solution temperature (°C)	75
Stirring speed (rpm)	270

The wafer was placed vertically inside the KOH solution so that the hydrogen bubbles, caused by the etching of the silicon from both sides, could be easily released. The temperature of the solution was controlled with a thermometer probe placed inside the solution that adjusted the hot plate temperature accordingly. The etch rate was found to be about 1 $\mu\text{m}/\text{min}$. Figure 5-24 presents the wafer cross-section after the silicon wet etching process. As shown, the walls of the etched windows are sloped inward. The wafer is etched from both sides and to a depth of around 260 μm , where both etching surfaces

come into contact and form through holes. The silicon wet etching of the wafer represents the last step in the electrode microfabrication process.

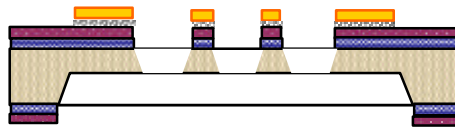


Figure 5-24 A schematic sketch of wafer cross-section after silicon wet etching process

5.6.2 Mesopump Packaging Procedure

The first stage of packaging was to dice the devices along the etched dicing marks. As pointed out earlier, on every wafer four electrodes were created, which had to be detached from the wafer platform. This was done by dicing the wafer. Before dicing the wafer, the wafer was covered as much as possible with a thick layer of photoresist and then hard baked. This layer provided protection during the mechanical handling and dicing process. The etched trenches on the backside of the wafer provided the path lines for the dicing process. Pictures of the diced electrodes along with their schematic sketch are presented in Figure 5-25.

As described earlier, a spacer layer is laid between the two electrodes, creating a constant gap between them. The spacer was in the form of a square Pyrex layer with a square window created inside it. This component was fabricated by a commercial manufacturer using ultrasonic machining.

The mesopump housing was made of acrylic and fabricated using conventional CNC machining. The mesopump housing and Pyrex spacer are shown in Figure 5-26. There were different options regarding which electrode design to use as the emitter and the collector electrodes. Our study showed that the best design for the emitter and

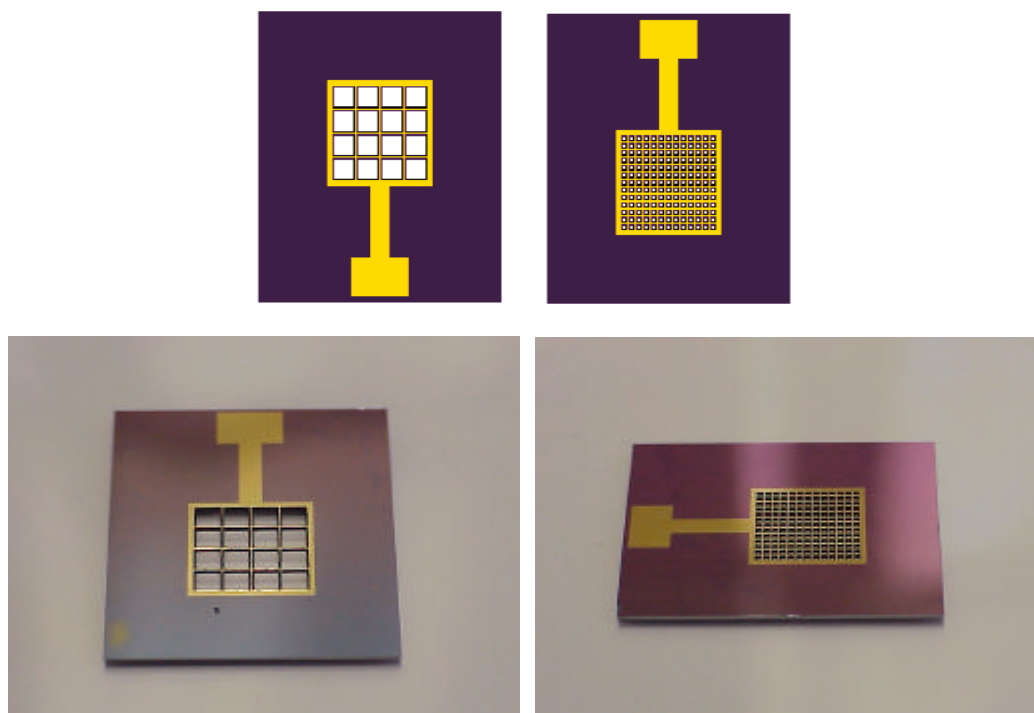


Figure 5-25 Schematic sketches of electrodes (top), and microfabricated electrodes after dicing (bottom)



Figure 5-26 Mesopump housing and Pyrex spacer

collector electrodes were the ones which had respectively the largest and the smallest edge-to-edge distance, 'd'. This is because as 'd' decreases, the injection points come closer to each other, and consequently the intensified electric field drops off (see section

5.2). Our experimental test with a swapped arrangement of electrodes resulted in minor pressure head generation.

Before assembling the pump component, the wires had to be connected to bond pads. In current work, the conventional soldering method was carefully used to make an appropriate connection. Then, the components were placed inside the housing, and quick-dry epoxy adhesive was used to secure them and bond the lid to its housing body. A picture of the final structure of the assembled mesopump is shown in Figure 5-27.

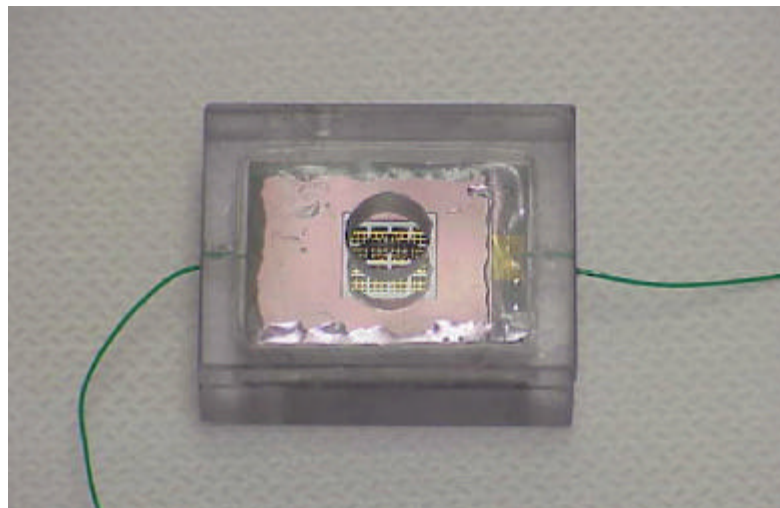


Figure 5-27 Assembled mesopump

5.7 Summary

In this chapter, the design requirements of the ion-injection mesopump were discussed, and based on the requirements a preliminary pump was designed and tested. As the experimental tests with the preliminary pump confirmed the concept and functionality of the design, a new design based on the microfabrication technology was developed. The new design exhibited a number of advantages compared to the preliminary design. The electrode microfabrication steps were fully described, and the packaging method was explained.

CHAPTER 6: EXPERIMENTAL APPARATUS AND TEST PROCEDURES

6.1 Introduction

In this chapter, the experimental setup and test facilities used in current study are introduced. A test section and an experimental test loop was designed and constructed to experimentally characterize the performance of the electrohydrodynamic pump developed in the present study.

6.2 Flow Loop Testing Setup

An important characteristic of the performance of an EHD pump is the flow rate that it can deliver. To measure this flow rate, a closed loop setup was designed and fabricated. The flow loop consisted of the EHD pump, a closed tubing circuit, and a flow measuring instrument. In addition, a differential pressure transducer was used to measure the pressure head that is generated across the pump. In the design of the flow loop, the following requirements were taken into consideration:

1. The total internal volume of the loop should be reasonably small in order to minimize the pumping response time and represent that of an actual miniaturized cooling loop.
2. The internal diameter and the length of the tubing in the circuit should be selected such that a reasonable pressure drop is produced.

3. Since the electrohydrodynamic phenomenon is particularly sensitive to the presence of particles and impurities, the fittings, connections, and circuit elements should be selected from inert and nondegrading materials.
4. It has been found that most of the refrigerants and cooling fluids exhibit a great tendency to absorb moisture from the ambient environment. This can drastically change the electrical properties of the working fluid. Therefore, the loop should be designed in such a way that during the fluid charging process, the possibility of exposure of the working liquid to the surrounding air is minimized.
5. The trapped bubbles inside the loop can negatively affect the electrohydrodynamic process. Therefore, the loop should be designed in such a way that any air infiltration to the loop is prevented or minimized.
6. Similar to the trapped bubbles, the dissolved gas in the working liquid can interfere with the electrohydrodynamic pumping process. In fact, during the fluid charging process the dissolved gas may emerge from the liquid phase, and as a result of dielectrophoretic effect, it is likely that a layer of gas shields the collector electrode. Therefore, it is necessary to design the loop in such a way that the dissolved gas can be extracted in-situ from the working liquid as much as possible.
7. The fluid flow and pressure measurement techniques should not interfere with or affect the pump performance.
8. The flow rate measurement technique must be sensitive enough to be able to detect the relatively low flow rates efficiently and accurately.
9. The pressure transducer should have a short response time and must detect low pressure heads.

10. To obtain repeatable results, the sensitivity of the measurement techniques to the variation of environmental conditions should be minimal.

Considering the above requirements, a closed flow measurement loop was designed and built. A schematic of the flow loop is depicted in Figure 6-1.

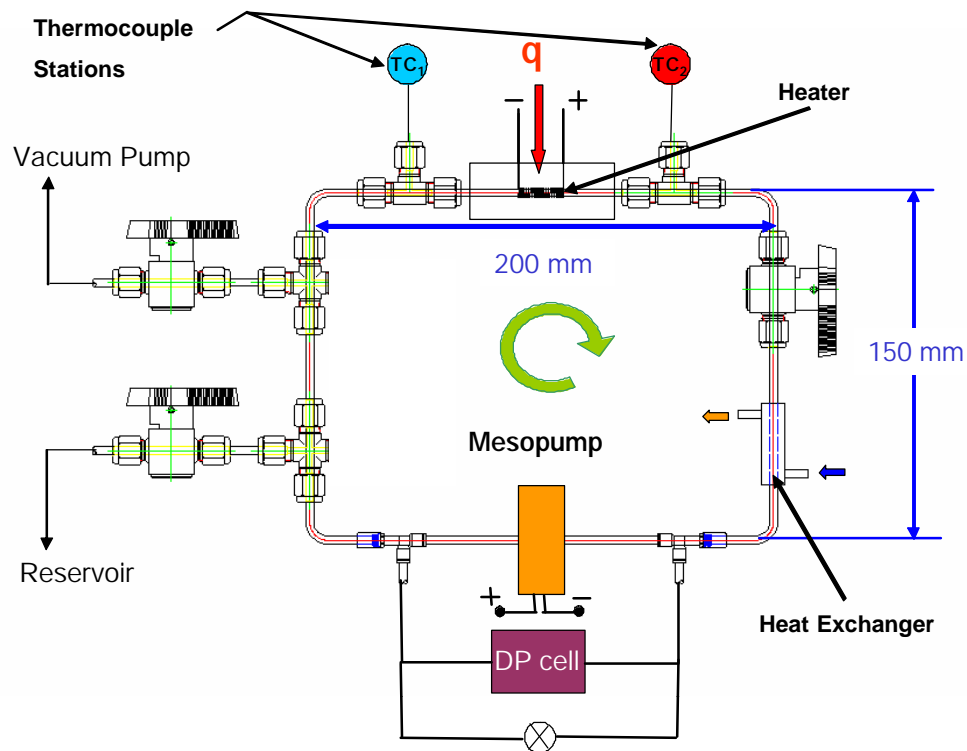


Figure 6-1 Schematic sketch of closed flow loop

One of the more accurate techniques for measuring mass flow rate is a heat balance technique in which heat is added to the fluid at one location and temperature probes measure the difference in temperature upstream and downstream of this heat source and from there through an energy balance the flow rate can be calculated. This technique was implemented in the flow loop test section.

The flow loop test section consisted of the following components:

1. Differential pressure transducer (Validyne Engineering, Inc., DP15)

2. Thin-wall stainless steel tubing (wall thickness: 0.25 mm, ID: 2.91 mm)
3. Flow measurement heating element (electrical resistance: 50 ?)
4. Ultra thin-wall stainless steel tubing for the heat balance flow measurement technique (wall thickness: 0.125 mm, ID: 2.92 mm)
5. Two thermocouple stations (type T, Omega, Inc.)
6. Heater insulation (thermal conductivity: ≈ 0.06 W/mC)
7. Heat exchanger (length: 40 mm, OD: 9.2 mm)
8. Valves and connectors (Swagelock, Inc.)
9. Chiller (RTE-101, Thermo NESLAB, Inc.)
10. Reservoir (volume: 50 ml, Swagelock, Inc.)
11. Degassing heater (Kapton encapsulated, resistance: 80 ?)
12. Compound pressure gauge (Range: 0 to -30" Hg/ 0-15 psi)
13. Data acquisition system (Agilent, Inc.)
14. DC power supply (Hewlett-Packard, Inc.)
15. Vacuum pump (Ritchie Engineering Company, Inc)
16. DC high-voltage power supply (0-30 kV, Glassman, Inc.)

Notice that items 9 to 16 are not shown in Figure 6-1. A picture of the test section is shown in Figure 6-2.

To precisely measure the volumetric flow rate, several measures in the loop design were implemented. The axial conduction effect through the wall tube was minimized using ultra thin-wall tubing with a 0.125 mm thickness. However, since the ultra thin tube was not bendable, a thicker tube (wall thickness: 0.250 mm) was used for the rest of the loop. Instead of standard steel connectors, Teflon tee connectors were used

to reduce heat loss through the body of these fittings. Furthermore, instead of measuring the tube wall temperature, thermocouple probes were inserted inside the tube so that the fluid temperature was measured directly. Although this measured temperature still may not exactly represent the fluid flow bulk temperature, the difference was expected to remain quite small. The thermocouples were placed about 100 mm apart. To minimize the heat dissipation to the ambient air, Polyurethane foam was used to insulate the heating element. The foam is moldable and provided appropriate insulation. The heating element, consisting of a thin wire coil, was wrapped tightly around the ultra thin-wall tube and was embedded inside the insulation foam. Figure 6-3 shows the heating element before and after insulation.

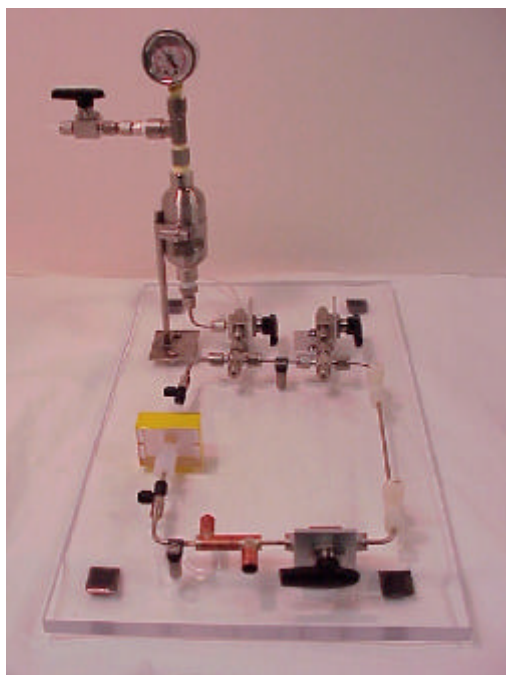


Figure 6-2 Flow measurement closed loop

The working fluid for the EHD mesopump was HFE-7100 (3M, Inc.). Before charging with HFE-7100 liquid, the loop was cleaned several times. First, the loop was flushed with alcohol a number of times. Then nitrogen gas was passed through the loop for a

period of time to dry the loop and drive any particles out of the system. Subsequently, the loop was evacuated and kept so for several hours to make sure that any remaining alcohol that might have been trapped inside the gaps was vaporized. Afterward, nitrogen gas was again run through the loop to evacuate any vaporized alcohol. Next, the loop was flushed with HFE-7100 liquid a few times and then evacuated and charged with the degassed HFE-7100 liquid, the process of which is described next.

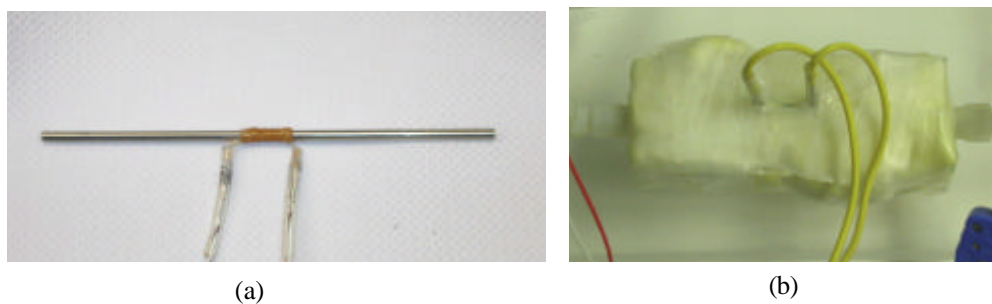


Figure 6-3 Heating element (a) before insulating (b) after insulating

We have noticed that despite extra care HFE-7100 contains dissolved gases that mostly might get into the system through the charging process or at the manufacturing/bottling stage. These gases generally cause undesired generation of bubbles during the charging process of the evacuated loop. These bubbles can cause an early spark-over between electrodes at a low voltage and can also result in an error in pressure measurement by the differential pressure transducer. To eliminate this problem, a heating technique was used to degas the working liquid. A flexible surface heater was placed on the outer wall of reservoir to heat up its content. The process for degassing and charging the loop was as follows. Initially, the entire system consisting of the reservoir and the closed flow loop was evacuated. Then the closed loop was isolated from the reservoir by closing the connecting valve, and the reservoir was charged with fresh HFE-7100 liquid. The reservoir was heated slowly to the boiling point of the liquid (about 60° C). During this

process, the dissolved gases gradually escaped in the form of bubbles through the connecting tube to the ambient air. The liquid was kept at boiling temperature for a few minutes. Due to condensation at the connections, the amount of liquid inside the reservoir did not reduce appreciably. Then, the reservoir was disconnected from the ambient environment by closing a valve. Next, the valve connecting the loop to the reservoir was opened to charge the loop. Due to the high sensitivity of the pressure transducer diaphragm to any shock that may occur during charging, the valve was opened very slowly.

6.3 EHD Mesopump Working Fluid

As discussed earlier, in the current research, Methoxy-nonafluorobutane $C_4F_9OCH_3$ (HFE-7100) was used as the working liquid. HFE-7100 is a clear, colorless dielectric liquid. Compared to many hydrofluorocarbons (HFCs), the global warming potential (GWP) of HFE-7100 is low, and as a result, HFE-7100 is a more environmentally-friendly choice than most other HFC refrigerants. The main advantage of this liquid is its relatively high dielectric constant (7.39) and low electrical conductivity ($\sim 3.0 \times 10^{-8}$ 1/? m). As explained in Chapter 2, a higher dielectric constant leads to a higher pumping head, while a lower electrical conductivity reduces power consumption of the pump, thus higher efficiency for the EHD pump. Another advantage of HEF-7100 is that it is a liquid at atmospheric pressure, thereby eliminating the need to keep the loop at high pressure conditions as is the case with some of the typical refrigerants. In fact, the boiling temperature of this liquid at atmospheric pressure is 61 C. Although it has suitable electrical properties, HFE-7100 has poor thermal properties compared to water. However, the high electrical conductivity of water makes it

unsuitable for the present application. Also, water is not an ideal coolant for electronics cooling since water is corrosive, and any accidental leakage is potentially catastrophic. A comparison between the physical properties of HFE-7100, water, and a number of other dielectric liquids is presented in Table 6-1.

Table 6-1 Physical properties of HFE-7100 in comparison with a number of other liquids*

Properties	HFE-7100	Water	FC-72	n-hexane	R-123	Liq. N ₂
Molecular weight, g/mol	250	18	340	86.1	152.9	28
Density (kg/m ³)	1480	997	1680	659	1464	810.6
Kinematic viscosity (m ² /s)	0.37×10^{-6}	0.89×10^{-6}	0.4×10^{-6}	0.45×10^{-6}	0.29×10^{-6}	0.21×10^{-6}
Thermal conductivity (W/m.K)	0.069	0.595	0.057	0.126	0.077	0.139
Specific heat (J/kg.K)	1180	4183	1047	2357	1035	2038
Boiling point (C)	61	100	56	69	27.8	-195.8
Heat of vaporization @ B.P., kJ/kg	111.6	2257	88	330	229	198.8
Surface tension (N/m)	0.0136	0.072	0.012	0.018	0.015	0.009
Vapor pressure (Pa) @ 25 C	26,931	3,169	30,930	20,260	91,477	N/A
Dielectric constant	7.39	80	1.76	1.9	4.5	1.43
Volume resistivity (? m)	3.29×10^7	1.0×10^4	1.0×10^{15}	11.0×10^{17}	1.47×10^{10}	_____
Solubility of air (ml./100ml)	53	1.4×10^5	48	_____	_____	_____
Solubility of water (ppm by weight)	95	N/A	10	Insoluble	_____	_____
GWP (100 year ITH)	320	N/A	9000	_____	93	_____

*All values are determined at 25 C except for Liq. N₂, for which properties are determined at boiling point

6.4 Instruments and Measurement Devices

The objective of this section is to review the specifications of the instruments and measurement devices used in the current study.

Differential Pressure Transducer

As explained above, a differential pressure transducer was used to measure the pressure difference across the inlet and outlet of the mesopump. The pressure transducer was a variable reluctance type with fast response time. It consisted of a diaphragm of magnetically-permeable stainless steel clamped between two blocks of stainless steel in each of which an inductance coil was embedded. A pressure difference applied through the pressure ports deflected the diaphragm toward the cavity with the lower pressure, decreasing one gap and increasing the other. As the magnetic reluctance varied with the gap and determined the inductance value of each coil, the diaphragm deflection increased the inductance of one coil and decreased that of the other. The major specifications of the pressure transducer are presented in Table 6-2.

Table 6-2 Pressure transducer specifications

Instrument and Facility	Model and Manufacturer	Specifications
Differential pressure transducer and carrier demodulator	Variable reluctance DP15, Validyne Engineering Corp.	<ul style="list-style-type: none"> • Pressure Range: 0- 880 Pa • Accuracy: $\pm 0.25\%$ FS • Linearity: $\pm 0.05\%$ FS

Data Acquisition Unit

A data acquisition unit was used to measure and record the thermocouple signals, the electrical voltage, the current applied to mesopump, and the output signal of the

pressure transducer demodulator. The relevant specifications of the data acquisition unit are presented in Table 6-3.

Table 6-3 Data acquisition unit specifications

Instrument and Facility	Model and Manufacturer	Specifications
Data acquisition unit	34970A, Agilent Technologies, Inc.	<ul style="list-style-type: none"> • Best range of Accuracy for thermocouple type T: 1.0 C • DC voltage measurement accuracy for a range of 10V: \pm (0.0035 % of reading + 0.0005% of range) • Resolution: 1 ppm

DC High-Voltage Power Supply

A DC high-voltage power supply was utilized to provide the required potential for the operation of the EHD mesopump. Selected specifications of the power supply are given in Table 6-4.

Table 6-4 DC high-voltage power supply

Instrument and Facility	Model and Manufacturer	Specifications
DC high-voltage power supply	EH, Glassman High Voltage, Inc.	<ul style="list-style-type: none"> • Rated output voltage: 0-30 kV • Output current: 0-3 mA • Accuracy: 1% of setting+ 1% of rated • Voltage monitor: Zero to +10V DC signal is equivalent to zero to rated voltage. Accuracy, 1% of rated voltage. • Current Monitor: Zero to +10V DC signal is equivalent to zero to rated current. Accuracy, 1% of reading +0.05% of rated current

DC Power Supply

A DC power supply was used to control the amount of heat needed for the thermal flow measurement technique. The rate of heat input was adjusted such that an appropriate temperature difference between thermocouples was measured. The relevant specifications of the DC power supply are summarized in Table 6-5.

Table 6-5 DC power supply specifications

Instrument and Facility	Model and Manufacturer	Specifications
DC power supply	6614C, Hewlett Packard, Inc.	<ul style="list-style-type: none"> • Rated output voltage: 0-100V • Output current: 0-0.5 A • DC voltage accuracy: 0.03% of setting+ 12 mV • DC current accuracy: 0.2% of setting + 0.1 mA

High Resolution Digital Multimeter

Although the digital multimeter was not used directly while running the experiment, it was needed to calibrate the high voltage power supply accurately. In Table 6-6 some of the specifications of digital multimeter are presented.

Table 6-6 Digital multimeter specifications

Instrument and Facility	Model and Manufacturer	Specifications
Digital multimeter	34401A, Agilent Technology, Inc.	<ul style="list-style-type: none"> • DC voltage accuracy (for 1 V range): 0.004% of reading+ 0.0007% of range • DC voltage accuracy (for 10 V range): 0.0035% of reading+ 0.0005% of range

		<ul style="list-style-type: none"> • DC current accuracy (for 10 mA range): 0.05% of reading+ 0.02% of range
--	--	---

6.5 Experimental Procedure

In this section the procedure followed in a typical experiment is briefly described.

The step-by-step procedure is as follows:

- Perform calibration (see section 7-2) for the test setup instruments including thermocouple probes, pressure transducer and power supply;
- Run leakage tests for the closed loop setup. This should be performed by keeping the test loop at a high pressure and vacuum. The inside pressure of the loop should not appreciably change within the duration of 24 hours and a pressure difference of 1 atm.
- Cleanse the loop several times as described in section 6-2;
- Evacuate and then charge the loop with HFE 7100 as explained in section 6-2;
- Degas the working liquid using a boiling technique (see section 6-2);
- Power up the instruments including the data acquisition system, pressure transducer and power supply;
- Power up the chiller and set the cooling water temperature to an appropriate value;
- Increase voltage in steps;
- At each step monitor the upstream and downstream temperatures, pressure difference across the mesopump, and electrical current between electrodes. Wait until hydrodynamic, thermal and electrical steady-state conditions are established;
- Record the measured data for each step;

- Stop the experiment when the applied voltage is about liquid breakdown voltage.
Decrease the voltage to zero and shut down all the instruments;
- Convert the measurement from each instrument by using the respective calibration curve;
- Analyze and reduce the data.

6.6 Summary

In this chapter, the experimental setup consisting of a closed flow loop with flow and pressure measurement units was introduced. To minimize the measurement error and conduct the experiment effectively, a number of requirements were defined, and the flow loop was designed accordingly. The specifications of the measurement units and experimental instruments were presented in this chapter. Description of the experimental loop and experimental procedure as a whole were also documented in this chapter.

CHAPTER 7: EXPERIMENTAL AND NUMERICAL RESULTS

7.1 Introduction

The results of the current research will be presented in two sections. In the first section, the experimental results will be taken into consideration. Our experience has shown that the calibration of the instrument and test section plays a central role in the subsequent data reduction and interpretation of the results. Therefore, in the first section a review of the calibration methodology will be presented, and then the experimental results will be presented. In the second section, the numerical results will be presented and a comparison between experimental and numerical results will be given.

7.2 Calibration and Experimental Results

7.2.1 Flow Loop and Instrument Calibration

Before conducting any experiments, all the instrument and measurement devices had to be calibrated. This was crucial since the final results are very sensitive to the measurement accuracy. For small-scale systems this sensitivity is even more important. In this part, the calibration methodology of the instruments will be reviewed.

7.2.1.1 Calibration of Thermocouples

To calibrate the thermocouples a temperature-controlled bath circulator was used. The thermocouples and a resistance temperature detector (RTD) were placed inside the bath. The bath temperature was changed gradually, and at each step the temperatures

measured by the thermocouples and RTD were recorded simultaneously. Considering the accuracy of the RTD, it was determined that the accuracy of the temperature measurement using thermocouples was in the range of 0.2 °C and the accuracy for the temperature difference measurement was about 0.3 °C. The result of the calibration for one of the thermocouples is presented in Figure 7-1. As expected, a linear calibration curve was obtained.

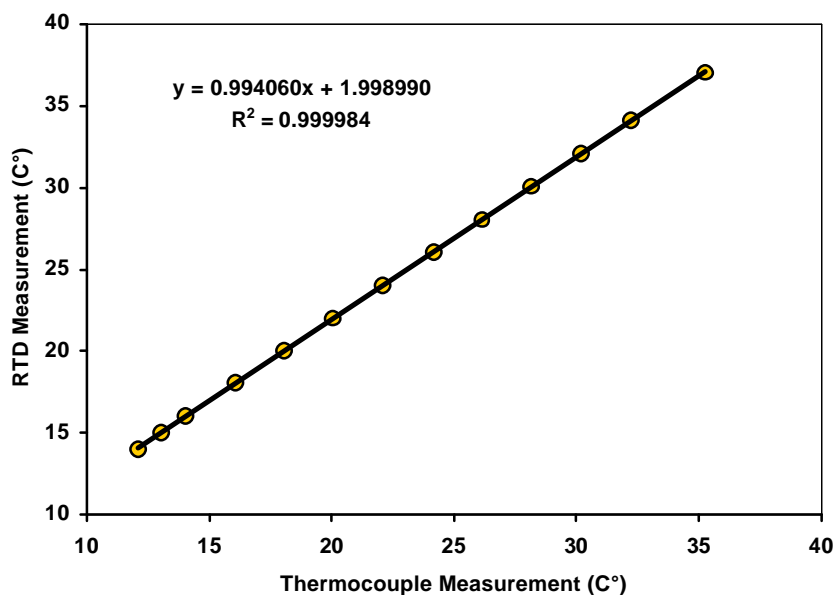


Figure 7-1: Thermocouple calibration curve

7.2.1.2 Calibration of Pressure Transducer

The calibration process for the differential pressure transducer was conducted using a U-tube manometer. In this technique one leg of the U-tube was kept open to the ambient environment, while the other leg was connected to one of the transducer ports. However, there was no direct contact between the water inside the U-tube and the diaphragm of the transducer, since a volume of air was confined between the free surface of the water in the U-tube and the transducer diaphragm. This technique eliminates the

possibility of having any bubble generation in the transducer port and hence no surface tension effect. Based on the results of our calibration process, the accuracy of the transducer was estimated to be about 5 Pa. The pressure transducer calibration curve is depicted in Figure 7-2. Here y and x axes represent the measured pressure by the U-tube and the transducer output voltage, respectively.

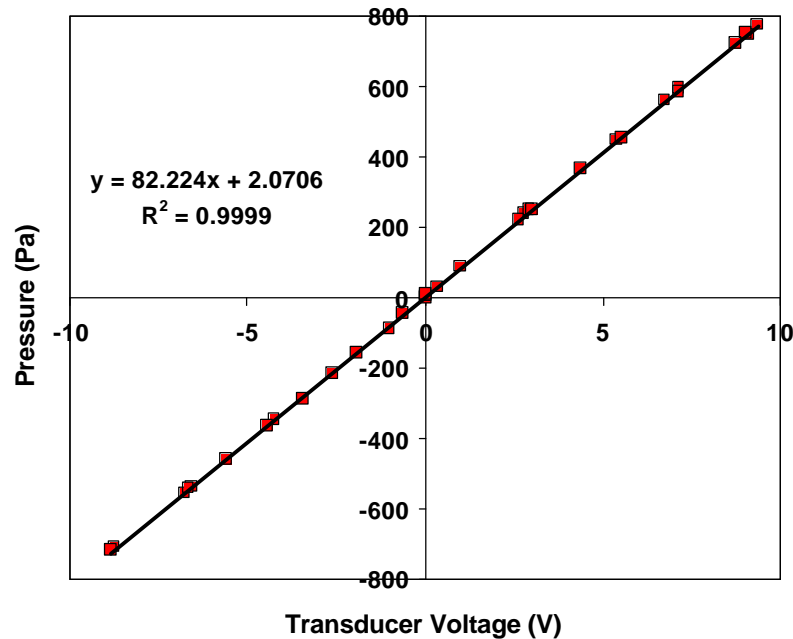


Figure 7-2 Pressure transducer calibration curve

7.2.1.3 Calibration of High-Voltage Power Supply

For the high-voltage power supply, the analog monitor signals of the voltage and current outputs were used for calibration. The calibration of the voltage monitor output was performed using a high voltage probe with a conversion factor of 1000 and a multimeter. The current monitor output of the power supply was calibrated using 100 M Ω constant resistance and a high accuracy multimeter. The estimated accuracy of the voltage monitor signal was expected to be about 1% of the applied voltage. For the current, a nonlinear

relationship between the actual applied current and the analog monitor signal at very low current value was observed. Since the range of the current of the EHD pump is very low (of the order of a few μA), our estimation showed that the accuracy of the current output signal was around $2\mu\text{A}$. The calibration curves of the high-voltage power supply are presented in Figure 7-3 and Figure 7-4, respectively.

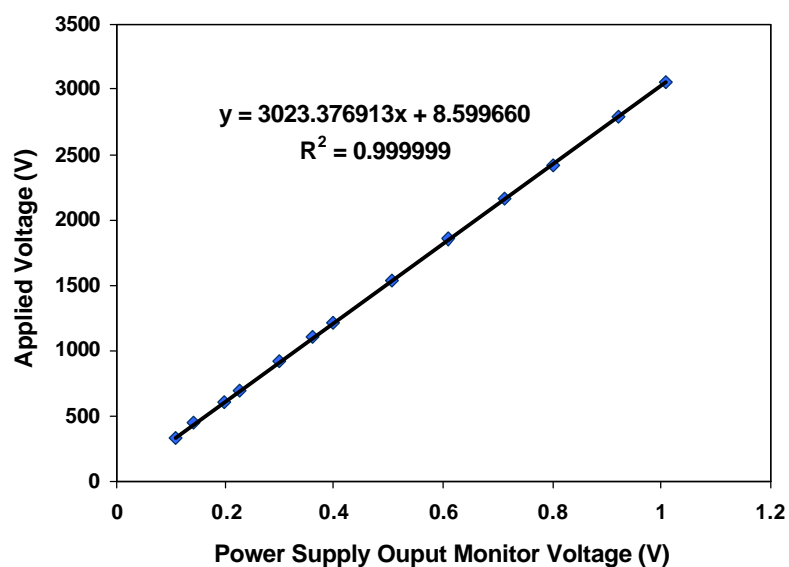


Figure 7-3 Voltage calibration curve for high-voltage power supply

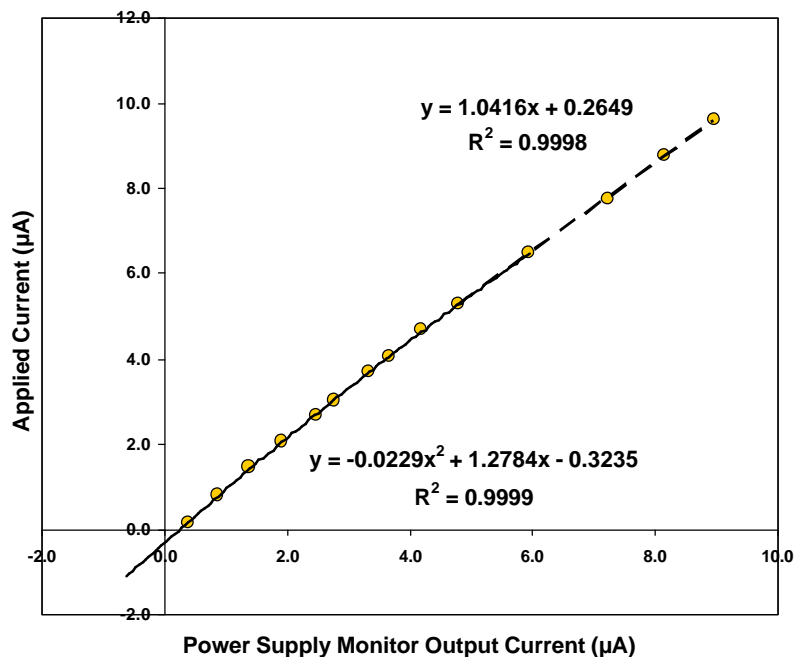


Figure 7-4 Current calibration curve for high-voltage power supply

7.2.1.4 Calibration of the Flow Loop

To find the relation between the actual volumetric flow rate and the one obtained using the thermal measurement technique, the closed flow loop was calibrated using a gear pump. This calibration was performed because no matter how well the tube and heating element between the two thermocouples are insulated, some heat loss to the ambient environment is inevitable. Besides, this calibration technique allowed us to find the relationship between the working fluid volumetric flow rate and the pressure drop inside the loop. To conduct the calibration, the EHD mesopump was replaced with the gear pump (Model MCP-Z, Ismatec, Inc.) as shown in Figure 7-5. The gear pump is able to pump the liquid at a user specified flow rate (2.52 to 252 ml/min).

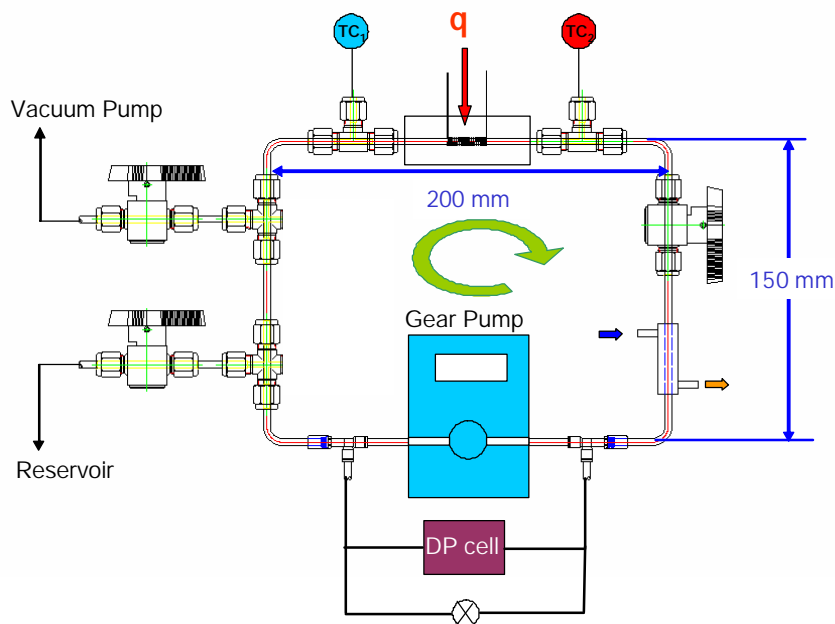


Figure 7-5 A gear pump was used to calibrate the flow measurement technique.

Due to its ease of application, water was used as the working liquid for the calibration instead of HFE-7100. However, as will be shown shortly, we were able to extend our calibration results to HFE-7100. As the gear pump circulated the water at a specific flow rate, the temperatures at the upstream and downstream of the heat source as well as the pressure drop inside the loop were recorded. Then, the pump flow rate was changed in several steps, at each of which data was recorded. Using the obtained results, the ratio of the heat transferred to the circulating liquid to the total applied heat was calculated. This ratio is defined as follows:

$$\text{Ratio of the heat transferred to the working liquid} = \frac{\dot{m}C_p \Delta T}{\dot{Q}}$$

(7-1)

where \dot{m} is the supplied mass flow rate by the gear pump, ΔT is the temperature difference across the heat source measured by thermocouples, and \dot{Q} is the rate of applied heat by the heating element. The results are presented in Figure 7-6. As seen

there, the results were obtained for different conditions of the controlling valve. This valve was placed in the closed loop circuit to control the pressure drop of the loop (see Figure 7-5). However, since the heat loss depends only on the volumetric flow rate and not on the pressure drop, the variation of heat loss should be independent of valve condition.

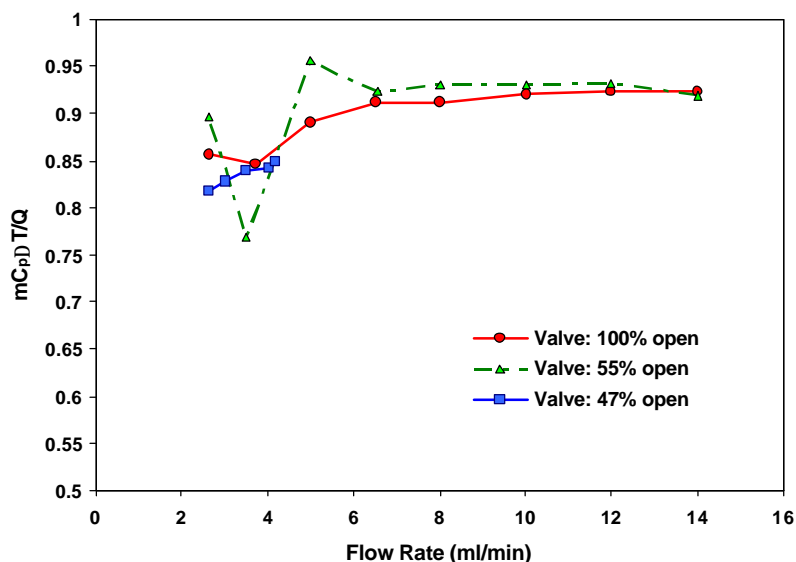


Figure 7-6 The variation of heat loss versus volumetric flow rate

From Figure 7-6 it can be concluded that the heat loss is higher at low flow rates and its maximum value is about 20%.

The results of the relationship between the actual volumetric flow rate supplied by the gear pump and the one evaluated by the thermal technique are pictured in Figure 7-7. A linear relationship was observed.

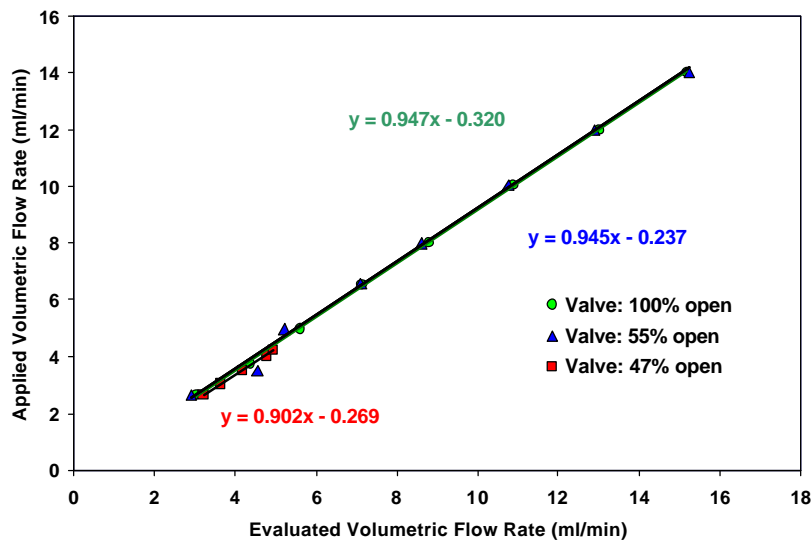


Figure 7-7 The calibration curve for the thermal based volumetric flow rate measurement technique

From this result, if we calculate the volumetric flow rate using the thermal technique, we can obtain the actual volumetric flow rate of the circulating liquid inside the closed flow loop. The dimensionless form of this graph in terms of Reynolds numbers when the valve is fully opened is presented in Figure 7-8.

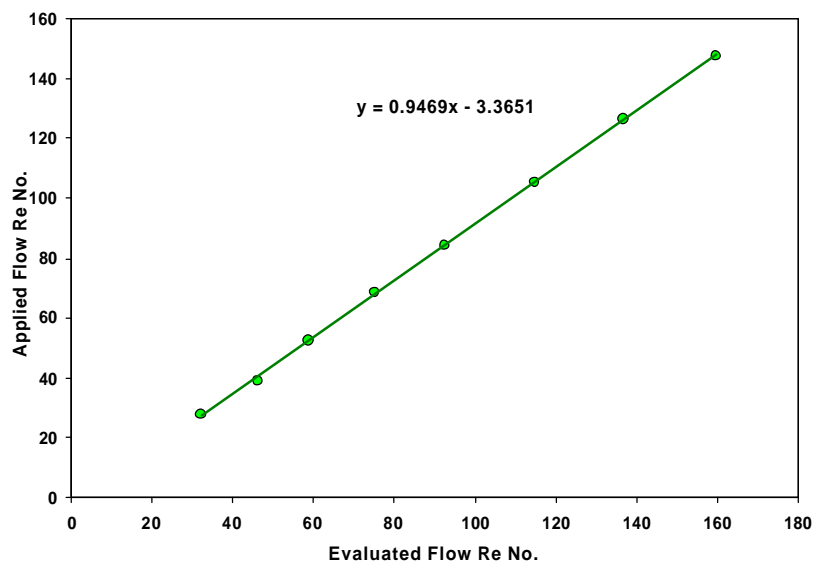


Figure 7-8 The calibration curve for the thermal based volumetric flow rate measurement technique in terms of dimensionless numbers

The relation between the applied volumetric flow rate of the liquid and the pressure drop along the loop was also found using the differential pressure transducer. The results are presented in Figure 7-9 and Figure 7-10 in terms of dimensional and dimensionless parameters, respectively.

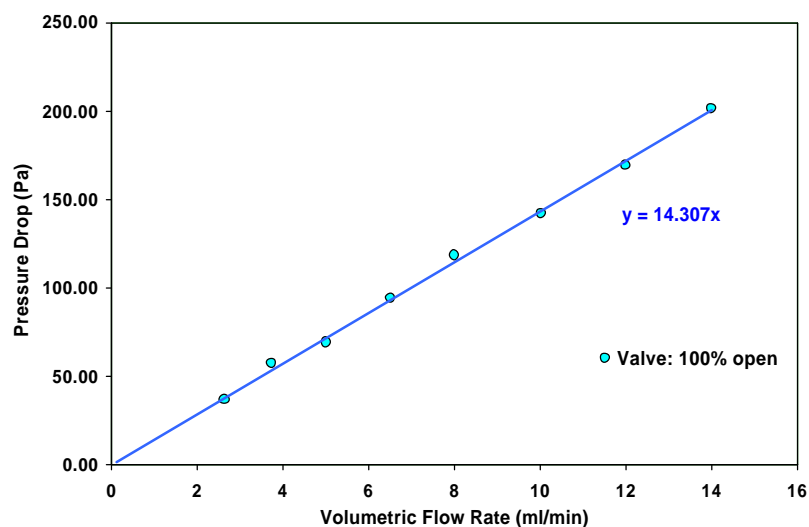


Figure 7-9 The flow loop pressure drop versus the volumetric flow rate

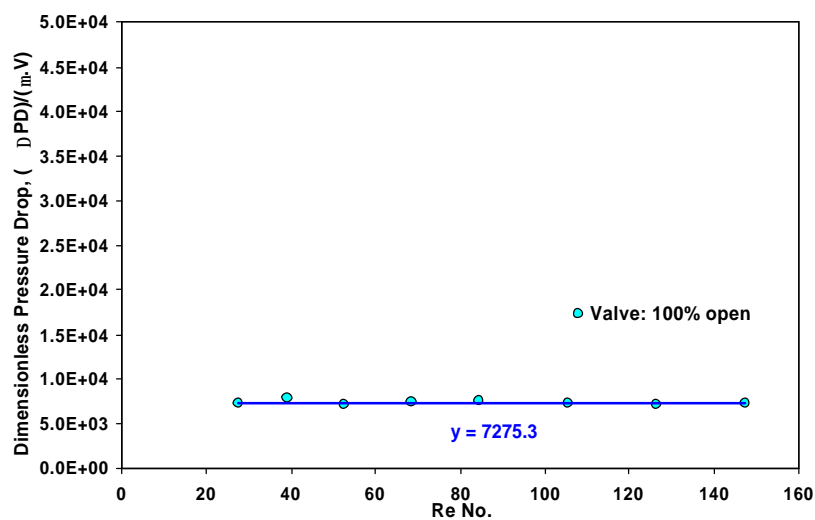


Figure 7-10 The flow loop dimensionless pressure drop versus the Reynolds number

The results are in agreement with the theory which states that for a laminar flow inside a tube at low flow rates, the connections and bends do not cause any non-linearity in the relationship.

An Analytical Model for Heat Source Performance

In the previous section, a calibration curve was obtained that established a relationship between the calculated volumetric flow rate using the thermal technique and the actual applied volumetric flow rate. However, as pointed out before, the results were obtained with water and not with HFE-7100, which is the actual working fluid for the EHD pump. Furthermore, this calibration curve depends on the ambient temperature. Therefore, if the ambient temperature varies, the calibration curve might alter as well, though the variation can be insignificant.

As a result, it was decided to develop a simple analytical model to simulate the heat transfer process from the heat source to the working liquid and ambient environment so that the calibration curves for different working liquids and environment conditions can be obtained. This analytical model is a basic 1-D model based on a thermal resistance network that does not consider the axial conduction through walls and other details. But we will see that this 1-D model provides sufficient accuracy for our purpose. The simple thermal resistance network is depicted in Figure 7-11.

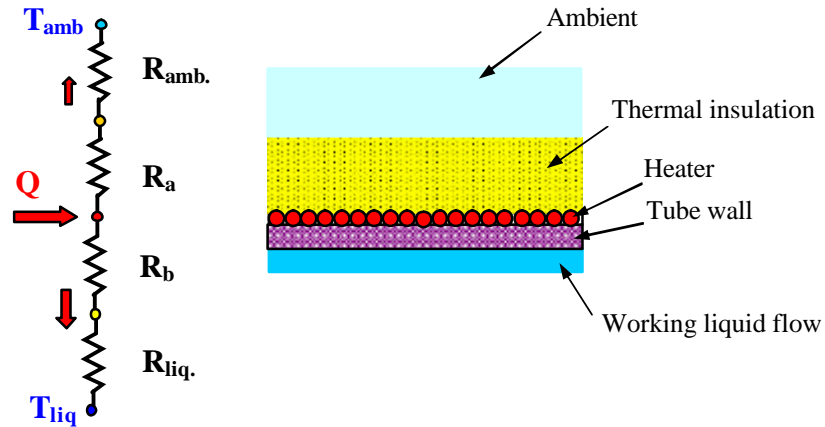


Figure 7-11 A thermal resistance network for analytical modeling

The parameters are defined as follows:

Q : Total power applied to the heater

R_a : Summation of the conductive heat transfer resistance of the insulation and its contact resistances with the heater

R_b : Summation of the conductive heat transfer resistance of the tube wall and its contact resistance with heater

R_{amb} : Convective heat transfer resistance to the ambient environment

R_{liq} : Convective heat transfer resistance to the liquid

T_{amb} : Ambient temperature

T_{liq} : Average temperature of liquid = $(T_{upstream} + T_{downstream})/2$.

Using the thermal resistance network, the percentage of the total applied heat transferred to the flowing liquid can be derived as:

$$w = \frac{\dot{m}C_p(T_{downstream} - T_{upstream})}{Q} = \frac{C_p(R_a Q + T_{amb} - T_{downstream})\dot{m}}{C_p Q(R_b + R_a)\dot{m} + Q/2}$$

(7-2)

The apparent mass flow rate is defined as the flow rate of the working liquid calculated based on the energy balance, assuming no heat loss to the ambient environment exists. This mass flow rate is given as:

$$z = \frac{Q}{C_p (T_{downstream} - T_{upstream})} \quad (7-3)$$

The relation between apparent and actual mass flow rates can be derived as:

$$z = \frac{Q(R_b + R_a)}{(R_a Q + T_{amb} - T_{upstream})} \dot{m} + \frac{Q}{2C_p (R_a Q + T_{amb} - T_{upstream})} \quad (7-4)$$

The results of this model compared to the experimental calibration results are presented in Figure 7-12 and Figure 7-13. As seen there, a good agreement between the experimental results and analytical model for water as the working liquid was obtained. In Figure 7-13, the expected calibration curve for HFE-7100 obtained by the analytical model at the same environmental condition is presented. As seen, the linear trend of the experimental data points is in agreement with the analytical relation given in Eq. (7-4).

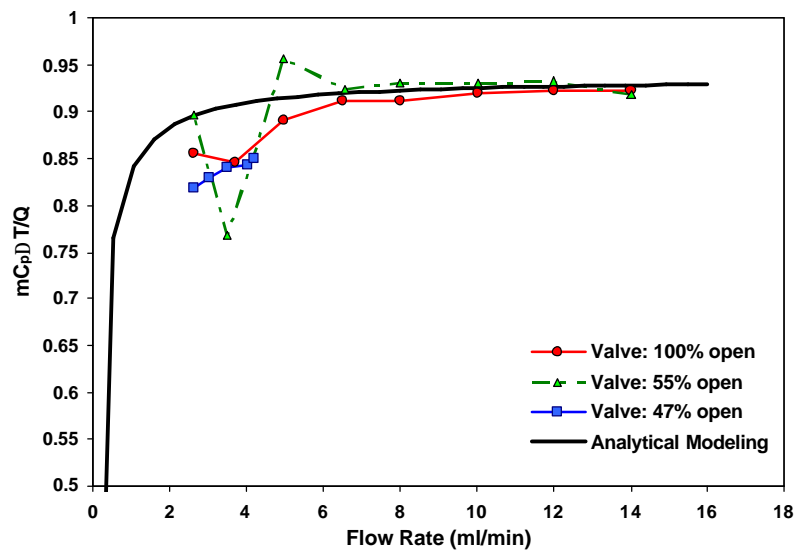


Figure 7-12 A comparison between analytical modeling and experimental results for flow measurement

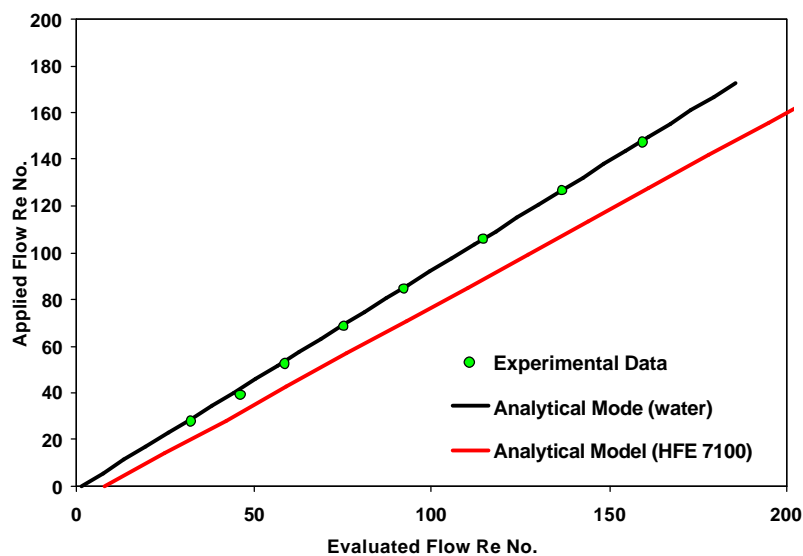


Figure 7-13 A comparison between analytical and experimental results for flow measurement calibration curve

7.2.2 EHD Pumping Experimental Results

After installing the EHD pump in the loop and charging the system with HFE-7100, electrical voltage was applied to the EHD mesopump and the pressure head and the temperature difference between the upstream and down stream of the heater was

measured. Using the calibration curves, all the quantities were calibrated. The result of the generated pressure versus the applied voltage measured by the pressure transducer is presented in Figure 7-14. As seen there, a maximum dynamic pressure head of 250 Pa was obtained. In this graph, the uncertainty of the measurement is incorporated. In the calculation of uncertainty propagation, the effects of two uncertainty components were considered, namely bias and random errors. The bias error is associated with uncertainty of the calibration technique, while the random error depends on the resolution of the measurement device.

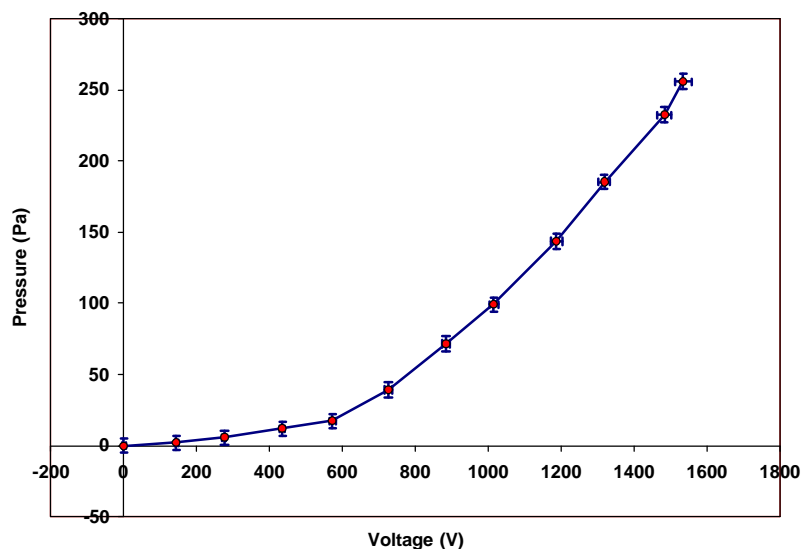


Figure 7-14 EHD pump-generated pressure versus applied voltage

The current-voltage relationship of the EHD mesopump is presented in Figure 7-15. As we can see, the current-voltage and pressure-voltage curves show similar trends. The uncertainty in the measurement of the current was relatively large. This was because the magnitude of the measured current was substantially small and was comparable to the measurement resolution of the high accuracy multimeter used for the calibration.

The variation of the generated volumetric flow rate versus the applied voltage is presented in Figure 7-16. Here two techniques were used to measure the flow rate. The first method was based on the temperature difference resulting from the fluid flow upstream and downstream of the heating source. In the second method the result of pressure head versus voltage, presented in Figure 7-14, and the relationship between pressure drop inside the loop and volumetric fluid flow, presented in Figure 7-10, were used to obtain the flow rate. Notice that the dimensionless result of Figure 7-10 is valid for both water and HFE-7100, and no correction is needed. As seen, a good agreement between two techniques was obtained. The power applied to the heating source was initially set to 0.15W. However, as the voltage increased, so did the measurement uncertainty, since the difference between the measured temperatures became smaller. Therefore, the applied power to the heating source was increased to 0.45W at a voltage of 900V.

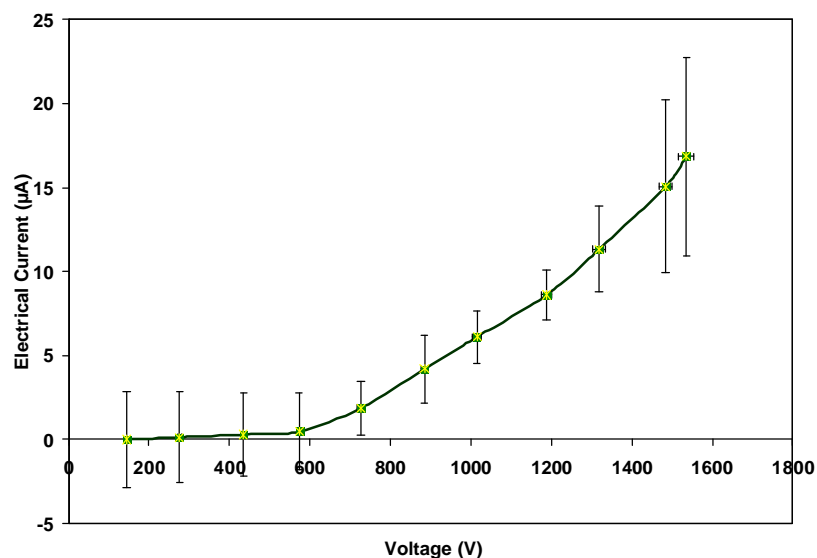


Figure 7-15 EHD mesopump electrical current versus applied voltage

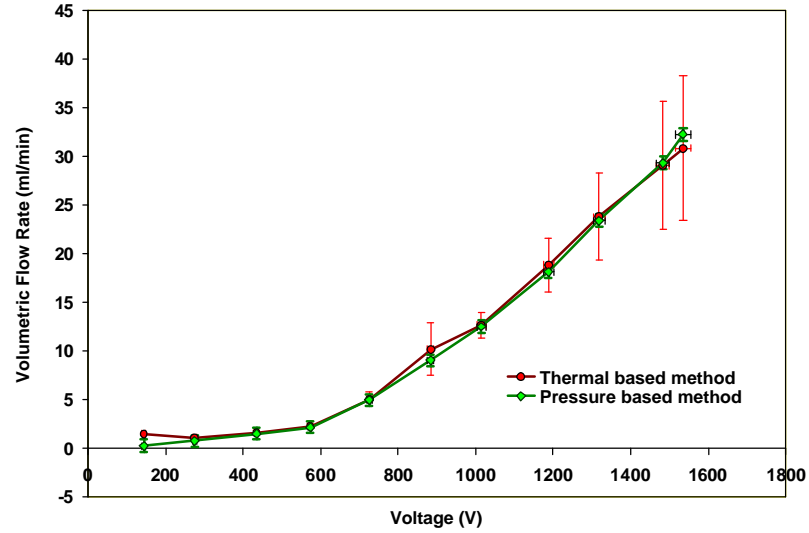


Figure 7-16 EHD mesopump volumetric flow rate versus applied voltage

We also calculated the thermodynamic efficiency of the EHD pump. The thermodynamic efficiency is defined as

$$h = \frac{\Delta P \dot{Q}}{W} \times 100$$

(7-5)

where ΔP , \dot{Q} and W are the pressure head, volumetric flow rate, and total input power to the pump, respectively. The variation of the efficiency versus applied voltage is presented in Figure 7-17.

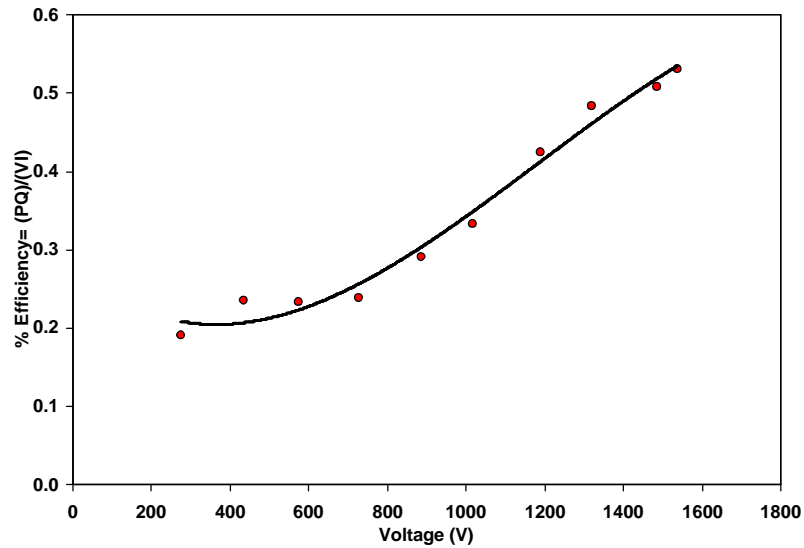


Figure 7-17 EHD mesopump efficiency versus applied voltage

As seen here, the efficiency of the EHD pump is fairly low, which is in accordance with the efficiencies of other EHD pumps reported in literature. However, this is not a major cause of concern since the total value of the input power is quite small (in the range of 0.01W). Notice that the ratio of total pump input power to the power applied to the heat source is very small. Therefore, it appears that the Joule heating effect does not cause any appreciable error in the fluid flow measurement technique.

7.3 Numerical Results

The objective of this section is to use the numerical simulation methodology that was developed to model the ion-injection pumping effect. A detailed review of the numerical modeling technique was given in Chapter 4.

Before introducing the computational domain and other modeling details, it is worthwhile to mention that a major step for the numerical simulation is the simplification of the model. In most cases, the actual natural phenomena are extremely complicated in

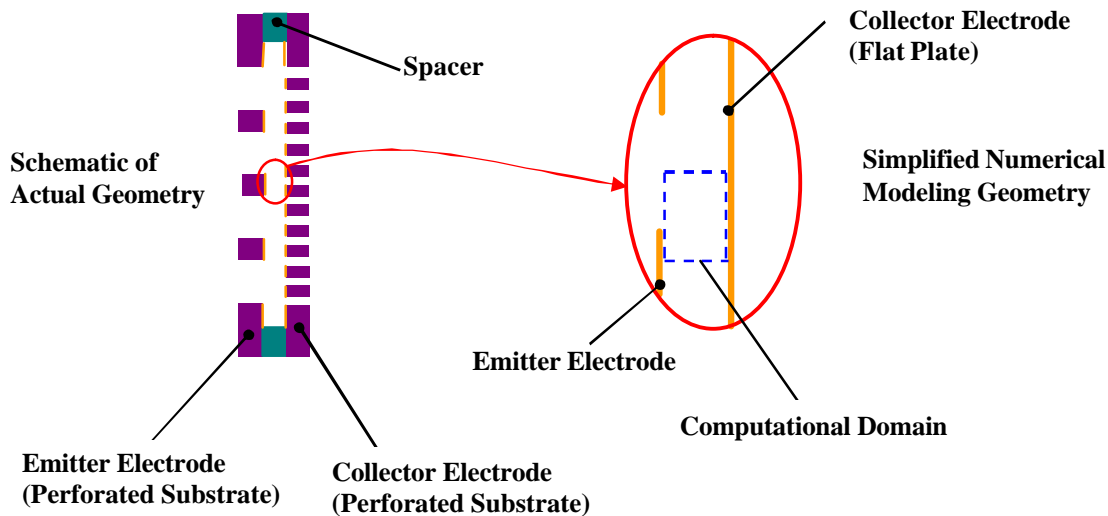
terms of the geometries and other parameters involved. Using physical/mathematical models these phenomena can be simplified and represented by a set of governing equations. However, in many cases, even further simplifications are required due to the complexity of the actual geometry that makes a numerical simulation, if not impossible, certainly computationally demanding and time consuming. These types of simplifications are implemented in the present modeling effort, which will be introduced and discussed in following sections.

7.3.1 Modeling of the Ion-Injection Mesopump

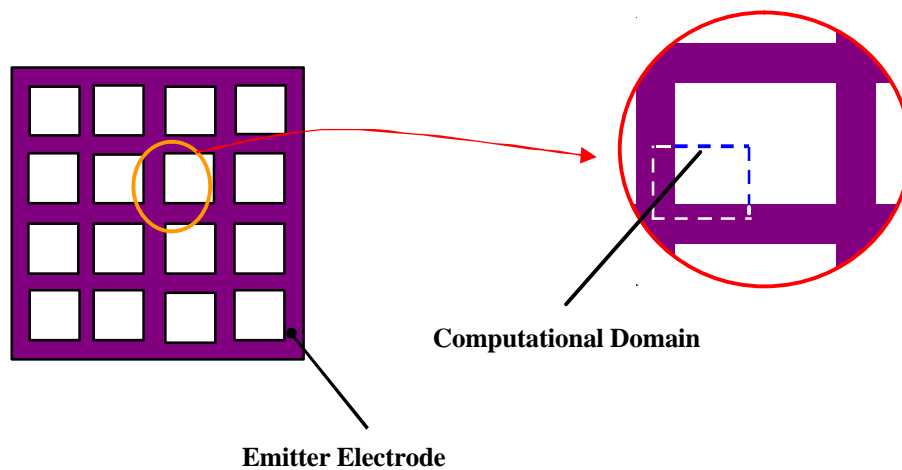
From experimental results, a relationship between the pressure head and the applied voltage for the ion-injection mesopump was obtained. In this section, the objective is to find a similar relationship using the numerical modeling technique. To do so, a number of simplifying assumptions had to be made. In spite of these simplifications, it will be shown that the reasonably accurate results can be still obtained.

To simulate the pumping process, the dissociation-injection modeling procedure was used (see Chapter 4 for a complete description of this modeling technique). In this model, not only the ion-injection process, but also the ion-dissociation and recombination processes are taken into consideration. This model allows us to simulate the process completely independently of experimental results.

Since the geometry of the mesopump is quite complicated to be considered in its entirety as the computational domain, it is necessary to simplify the modeling region. The computational domain is depicted in Figure 7-18.



(a)



(b)

Figure 7-18 Computational domain of solution: (a) side view (b) top view

As seen in this picture, only a limited region of the electrodes and the gap between them was considered as the computational domain. This allowed us to solve the governing equations with a relatively high degree of resolution and accuracy. However, the results for this limited portion were extended to the entire electrode surfaces and the gap between them.

Further simplification was also made in terms of the geometry of the collector electrode. Since our modeling procedure is based on the assumption that the collector electrode does not participate in the ion-injection process, the perforated geometry of the collector electrode was modeled as a flat plate electrode. This simplification can be justified by the fact that on the collector electrode, the sharp points on the edge of the webs are placed closer to each other than they are on the emitter. Therefore, the electric field is not significantly intensified in neighborhood of these points. Therefore, a flat plate can reasonably represent the collector electrode in numerical modeling.

Figure 7-19 shows the computational domain enclosed by various surface boundaries. For each of these surfaces the appropriate boundary condition was assigned. These boundary conditions can be summarized as follows (see Chapters 2 and 4):

$$\text{Emitter electrode: } \rho_{e.inj}^- = \frac{A\sigma_e}{(\mu_e^+ + \mu_e^-)} \cdot \frac{1}{2b K_1(2b)}, \quad \frac{\partial \rho_e^+}{\partial n} = 0, \quad \phi = -\phi_0$$

$$\text{Collector electrode: } \frac{\partial \rho_e^-}{\partial n} = 0, \quad \rho_e^+ = 0, \quad \phi = 0$$

$$\text{Symmetric and electrically insulated planes: } \frac{\partial \rho_e^-}{\partial n} = 0, \quad \frac{\partial \rho_e^+}{\partial n} = 0, \quad \frac{\partial \phi}{\partial n} = 0$$

Notice that here a negative polarity voltage was applied to the emitter electrode, while the collector electrode was grounded.

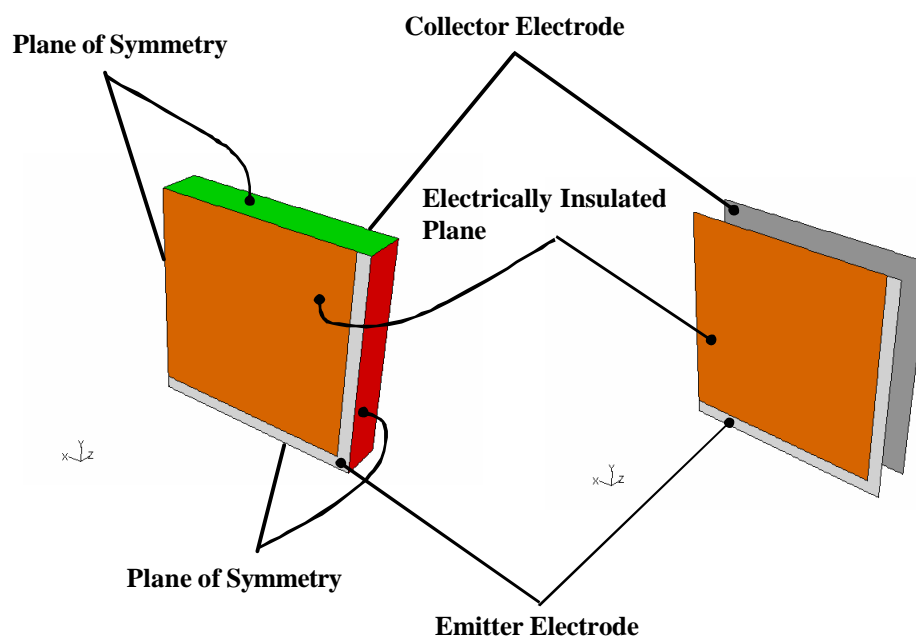


Figure 7-19 Surface boundaries surrounding the computational domain

The electrohydrodynamic governing equations for the dissociation-injection process were given in Chapter 4. As shown there, in general, electric and fluid flow governing equations are coupled through the fluid velocity field. On the other hand, the velocity of the liquid passing through the mesopump depends not only on the mesopump performance but also on the pressure drop of the rest of the loop. This means that an appropriate fluid flow velocity boundary condition for the computational domain cannot be assigned simply because the relation between the pressure drop and fluid flow must be known in the rest of the loop. However, it is still possible to calculate the maximum pressure head of the mesopump (i.e. the static pressure head). In fact, the pressure head of the mesopump reaches its maximum when the mesopump does not deliver any flow to the rest of the loop. This corresponds to the case where the outlet of the mesopump is

hypothetically obstructed so that the pump essentially generates a static pressure head. For this case, it can be assumed that the liquid velocity is zero. Therefore, in the absence of the liquid flow, the maximum static pressure can be calculated from the following equation:

$$\nabla p = (\rho_e^+ - \rho_e^-) \mathbf{E} \quad (7-6)$$

In order to solve the governing equations, various input parameters of numerical code were assigned as given in Table 7-1, and the computational domain was divided into 176,400 hexahedral cells.

Table 7-1 Value of input parameters

Parameter	Value	Parameter	Value
Liquid dielectric constant, ϵ_s	7.4	Liquid electrical conductivity, σ_e (S/m)	2.6×10^{-8}
Liquid positive and negative ion mobilities, μ_e^+, μ_e^- ($\text{m}^2/\text{V.s}$)	3.44×10^{-8}	Voltage, ϕ_0 (kV)	0 to -2000
Density, ρ (kg/m^3)	1470	Liquid viscosity, μ ($\text{kg}/\text{m.s}$)	6.5×10^{-4}
$A\sigma/(\mu_e^+ + \mu_e^-)$, (Q/m^3)	0.33		

A comparison of the numerical model and experimental results for the generated pressure versus the electrical voltage is presented in Figure 7-20. As seen in this figure, overall an acceptable agreement between numerical model and experimental results was obtained, with the numerical model approximately predicting the trend of pressure variation with the applied voltage. There are two main reasons for the observed difference. The first is the fact that in spite of the complexity of the governing equations and numerical simulation procedure, this was still a quite simplified model for the actual EHD process involving the electrochemical reactions and ions interactions. Moreover, a

simplified modeling geometry was used to represent the actual ion-injection mesopump. Also, as was pointed out earlier, in this modeling procedure the maximum static pressure head was calculated where no liquid flow was assumed, but the experimental data was obtained when a liquid flow through the mesopump existed. As a result, it is expected that the measured pressure will be less than the maximum calculated pressure.

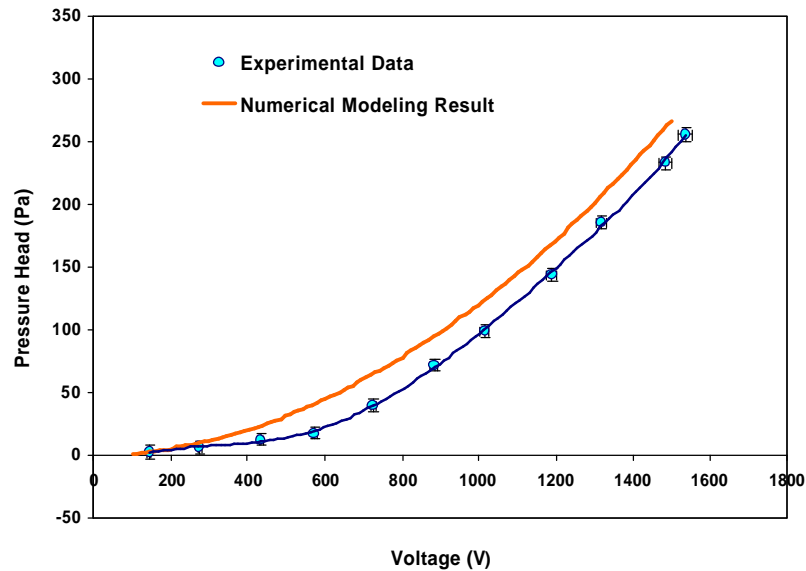


Figure 7-20 Numerical modeling and experimental results for the static pressure versus voltage

Using the numerical model it is also possible to calculate the electrical current passing through the liquid. For a static liquid, the current can be found by Eq. (7-7)

$$I = \int \mathbf{J} \cdot d\mathbf{A} = \int (\mu_e^+ \rho_e^+ - \mu_e^- \rho_e^-) \mathbf{E} \cdot d\mathbf{A} \quad (7-7)$$

where the integral is calculated on any arbitrary surface between two electrodes. Notice that as discussed earlier, only one element of the whole mesopump geometry was considered as the computational domain. Therefore, the calculated current for this element was multiplied by the number of elements to find the total electrical current. The modeling result compared to the experimental data is presented in Figure 7-21.

As seen here, the experimental and numerical results show a different trend. While the measured current displays an exponentially growing trend, the numerical current shows nearly a linear trend. To understand the source of this difference, some factors should be recalled. First, as shown in Figure 7-15, the margin of measurement error for electrical current was relatively large because the magnitude of the measured current was substantially small and was comparable to the measurement resolution of the high accuracy multimeter used for the calibration. Therefore, some uncertainty is associated with the value of the experimental data for the electrical current.

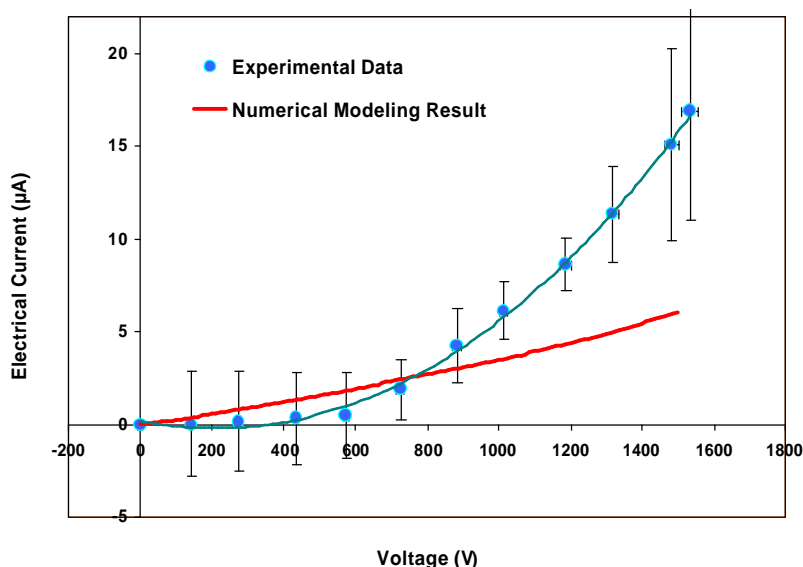


Figure 7-21 Numerical modeling and experimental results for the electrical current versus voltage

Secondly, since for the pressure head an acceptable agreement between the numerical and experimental results was observed, it can be concluded that the difference between the electrical current results might be associated with the dissociation component rather than the injection component of the current. Notice that only the injection part of the current results in a pumping action, and the dissociation part of the current either does not affect the pumping action or, in special geometries of the electrodes, causes a flow in the

reverse direction (known as conduction pumping). Therefore, the current model might not accurately calculate the dissociation part of the current. Moreover, notice that this component of the total electrical current is very sensitive to the presence of impurities. A small amount of impurities can substantially change the dissociation component of the current. The other explanation for this difference is that in our simple model the effect of the sharp edges of the electrode webs was not taken into account. These edges can intensify electric field locally and promote the ion injection process that increases the electrical current. Finally, this model was developed for nonpolar liquids. The dielectric constant (or permittivity) of nonpolar liquids is relatively low. For example, for liquid nitrogen the dielectric constant is about 1.43. Conversely, the dielectric constant of polar liquids is quite high. For example, for water the dielectric constant is about 80. As a result, HFE7100 can be considered a semi-polar liquid because it shows polar liquid characteristics to some extent. Therefore, the current model might not fully describe the behavior of this liquid under the effect of electric field.

The distribution of the dimensionless potential and positive and negative charge densities in the gap space between electrodes is presented in Figure 7-22 to Figure 7-24. Notice that the computational domain is only one fourth of the displayed region in these figures (see Figure 7-19). The dimensionless potential and positive and negative charge densities are defined as follows:

$$\begin{aligned}\phi^* &= \frac{\phi}{-\phi_0} \\ [\rho_e^+]^* &= \frac{\rho_e^+}{\sigma/(\mu_e^+ + \mu_e^-)} \\ [\rho_e^-]^* &= \frac{\rho_e^-}{\sigma/(\mu_e^+ + \mu_e^-)}\end{aligned}$$

The results were obtained using HFE-7100 properties and $\phi=1000$.

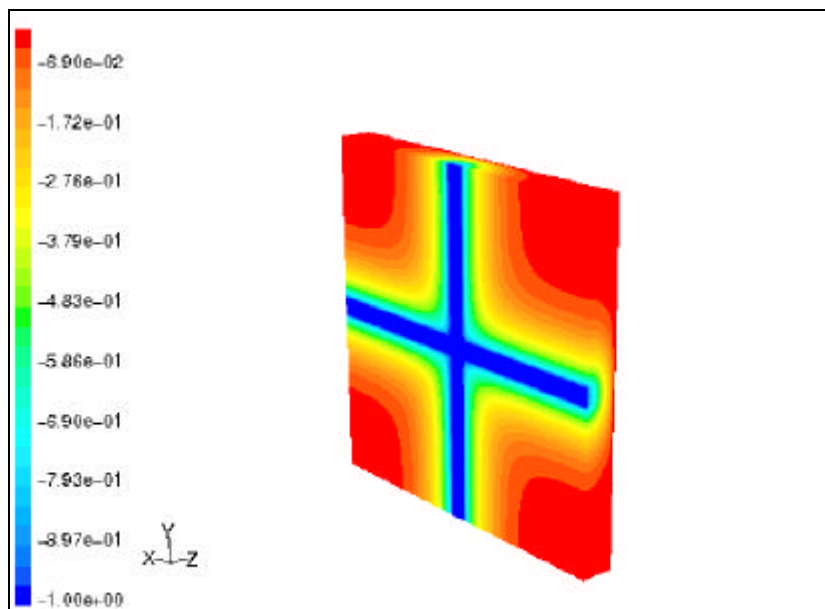


Figure 7-22 Distribution of the dimensionless electrical potential

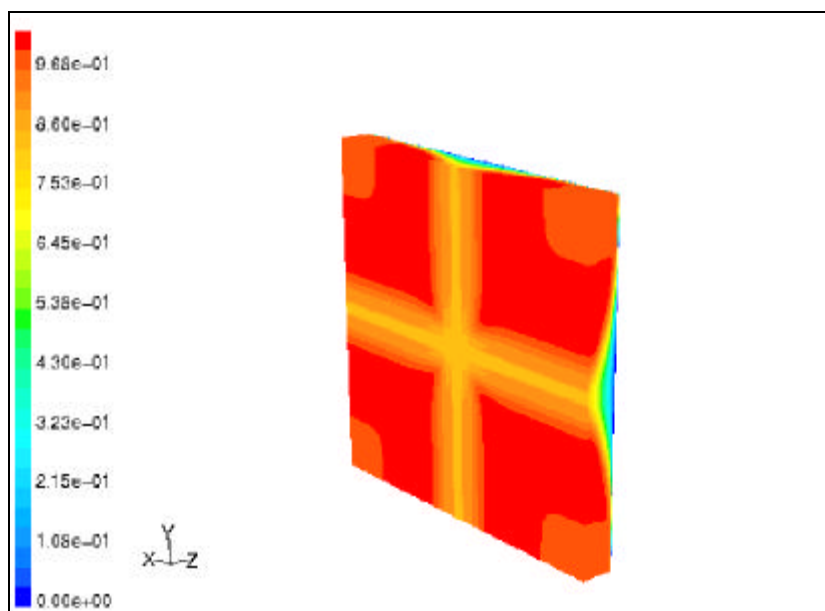


Figure 7-23 Distribution of dimensionless positive charge density

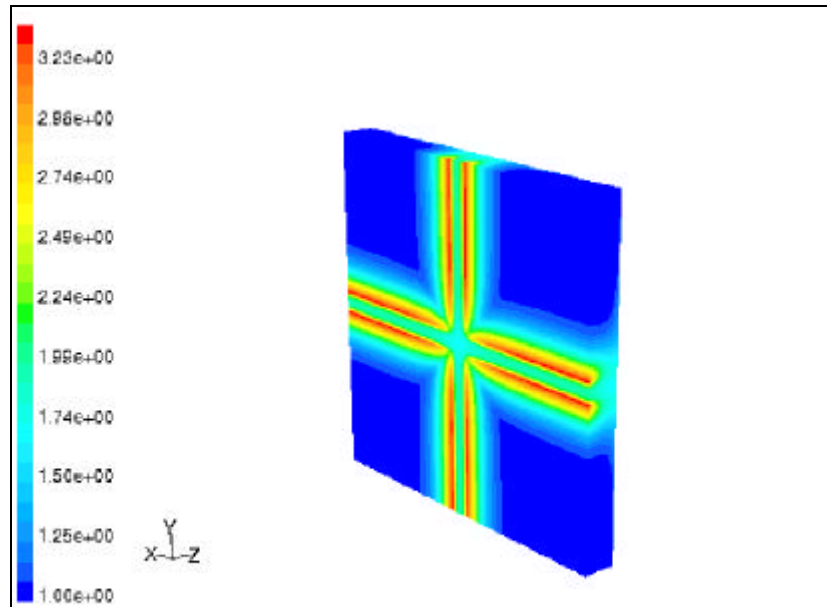


Figure 7-24 Distribution of dimensionless negative charge density

7.3.2 Design of Multi-stage Mesopump Using the Numerical Modeling

In the previous section the experimental and numerical results were compared. In this section the objective is to demonstrate that this numerical model can serve for further improvement of the ion-injection mesopump.

As shown in Figure 7-14, the present design of the ion injection mesopump was able to produce a maximum pressure about 260 Pa. However, in many applications for this type of pump a higher pressure drop in the system is expected. For example, our study has shown that for a two-phase, small scale, cooling loop consisting of a miniaturized evaporator, condenser and pump, a pressure drop of about 1 kPa is expected to dissipate 50W heat. Therefore, the question is how the pumping head can be improved. One answer is to use multistage electrodes for the mesopump. Multistage electrodes are arrays of electrode pairs that are placed in series. Each electrode pair, consisting of an

emitter and a collector, bumps up the pressure and drives the liquid to the next stage. A schematic of a three-stage ion-injection pump is depicted in Figure 7-25.

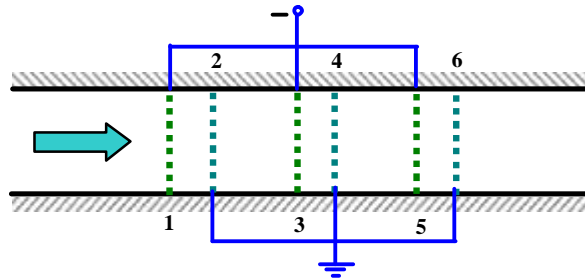


Figure 7-25 Schematic of a three-stage ion-injection pump; Electrodes 1, 3 and 5 are emitters and electrodes 2, 4 and 6 are collectors.

The important factor in the design of a multistage pump is the distance between two successive stages. To understand the importance of this parameter, again consider Figure 7-25. Here, not only electrodes 1 and 2, but also electrodes 2 and 3 form a pair of emitter and collector electrodes. Since electrodes 1 and 2 are acting as the emitter and collector, respectively, the pumping force direction because of these two electrodes is from left to right. However, for electrodes 1 and 3 the pumping force direction is the opposite, i.e. from right to left, since here, the emitter is electrode 3 and the collector is electrode 2. As seen in this picture, the distance between electrode 1 and 2 is less than the distance between electrode 2 and 3; therefore, the pumping force due to the electrode pair of 1 and 2 is stronger than the pumping force of the electrode pair of 2 and 3. As a result, the net pumping force direction is from left to right.

Now the question is what the optimum distance between two successive stages is. Obviously, the pumping head increases if the two successive stages get farther from each other. But in practical situations, there is generally a restriction on the total length of the pump. In this case, if the distance between the successive stages increases, the total

number of electrode pairs reduces. Therefore, it is likely that an optimum distance exists. Here, the objective is to find this optimum distance using numerical modeling.

To simulate this problem, a number of simplifying assumptions need to be made.

These assumptions are listed as follows:

- The emitter and collector electrodes are modeled as flat plates;
- Each electrode only interacts with the next electrode; therefore, there is no interaction between, for example, the first and the fourth electrodes;
- The problem is one-dimensional;
- There is no liquid flow and the total pressure head generated is static pressure;
- All other assumptions made in the development of the numerical modeling procedure are still valid.

A simple model for this problem is depicted in Figure 7-26. In this model three electrodes, consisting of two emitter electrodes (E_1 and E_2) and one collector electrode (C_1), are taken into consideration. The objective is to find the optimum value of $x = S/L$. Notice that for $x=1$, no net pumping is expected since the effect of the E_1-C_1 electrode pair counterbalances the effect of the E_2-C_1 electrode pair. In this problem it is assumed that in the electric field between two electrodes, no electrode, other than these two electrodes, has any effect.

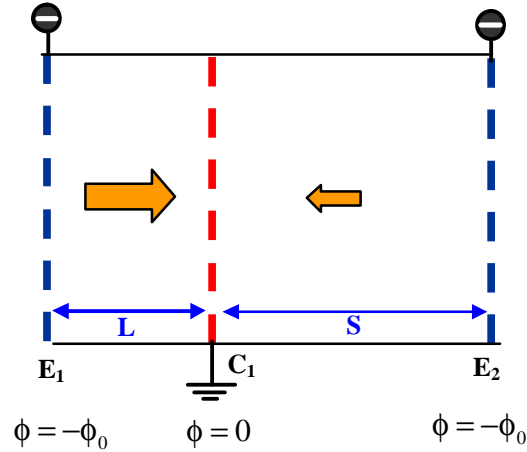


Figure 7-26 Numerical model consisting of two emitter electrodes (E_1 , E_2) and one collector electrode (C_1)

The governing equation and boundary conditions of this problem are presented in Chapter 4. To generalize the solution of this problem, it is more suitable to present the solution in its dimensionless form. Based on the governing equations and boundary conditions presented in Chapter 4, it can be shown that the governing dimensionless parameters for this problem are as follows:

$$\gamma = \frac{\mu_e^+}{\mu_e^-}, \quad A = \frac{\rho_{e,inj}^0}{\sigma_e / (\mu_e^+ + \mu_e^-)}$$

$$C_0 = \frac{s_e L^2}{(\mu_e^+ + \mu_e^-) e \phi_0}, \quad C_0 \bar{b}^2 = \frac{s_e L^2}{(\mu_e^+ + \mu_e^-) e \phi_0} \cdot \left[\frac{e_0^3}{16\pi\epsilon k^2 T^2} \frac{\phi_0}{L} \right] \quad (7-8)$$

where γ is a dimensionless parameter representing the ratio of mobilities of the positive and negative ions, A is a ratio of the ion density at the emitter electrode and the ion density in the bulk at the thermodynamic equilibrium. C_0 is another dimensionless parameter called the residual conductivity parameter. Notice that $C_0^{-1} \propto \phi_0$. $C_0 \bar{b}^2$ is a parameter that is independent of the electrical potential and constant for a given liquid with a fixed electrode spacing.

It can be shown that C_0 and $C_0\bar{b}^2$ are related to the primary dimensionless parameters given in Table 2-1 based on the following relations:

$$C_0 = \frac{E_{hd}}{\epsilon_s Md}$$

$$C_0\bar{b}^2 = \frac{1}{16\pi} \left(\frac{Db}{\epsilon_s} \right)^2 \cdot \frac{e_0(\mu_e^+ + \mu_e^-)}{\sigma_e L^3} \quad (7-9)$$

For modeling of this problem it was assumed that $\gamma = 1$ and $A=1$, as suggested by (Pontiga and Castellanos 1996). The other input parameters are given in Table 7-2.

Table 7-2 Modeling input parameters

Parameter	Value	Parameter	Value
Liquid dielectric constant, ϵ_s	7.4	Liquid electrical conductivity, σ_e (S/m)	2.6×10^{-8}
Liquid positive and negative ion mobilities, μ_e^+, μ_e^- ($m^2/V.s$)	3.44×10^{-8}	Voltage, $-\phi_0$ (kV)	-1000
L (m)	250×10^{-6}	Temperature (K)	298

Thus, the other dimensionless parameters can be calculated as

$$C_0 = 0.3607 \quad C_0\bar{b}^2 = 0.1061$$

The result of numerical modeling is presented in Figure 7-27. The definitions of the variables which are indicated in this figure are as follows:

$$P^* : \text{Dimensionless pressure defined as } P^* = \frac{P}{P_0}, \text{ where } P_0 = \rho \left(\frac{\mu_e^+ \phi_0}{L} \right)^2$$

ΔP^* : Total pressure head generated between electrodes E_1 and E_2

S: The gap between electrode C_1 and electrode E_2 (see Figure 7-26)

L: The gap between electrode C_1 and electrode E_1 (see Figure 7-26)

x: the gap ratio = S/L

$\Delta P^*/(1+x)$ Total pressure head over total length given in dimensionless form

ΔP_o^* : Pressure head generated between electrode E_1 and electrode C_1

$\Delta P^*/\Delta P_o^*$: Ratio of the total pressure head to the pressure head generated by one pair of the emitter and the collector (i.e. E_1 and C_1)

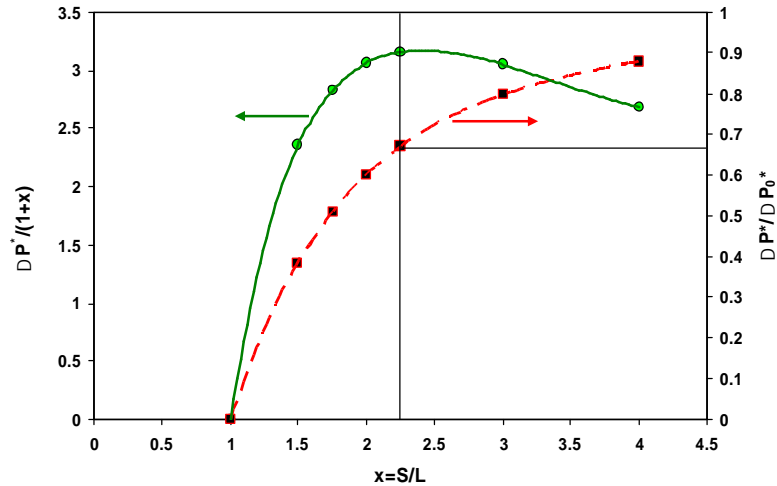


Figure 7-27 Numerical modeling results of the dimensionless pressure head per total length (left) and pressure head ratio (right) versus $x=S/L$

Figure 7-27 shows that as the gap between electrode E_2 and C_1 increases, the effect of the backward pumping decreases and the pressure ratio $\Delta P^*/\Delta P_o^*$ approaches unity. Therefore, if there is no restriction on the total length of the pump, an increase in the distance between two successive stages is desirable. However, if the objective is to maximize the pressure head for a given length of the pump, then the ratio of $\Delta P^*/(1+x)$ should be maximized. As seen, the peak of the curve corresponds to the gap ratio of 2.25. For this gap ratio, the pressure ratio is about 0.67, which means that a two-stage pump with an optimum gap ratio can generate a pressure head 67% higher than a single-stage pump.

Now the question is whether this optimum gap ratio depends on the applied voltage. Our result showed that for an increase of 50% in the applied voltage, a significant variation in the optimum point was not observed. The result of this investigation is presented in Figure 7-28. Therefore, it can be concluded the obtained result is independent of the applied voltage.

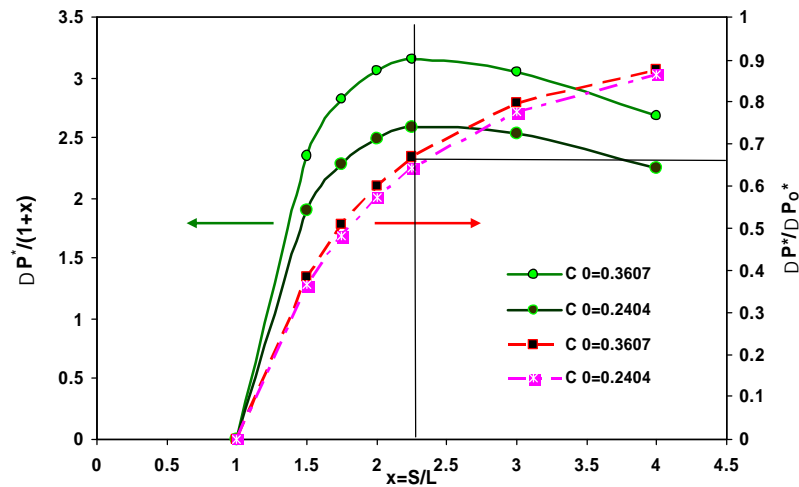


Figure 7-28 Numerical modeling results of the dimensionless pressure head per total length (left) and pressure head ratio (right) versus $x=S/L$ for two different voltages $f_0=1000$ ($C_0=0.3607$) and $f_0=1500$ ($C_0=0.2404$)

In order to use these results to improve the pumping pressure head of the mesoscale pump, some issues need to be taken into consideration. As pointed out in Chapter 5, the thickness of the electrode substrate and the gap between the electrodes were $525 \mu\text{m}$ and $250 \mu\text{m}$, respectively. Therefore, if we want to increase the pressure head by adding multiple stages, the minimum distance between two successive stages (i.e. S) cannot be less than twice the substrate thickness (i.e. $1050 \mu\text{m}$) where two electrode substrates come into contact from the back side. As a result, the optimum gap size between two successive stages cannot be implemented unless the fabrication is

performed with thinner wafers. However, with $S/L= 1050/250$, it can be shown that a five-stage mesopump can produce a total pressure head of 1200 Pa for a total length about 5250 μm . If a 250 μm thick wafer is fabricated, it can be shown that using the optimum S value, about the same pressure head can be obtained for a mesopump with a total length of 4000 μm .

7.4 Summary

In this chapter the static pressure and flow rate results of the experiments conducted on the ion-injection mesopump were presented. It was shown that the two flow rate measurement methods based on a heat balance technique yielded consistent results. The maximum measured pressure and flow rate were about 270 Pa and 30 ml/min for an applied voltage of 1500V. A numerical simulation was also conducted to model the maximum pressure head of the mesopump. The numerical pressure head result showed acceptable agreement with the one obtained from experiments. However, a difference between the numerical and experimental currents was noted for which the possible causes were discussed. It was also demonstrated how that the numerical modeling can be used to improve the generated pressure head by adopting multistage electrodes.

CHAPTER 8: CONCLUSIONS AND RECOMMENDATIONS FOR FUTURE WORK

8.1 Introduction

This chapter summarizes the results of this study and provides a number of recommendations to continue this investigation as future work to further develop knowledge in the subject matter. An overview of the previous chapters clearly indicates that the current study involved contributions to the advancement of knowledge in the present study field through three specific research tasks, namely: numerical modeling; experimental study; and microfabrication. Naturally, the recommendations will be also divided into categories associated with each discipline.

8.2 Overview and Conclusions

It is worthwhile to summarize here some of the achievements of this study and to highlight the corresponding conclusions of the present research.

- Relevant theoretical fundamentals of electrohydrodynamics were presented, and the governing equations and boundary conditions were introduced.
- A literature survey on the different types of EHD pumping concepts in general and on ion-injection pumping in particular was performed. A comparison among a number of different ion-injection pumps was provided based on parameters viewed of practical significance in a tabular format.

- A methodology for the numerical solution of the governing equations was developed, and a user-defined routine was created that was used in conjunction with the Fluent[®] CFD code to model the interaction of the electrical and hydrodynamic fields. Standard benchmark problems were carefully studied to validate the numerical solution results, and the numerical results were compared against available experimental results.
- The design requirements for an ion-injection mesopump were identified, and based on those requirements a preliminary pump was designed and fabricated.
- Once the preliminary device demonstrated the applicability of the electrode design for the concept, a mesoscale ion-injection pump with micro fabricated electrodes was designed and fabricated.
- A detailed, step-by-step, description of the developed micro fabrication process was presented.
- A flow loop was built to measure the pressure head and the fluid flow rate delivered by the pump. The relevant instruments were also discussed.
- Two techniques based on the heat balance and pressure measurements were developed to measure the volumetric fluid flow rate.
- Upon careful calibration of the instrumentation and the flow loop, the experiments were successfully conducted to measure the extremely small flow rates generated by the mesopump inside the loop. The results based on two different measurement techniques showed good agreement.
- It was demonstrated that the mesopump was able to produce a pressure head of about 250 Pa at a flow rate of 30 ml/min for a voltage of 1600kV and thermo-

hydro-dynamic efficiency of 0.55 %. The measured electrical current at this voltage was about 17 μA .

- A numerical model was developed to simulate the generated pressure head of the pump. The result of this model showed an acceptable agreement with that from the experiments.
- The numerical model was used to demonstrate how the generated pressure head can be increased using a multistage mesoscale pump. An appropriate distance between the two successive stages was presented.

The present research is novel in that to the best of author's knowledge, this is the first work that investigates numerical modeling and simulation of the very complex interaction of the ion injection-dissociation phenomenon with fluid flow and compares the model with experimental results. A few studies on the interaction of either the ion dissociation or ion injection process with the fluid flow have been reported, but none of them has taken into account the combined effect of these two processes on the fluid. On the other hand, there are a few other reported works in which the combined effects of the ion dissociation and ion-injection processes were modeled. But in these studies the interaction with the fluid flow was not considered and numerically simulated. In fact, these studies were restricted to finding only the current-voltage relation and did not include modeling the fluid flow interaction with the electric field.

Designing instrumentation and measurement techniques for the small scale systems is a critical task because the errors could be quite significant. As a result, not only each instrument, but also the whole system with the instruments in place must be calibrated carefully. Therefore, another contribution of this study was successful

calibration and instrumentation of the loop to accurately measure the extremely small flow rates.

Perhaps a major contribution of this study to the advancement of the field in this area is the fact that present study demonstrated the complexity and challenge associated with numerical and experimental research of the electrohydrodynamic phenomenon on a miniaturized scale. Moreover, from practical significance view point, EHD in microscale seems to be the area where future research with commercial interest will focus.

8.3 Recommendations

Since in this study various research fields were involved, the recommendations can also be classified in different divisions.

8.3.1 Recommendations for Numerical Modeling

- **Model the interaction of the dielectrophoretic and electrostrictive forces and two-phase fluid flow.**

As documented in Chapter 2, the electrohydrodynamic body force consists of three components: electrophoretic, dielectrophoretic, and electrostrictive. In the current study, the interaction of the electrophoretic force (also known as the Coulomb force) and the single phase fluid flow was numerically modeled. In fact, in a single-phase fluid flow the effects of the other two EHD force components are generally negligible. However, in a two-phase fluid flow where the interface is under the influence of a nonuniform electric field, these two force components become important. As an extension of the current numerical study, the modeling of the dielectrophoretic and electrostrictive forces and their interaction for a two-phase fluid is proposed. Applications of this numerical

simulation may include the tracking of the bubbles moving under influence of the electric field, EHD-enhanced condensation, and polarization pumping. Some preliminary work on this modeling has already been performed by the author using the volume of fluid (VOF) numerical modeling technique. In order to understand this technique, consider a two-phase fluid flow consisting of phase A and phase B. In the VOF modeling technique, besides conventional governing parameters such as velocity and pressure, another parameter called volume fraction, F , is taken in to consideration and computed. This parameter represents the portion of a computational cell that is filled with a particular fluid phase. For example, if $F=1$ for a specific cell, it means that that cell is filled with one phase, say phase A. Conversely, if $F= 0$, then that cell is filled with phase B. If $0<F<1$ for a computational cell, it can be concluded that the interface is passing through that cell. Now, the permittivity at any point of a two-phase flow can be calculated in terms of the volume fraction at that point as follows:

$$\varepsilon = F\varepsilon_A + (1-F)\varepsilon_B \quad (8-1)$$

where ε_A and ε_B are the permittivity of phase A and phase B, respectively. Now, knowing the value of F at any point, the permittivity gradient can be calculated as follows:

$$\nabla\varepsilon = (\varepsilon_A - \varepsilon_B)\nabla F \quad (8-2)$$

Notice that $\nabla\varepsilon$ must be determined to calculate the dielectrophoretic force component (see Chapter 2). The electrostrictive force component can also be calculated in terms of volume fraction, F . Therefore, if F is known, the EHD body force can be computed. On the other hand, this body force changes the fluid flow field, which in turn alters the

volume fraction field indirectly. This leads to a movement of the interface toward a region of higher intensity in the electric field.

Further research on this method will provide greater detail on this numerical approach. The author believes that the proposed modeling is challenging and is very useful contribution to accurate modeling of the EHD flow field.

- **Develop a numerical technique that uses two different computational grids for the electrical and fluid flow fields.**

One issue in the current numerical model arose when using the same computational grid for both the electric and fluid flow fields. In fact, these two fields are different in nature. There are some circumstances for which a high-resolution computational grid is needed in certain portions of the computational domain for one of these fields, while for the other field such a need does not exist. However, since the discretization of the governing equations for both of these fields is implemented on the same computational grid, the computational run time may be very high.

To explain this issue more fully, consider an example where a gaseous corona wind flow issuing from a wire electrode strikes a flat plate. Let us assume that the flow velocity is relatively low, so that the velocity field does not influence the charge density distribution (see Chapter 4). In the vicinity of the wire electrode (i.e., the emitter), the electric field varies sharply, while around the plate (i.e., the collector) it changes gradually. Conversely, the variation of the fluid flow pattern around the plate is quite steep, as the flow direction changes from a normal to the plane to a parallel along it. Therefore, if we want to numerically model this problem, a dense grid should be generated around both the wire and the plate to capture the sharp electric field variation

and steep velocity gradient. However, when the governing equations for the electrical domain are solved, a refined grid around the plate is not needed and can increase the calculations load and time run.

To solve this problem and similar cases, it is recommended to develop a modeling technique such that two different computational grids can be used for different domains. In this technique, the solution for one of the fields should be mapped onto the grid of another field using interpolation techniques. The methodology can be quite similar to the one used in a multigrid solution technique. This solution mapping technique could be computationally costly and time-consuming due to the necessary calculations, but the costs are justified, as this technique could be used for many problems, such as the above example where the velocity field does not influence the electric field. In that case, first, the electrical equations could be solved independently of the velocity field. Next, the solution mapping could be carried out, and then velocity field governing equations could be iteratively solved.

- **Track particles moving under the influence of electric field**

In addition to solving transport equations for the continuous phase, it would be quite helpful to simulate a discrete second phase in a Lagrangian frame of reference and subject to an electric field. This second phase may consist of spherical particles (which may be taken to represent solid objects, droplets, or bubbles) dispersed in the continuous phase. As a result of the electrostatic force, the trajectory of these particles can change. Therefore, calculation of the position of the particles and tracking their movement could be an interesting research topic. Applications for this numerical modeling procedure might include tracking of oil droplets carried with a refrigerant stream inside an EHD-

assisted oil separator unit; or tracking of seeding particles used in the Laser Doppler Velocimetry (LDV) technique to measure corona wind velocity (see Chapter 4). In this class of problems, again the EHD body force components are applied to the particles. For solid particles, the electrostrictive force is negligible, while for droplets and bubbles, both electrostrictive and dielectrophoretic forces must be taken into consideration. The problem can become more complicated if the charge accumulation effect is present as well. In this case the electrophoretic force must also be considered.

8.3.2 Recommendations for Fabrication of EHD Mesopump

- **Deep reactive ion etching to microfabricate the silicon perforated pattern**

As discussed in Chapter 5, to fabricate the perforated pattern of the electrode, anisotropic silicon wet etching technique was used. However, this process consists of several microfabrication steps, making it quite time-consuming. Moreover, anisotropic silicon wet etching resulted in the sloped side walls of perforations, which might not be an attractive characteristic of this technique as it limits the size of these holes.

Now the question is, can silicon be replaced with any other material? The other candidates for the substrate material would be metal, ceramic, plastic, and glass. As was pointed out in Chapter 5, a metallic substrate can cause backward ion-injection, thereby negatively affecting the pumping action. For the other choices, a comparison with silicon in terms of cost, ease of creating a metal electrode layer, and machinability (i.e., creating holes or perforations) is given in Table 8-1.

Table 8-1 A comparison of choices of substrate materials

Substrate	Cost	Metallization	Machinability
Ceramic	Medium	Fair	Poor
Plastic	low	poor	Fair
Glass	Low	Good	Poor
Silicon	High	Good	Very good

From (Madou 2002)

As indicated in Table 8-1, the superiority of silicon compared to other materials is associated with its machinability and ease of metallization. Considering the geometric dimensions and necessary tolerances achievable in fabricating the present electrode design, it might still be possible to replace the substrate material with one of the other choices, such as ceramic. However, it is believed that a better solution would be a reduction in the necessary number of microfabrication stages for the silicon substrate. To reduce the number of stages, it is proposed that instead of the silicon wet etching, deep reactive ion etching (DRIE) be used. DRIE is a high aspect ratio, deep trench silicon etching process. The principle of the deep trench silicon etching process is a combination of an alternating fluorine-based etching and chemical passivation of the structures (see (Madou 2002; Franssila 2004)). Compared to RIE, DRIE dry etching has a significantly higher etch rate (1.5-4 $\mu\text{m}/\text{min}$) and achieves an aspect ratio as high as 20-30. Since the desired aspect ratio in the present electrode design is less than 3, using the DRIE technique is quite appropriate. If this microfabrication technique is implemented, there is no need to etch the wafer from the backside of the wafer (see Chapter 5). As a result, the number of microfabrication stages can effectively be reduced.

- **Mesopump packaging using anodic bonding**

As discussed in Chapter 5, the present packaging technique employs a quick-dry epoxy adhesive to secure the electrodes and wafer inside the housing. However, using adhesives to packaging the mesopump is not generally a favorable solution. This is because over a period of time, these adhesives may chemically interact with the working liquid, thereby changing the liquid relevant properties. Besides, de-gassing and gradual degradation are other problems associated with these types of adhesives. Also, if a layer of adhesive penetrates between the electrode and the Pyrex[®] spacer, it may cause the gap between electrodes to be changed.

An alternative solution to the use of epoxy adhesive is anodic bonding. Anodic bonding is a simple process that joins a bare silicon wafer and a sodium-containing glass substrate such as Pyrex[®] (see (Maluf 2000) for a description of anodic bonding). This bonding method allows us to directly join the Pyrex spacer to the electrode substrates. However, before accomplishing this packaging process, some additional steps would be necessary. For example, the nitride and oxide layers need to be removed to provide a direct contact between the silicon substrate and Pyrex[®] surfaces.

8.3.3 Recommendations for EHD Mesopump Experimental Test Conditions

- **Experimental tests with other dielectric fluids**

In Chapter 6, the characteristics of HFE 7100[®] were reviewed. As pointed out there, HFE 7100 exhibits favorable electrical properties such as relatively high electrical permittivity and moderate electrical conductivity. Additionally, in contrast to many other refrigerants, it has a relatively high boiling temperature and can be used at atmospheric pressure. However, two major problems with this liquid were noted. First, HFE 7100

suffers from relatively poor heat transfer properties. Secondly, there is evidence suggesting that this liquid might irreversibly decompose under the effect of a high electric field. This evidence is supported by the non-repeatability of experimental results that was observed from time to time. An explanation for this phenomenon may lie in the molecular structure of this liquid. HFE-7100 and many other similar refrigerants have complex molecular structures with several atomic bonds. Therefore, a strong electric field might cause a rupture in these bonds, resulting in chemical decomposition of the liquid. On the other hand, a review of the electrical properties of liquids with simple molecular structures shows that they generally have relatively low electrical permittivity. In fact, it can be shown that for a wide class of liquids, the electrical permittivity is directly proportional to the polarizability of the molecule (see (Schmidt 1997; Castellanos 1998)). On the other hand, the molecular polarizability is generally higher for larger molecules. Therefore, it is expected that liquids with simple molecular structure exhibit a lower electrical permittivity. In fact, for the liquefied rare gases and cryogenic liquids with simple molecular structures, the dielectric constant is between 1.0 and 2.0. Notice that the dielectric constant is a ratio of the permittivities of medium and vacuum.

Therefore, a liquid with simple molecular structure, being more stable chemically, is a better choice to enhance the mesopump performance. A cryogenic liquid like liquid nitrogen can serve this purpose. However, liquid nitrogen has a low permittivity, and the generated pressure head of the mesopump will also be small, thereby making measurements more challenging.

Note that as documented in Chapter 2, the pressure head of an ion-injection pump is proportional to the permittivity of the working liquid. Besides, using the liquid nitrogen

would require redesigning the mesopump and the flow measurement loop. Applicability of the silicon substrate at the cryogenic temperature and thermal coefficients of expansion mismatch for different components of the mesopump also need to be investigated.

Another important point regarding the liquid nitrogen property is that its characteristic time for the relaxation of charge due to ohmic conduction (i.e. ϵ/σ_e) is very high compared to HFE-7100, since the conductivity of liquid nitrogen is quite small. This means that the generated ions inside the liquid nitrogen tend to retain their charge for a long time. Consequently, the efficiency of the ion-injection pump with liquid nitrogen is expected to be higher. Therefore, research leading to improvement in dielectric constant of LN2 without altering its molecular structure is a useful future work contribution. One method for this could be mixing of nitrogen with another gas of similar properties, but with the aim to raise the combined dielectric constant for the mixture for better pumping characteristics.

- **Characterization of the working liquid electrical properties**

As pointed out in the previous section, the electrical property of the working liquid is fundamental in determining the performance of the ion-injection pumps. It is important to investigate any variation of these properties under different circumstances such as temperature variation and exposure to the environmental moisture, electric field, or any other contamination. These fundamental electrical properties consist of the electrical permittivity, electrical conductivity and dielectric strength. Therefore, it is recommended that a series of tests be conducted to characterize the influence of these different factors on the properties. Moreover, it is also suggested that a measurement and

record of these properties be made on the fluid before and after each experimental run. For each of these properties, standard measurement techniques have been developed and documented, and such testing facilities are commercially available.

8.4 Summary

In this chapter various challenges involved in the present study were outlined. Specific contributions addressed by the present study were highlighted. Recommendations for future work for an improved and expanded understanding of the electrohydrodynamics phenomenon were discussed.

References

- Abdel-Salam, M. and Z. M. Al-Hamouz (1999). "Finite-Element Solution of Monopolar Corona on Bundle Conductors." IEEE Transactions on Industry Applications **35**(2): 380-386.
- Adamiak, K. (1994). "Adaptive Approach to Finite-Element Modeling of Corona Fields." Ieee Transactions on Industry Applications **30**(2): 387-393.
- Ahn, S. and Y. Kim (1997). Fabrication and Experiment of Planar Micro Ion Drag Pump. Transducer '97-International Conference on Solid-State Sensors and Actuators, Chicago.
- Asano, K., C.-r. Choi, et al. (2002). Acceleration and Deceleration of a Conductive Particle within Parallel Electrodes in Viscous Fluid. IEEE 11th International Conference on Conduction and Breakdown in Dielectric Liquids, Baden-Dattwil , Switzerland.
- Asano, K. and K. Yatsuzuka (1999). Fundamental Study of EHD Pump with Needle-Cylinder Electrodes. Conference on Electrical Insulation and Dielectric Phenomena, Austin, TX , USA.
- Atten, P. and J. Seyed-Yagoobi (2003). "Electrohydrodynamically Induced Dielectric Liquid Flow Through Pure Conduction in Point/Plane Geometry." IEEE Transactions on Dielectrics & Electrical Insulation **10**(1): 27-36.
- Barbini, G. and G. Coletti (1995). "Influence of Electrode Geometry on Ion-Drag Pump Static Pressure." IEEE Transactions on Dielectrics & Electrical Insulation **2**(6): 1100-1105.
- Benetis, V., A. Shooshtari, et al. (2003). A source-integrated micropump for cooling of high heat flux electronics. Semiconductor Thermal Measurement and Management Symposium, 2003. Ninteenth Annual IEEE.

- Bologa, M. K., I. V. Kozhevnikov, et al. (2000). Multistage Electrohydrodynamical Pump. Annual Report Conference on Electrical Insulation and Dielectric Phenomena, Victoria, BC, Canada.
- Bologa, M. K., I. A. Kozhukhar, et al. (1999). Electrohydrodynamic Pumps. IEEE 13th International Conference on Dielectric Liquids. (ICDL '99), Nara, Japan.
- Bologa, M. K., I. A. Kozhukhar, et al. (1993). Electrohydrodynamic Pump Service Life. IEEE 11th International Conference on Conduction and Breakdown in Dielectric Liquids, 1993., IC DL '93, Baden-Dattwil , Switzerland.
- Brand, K. and I. Seyed-Yagoobi (2002). "Effect of Electrode Position on Electrohydrodynamic Induction Pumping of a Stratified Liquid/ Vapor Medium." IEEE Transactions on Industry Applications **38**(2): 389 - 400.
- Brand, K. and J. Seyed-Yagoobi (2003). "Experimental Study of Electrohydrodynamic Induction Pumping of a Dielectric Micro Liquid Film in External Horizontal Condensation Process." Journal of Heat Transfer-Transactions of the Asme **125**(6): 1096-1105.
- Brayan, J. E. and I. Seyed-Yagoobi (1994). "Analysys of 2-Dimensional Flow Field Generated by a 1-Electrode-Pair Ion-Drag Pump." IEEE Transactions on Dielectrics & Electrical Insulation **1**(3): 459-467.
- Bryan, J. E. and I. Seyed-Yagoobi (1992). "An Experimental Investigation of Ion-Drag Pump in a Vertical and Axisymmetric Configuration." IEEE Transactions on Industry Applications **28**(2): 310-316.
- Bustgens, B., W. Bacher, et al. (1994). Micropump Manufactured by Thermoplastic Molding. IEEE Workshop on Micro Electro Mechanical Systems, 1994, MEMS '94, Oiso Japan.
- Buyanov, A. V. and Y. K. Stishkov (2003). "Kinematic Structure of Electrohydrodynamic Flow in ``Wire--Wire" and ``Wire over Plane" Electrode Systems Placed in a Liquid." Technical Physics **48**(8): 972-977.

- Castellanos, A. (1998). Electrohydrodynamics. New York, Springer-Verlag.
- Castellanos, A. (2003). "Entropy Production and the Temperature Equation in Electrohydrodynamics." IEEE Transactions on Dielectrics & Electrical Insulation **10**(1): 22- 26.
- Chattock, A. P., W. E. Walker, et al. (1901). Philosophical Magazine: 1-79.
- Chen, X., J. Cheng, et al. (2003). "Numerical Analysis of Electrohydrodynamics in a Round Pipe." IEEE Transactions on Dielectrics & Electrical Insulation **10**(2): 278-285.
- Cisse, L., S. S. Bamji, et al. (2003). "Electric Field Calculations for Needle-Plane Geometry and Space Charge in Polyethylene." IEEE Transactions on Dielectrics & Electrical Insulation **10**(1): 176-180.
- Coletti, G. and R. Bozzo (1996). A Contribution to the Evaluation of Electrohydrodynamic Pump for Insulating Oils. IEEE Annual Report - Conference on Electrical Insulation and Dielectric Phenomenon, San-Francisco.
- Cotton, J. S., D. Brocilo, et al. (2003). "Numerical Simulation of Electric Field Distributions in Electrohydrodynamic Two-Phase Flow Regimes." IEEE Transactions on Dielectrics & Electrical Insulation **10**(1): 37- 51.
- Crowley, J. M., G. S. Wright, et al. (1990). "Selecting a Working Fluid to Increase the Efficiency and Flow Rate of an EHD Pump." IEEE Transactions on Industry Applications **26**(1): 42-49.
- Darabi, J., M. M. Ohadi, et al. (2001). "An Electrohydrodynamic Polarization Micropump for Electronic Cooling." Microelectromechanical Systems **10**(1): 98-106.
- Darabi, J., M. Rada, et al. (2002). "Design, Fabrication, and Testing of an Electrohydrodynamic Ion-Drag Micropump." J. of Microelectromechanical Systems **11**(6): 684- 690.

- Davidson, J. H., F. A. Kulacki, et al. (1987). Convective Heat Transfer with Electric and Magnetic Fields. Handbook of single-phase convective heat transfer. S. Kakaç, R. K. Shah and W. Aung. New York, Wiley: 9.1-9.47.
- DeVoe, D. L. (2002). "Thermal issues in MEMS and microscale systems." IEEE Transactions on Components and Packaging Technologies **25**(4): 576-583.
- Dulikravich, G. S., V. Ahuja, et al. (1993). "Simulation of Electrohydrodynamic Enhancement of Laminar Flow Heat Transfer." Enhanced Heat Transfer **1**(1): 115-126.
- Feng, J. Q. (1999). "An Analysis Of Corona Currents Between Two Concentric Cylindrical Electrodes." Journal of Electrostatics **46**(1): 37-48.
- Feng, J. Q. (1999). "Application of Galerkin finite-element method with Newton iterations in computing steady-state solutions of unipolar charge currents in corona devices." Journal of Computational Physics **151**(2): 969-989.
- Franssila, S. (2004). Introduction to microfabrication. Chichester, West Sussex, England ; Hoboken, NJ, J. Wiley.
- Fuhr, G., T. Schnelle, et al. (1994). "Traveling Wave-Driven Microfabricated Electrohydrodynamic Pumps for Liquids." Journal of Micromechanics and Microengineering **4**: 217-226.
- Gallagher, T. J. (1975). Simple Dielectric Liquids : Mobility, Conduction, And Breakdown. Oxford [Eng.], Clarendon Press.
- Gerlach, T., M. Schuenemann, et al. (1995). "A New Micropump Principle of the Reciprocating Type Using Pyramidical Micro Flowchannels as Passive Valves." Journal of Micromechanics and Microengineering **5**(2): 199-201.
- Gerlach, T. and H. Wurmus (1995). "Working Principle and Performance of the Dynamic Micropump." Sensors and Actuators a-Physical **50**(1-2): 135-140.

- Haefliger, D., B. P. Cahill, et al. (2003). "Rapid Prototyping of Micro-Electrodes on Glass and Polymers by Laser-Assisted Corrosion of Aluminum Films in Water." Microelectronic Engineering **67-68**: 473-478.
- Higuera, F. J. (2000). "Electrohydrodynamic Flow of a Dielectric Liquid around a Blade Electrode." Physics of Fluids **12**(11): 2732-2742.
- Higuera, F. J. (2002). "Electrohydrodynamic Flow of a Dielectric Liquid Due to Autonomous Injection of Charge by a Needle Electrode." Physics of Fluids **14**(1): 423-426.
- Huang, L., W. Wang, et al. (2000). "LIGA Fabrication and Test of a DC Type Magnetohydrodynamic (MHD) Micropump." Microsystem Technologies-Micro- and Nanosystems-Information Storage and Processing Systems **6**(6): 235-240.
- IEEE-DEIS-EHD Technical Committee (2003). "Recommended International Standard for Dimensionless Parameters Used in Electrohydrodynamics." IEEE Transactions on Dielectrics & Electrical Insulation **10**(1): 3-6.
- Jang, J. and S. S. Lee (2000). "Theoretical and Experimental Study of MHD (Magnetohydrodynamic) Micropump." Sensors & Actuators A: Physical **80**: 84-89.
- Jeong, O. C. and S. S. Yang (2000). "Fabrication and Test of a Thermopneumatic Micropump with a Corrugated P Plus Diaphragm." Sensors and Actuators a-Physical **83**(1-3): 249-255.
- Jeong, S. I. and J. Seyed-Yagoobi (2002). Innovative Electrode Design for Electrohydrodynamic Conduction Pumping. Industry Applications Conference, 2002. 37th IAS Annual Meeting.
- Jeong, S.-I., J. Seyed-Yagoobi, et al. (2003). "Theoretical/Numerical Study of Electrohydrodynamic Pumping Through Conduction Phenomenon." IEEE Transactions on Industry Applications **39**(2): 355-361.

- Kallio, G. A. and D. E. Stock (1986). "Computation of Electrical Conditions inside Wire-Duct Electrostatic Precipitators Using a Combined Finite-Element, Finite-Difference Technique." Journal of Applied Physics **59**(6): 1799-1806.
- Karniadakis, G. E. and A. Beskok (2002). Micro Flows. New York, Springer Verlag.
- Kashani, R., S. Kang, et al. (2000). "Micro-Scale Electrohydrodynamic Pumped High Performance Actuation." Journal of Intelligent Material Systems and Structures **11**: 343-350.
- Kim, Y. T. and K. W. Whang (2000). "Two-Dimensional Numerical Simulation of Radical Generation in the Positive Corona Discharge." Ieee Transactions on Plasma Science **28**(1): 261-267.
- Koch, M., A. G. R. Evans, et al. (1998). "The Dynamic Micropump Driven With A Screen Printed PZT Actuator." Journal of Micromechanics and Microengineering **8**(2): 119-122.
- Kojevnikov, I., O. V. Motorin, et al. (2002). Optimization of the Electrohydrodynamic Pump. Annual Report Conference on Electrical Insulation and Dielectric Phenomena.
- Leger, L., E. Moreau, et al. (2002). "Effect of a Dc Corona Electrical Discharge on the Airflow along a Flat Plate." IEEE Transactions on Industry Applications **38**(6): 1478- 1485.
- Lemoff, A. V. and A. P. Lee (2000). "An Ac Magnetohydrodynamic Micropump." Sensors & Actuators (B) **63**: 178-185.
- Lesaint, O. and R. Tobazeon (1988). "Streamer Generation and Propagation in Transformer Oil under Ac Divergent Field Conditions." Ieee Transactions on Electrical Insulation **23**(6): 941-954.
- Madou, M. J. (2002). Fundamentals of Microfabrication: The Science of Miniaturization. Boca Raton, CRC Press.

- Makita, T., R.-i. Ohyama, et al. (2002). A Computerized Visualization of Gas-Phase Ehd Flow Field for Needle-Plane Electrodes System. Annual Report Conference on Electrical Insulation and Dielectric Phenomena.
- Malik, N. H., A. A. Al-Arainy, et al. (1998). Electrical Insulation in Power Systems. New York, Marcel Dekker.
- Maluf, N. (2000). An Introduction to Microelectromechanical Systems Engineering. Boston, Artech House.
- Marco, P. D., W. Grassi, et al. (2003). "Influence of Electric Field on Single Gas-Bubble Growth and Detachment in Microgravity." International Journal of Multiphase Flow **29**(4): 559-579.
- Maruvada, P. S. (2000). Corona Performance of High-Voltage Transmission Lines. Baldock, Hertfordshire, England ; Philadelphia, PA, Research Studies Press.
- Mcdonald, J. R., W. B. Smith, et al. (1977). "Mathematical-Model for Calculating Electrical Conditions in Wire-Duct Electrostatic Precipitation Devices." Journal of Applied Physics **48**(6): 2231-2243.
- Medlin, A. J., C. A. J. Fletcher, et al. (1998). "A Pseudotransient Approach to Steady State Solution of Electric Field-Space Charge Coupled Problems." Journal of Electrostatics **43**(1): 39-60.
- Melcher, J. R. (1981). Continuum Electromechanics. Cambridge, Mass., MIT Press.
- Melcher, J. R. (1989). "Noninvasive Ion-drag Velocimeter." Journal of Electrostatics **24**: 67-77.
- Mizeraczyk, J., J. Dekowski, et al. (2002). "Images Of Electrohydrodynamic Flow Velocity Field In A Dc Positive Polarity Needle-To-Plate Nonthermal Plasma Reactor." IEEE Transactions on Plasma Science **30**(1): 164-165.

- Oda, T., M. Aoyama, et al. (1996). Electrohydrodynamic Pumping Effect in Dielectric Liquid Using a Non-Uniform Traveling Field. 1996 IEEE Annual Report-Conference on Electrical Insulation and Dielectric Phenomenon, San Francisco.
- Owsenek, B. L. and I. Seyed-Yagoobi (1997). "Theoretical and Experimental Study of Electrohydrodynamic Heat Transfer Enhancement Through Wire-Plate Corona Discharge." Journal of Heat Transfer-Transactions of the ASME **119**: 604-610.
- Peek, F. W. (1929). Dielectric Phenomena in High-Voltage Engineering. New York [etc.], McGraw-Hill Book Company, inc.
- Pickard, W. F. (1963). "Ion-Drag Pumping I - Theory." Journal of Applied Physics **34**: 246-250.
- Pickard, W. F. (1963). "Ion-Drag Pumping II - Experiments." Journal of Applied Physics **34**: 251-258.
- Poliashenko, M. and C. K. Aidun (1995). "A Direct Method for Computation of Simple Bifurcations." Journal of Computational Physics **121**(2): 246-260.
- Pontiga, F. and A. Castellanos (1996). "Electrical Conduction of Electrolyte Solutions in Nonpolar Liquids." IEEE Transactions on Industry Applications **32**(4): 816-824.
- Qureshi, M. I. and W. G. Chadband (1988). "On the Relation between Current Pulses and Discharges." Ieee Transactions on Electrical Insulation **23**(4): 715-722.
- Rigo, M. (1993). Numerical Computation of Electrohydrodynamic Motions of Liquids Subjected to Unipolar Injection. IEEE 11th International Conference on Conduction and Breakdown in Dielectric Liquids, Baden-Dattwil , Switzerland.
- Roth, J. R. (2003). "Aerodynamic Flow Acceleration Using Paraelectric and Peristaltic Electrohydrodynamic Effects of a One Atmosphere Uniform Glow Discharge Plasma." Physics of Plasmas **10**(5): 2117-2127.

- Saidi, A., S. Moghaddam, et al. (2002). AAAV Project, Phase II, EHD Enhanced Liquid-Air Heat Exchangers, ATEC, Inc.
- Schmidt, W. F. (1997). Liquid State Electronics of Insulating Liquids. New York, CRC Press.
- Seyed-Yagoobi, J. and J. E. Bryan (1995). "Theoretical Analysis of Ion-Drag Pumping." IEEE Transactions on Industry Applications **31**(3): 469-476.
- Seyed-Yagoobi, J. and J. E. Bryan (1999). Enhancement of Heat Transfer and Mass Transport in Single-Phase and Two-Phase Flows with Electrohydrodynamics. Advances in Heat Transfer, Academic Press. **33**.
- Shoji, S., S. Nakagawa, et al. (1990). "Micropump and Sample-Injector for Integrated Chemical Analyzing Systems." Sensors and Actuators a-Physical **21**(1-3): 189-192.
- Stehr, M., S. Messner, et al. (1996). "The Vamp - A New Device for Handling Liquids or Gases." Sensors and Actuators a-Physical **57**(2): 153-157.
- Stishkov, Y. K. (1999). The Internal Contradictions in System of Electrohydrodynamics. 13th International Conference on Dielectric Liquids, Nara, Japon.
- Stishkov, Y. K. and A. V. Buyanov (2002). Electrodynamical Currents in a Wire-Wire Electrode System. Proceedings of 14th Conference on Dielectric Liquids, Graz, Austria.
- Stratton, J. A. (1941). Electromagnetic Theory. New York, London,, McGraw-Hill book company, inc.
- Stuetzer, O. M. (1959). "Ion-Drag Pressure Generation." Journal of Applied Physics **30**: 984-994.
- Stuetzer, O. M. (1960). "Ion-Drag Pumps." Journal of Applied Physics **31**: 136-146.

- Vazquez, P. A., E. Chacon Vera, et al. (2002). Finite Element-Particle Method Calculation of Ehd Plumes. Annual Report Conference on Electrical Insulation and Dielectric Phenomena.
- Wang, H. T. and J. D. Cross (1991). The Interpretation of Electrohydrodynamic Mobility under Unipolar Injection in Dielectric Liquids. the 3rd International Conference on Properties and Applications of Dielectric Materials, Tokyo , Japan.
- Watanabe, M., H. Shirai, et al. (2003). "Liquid-Liquid Two-Layer Electrohydrodynamic Flow System." Sensors and Actuators (Part B) **94**: 267-270.
- Wawzyniak, M. and J. Seyed-Yagoobi (2001). "Electrohydrodynamic Induction Pumping of a Stratified Liquid/Vapor Medium In The Presence of Volumetric and Interface Electric Charges." IEEE Transactions on Industry Applications **37**(4): 950-958.
- Whitehead, J. B. (1929). High Voltage Corona in International Critical Tables, McGraw-Hill.
- Wong, C. C., D. R. Adkins, et al. (1996). Development of A Micropump for Microelectronic Cooling. Micro-Electro-Mechanical Systems (MEMS). 1996 International Mechanical Engineering Congress and Exposition., New York, NY, USA, ASME.
- Yabe, A., Y. Mori, et al. (1978). "Ehd Study of Corona Wind between Wire and Plate Electrodes." AIAA Journal **16**(4): 340-345.
- Yamamoto, T., M. Okuda, et al. (2002). Three-Dimensional Ionic Wind and Electrohydrodynamics of Tuft/Point Corona Electrostatic Precipitator. Industry Applications Conference, 2002. 37th IAS Annual Meeting.
- Yanada, H., S. Hakama, et al. (2002). "An Investigation of an Ion Drag Pump Using a Needle-Mesh Electrode Configuration." Proceedings of the Institution of Mechanical Engineers Part C-Journal of Mechanical Engineering Science **216**(3): 325-335.

- Yao, S. H., D. E. Hertzog, et al. (2003). "Porous Glass Electroosmotic Pumps: Design and Experiments." Journal of Colloid and Interface Science **268**(1): 143-153.
- Zaghdoudi, M. C. and M. Lallemand (2001). "Nucleate Pool Boiling Under DC Electric Field." Experimental Heat Transfer **14**(3): 157-180.
- Zeng, S. L., C. H. Chen, et al. (2001). "Fabrication and Characterization of Electroosmotic Micropumps." Sensors and Actuators B-Chemical **79**(2-3): 107-114.
- Zeng, S. L., C. H. Chen, et al. (2002). "Electroosmotic Flow Pumps with Polymer Frits." Sensors and Actuators B-Chemical **82**(2-3): 209-212.
- Zhakin, A. I. (2002). Theoretical investigation of Complex Ion Formation in Liquid Dielectrics. IEEE 14th International Conference on Dielectric Liquids.
- Zhakin, A. I. and S. A. Lunev (1999). Theory of Net-EHD Pump. IEEE 13th International Conference on Dielectric Liquids, Nara , Japan.
- Zhong, J., M. Yi, et al. (2002). "Magneto Hydrodynamic (Mhd) Pump Fabricated with Ceramic Tapes." Sensors & Actuators A: Physical **96**(1): 59-66.